Johannes Gutenberg-Universität Mainz

Thermomechanical Modeling of Mantle Dynamics and Plate Motion in the Mediterranean

Dissertation
zur Erlangung des Grades
Doktor der Naturwissenschaften
im Promotionsfach Geowissenschaften

am Fachbereich Chemie, Pharmazie, Geographie und Geowissenschaften
der Johannes Gutenberg-Universität Mainz

Christian Schuler
geboren in Saarlouis

Mainz, 2025

1. Berichterstatter: Prof. Dr. Boris J. P. Kaus

2. Berichterstatter: Prof. Dr. Thibault Duretz

Tag der mündlichen Prüfung: 10.12.2025

Abstract

Over millions of years, the Mediterranean has been shaped by various geological processes. The region comprises several rollback subduction systems, some still actively retreating, and is influenced by the convergence of the African plate in the south and the Eurasian plate in the north. The dynamic behaviour is also reflected in the crust, as the region is characterized by numerous orogens as well as a complex plate motion pattern. The Adriatic microplate is located in the center of the Mediterranean and is bounded by the African plate and the Eurasian plate. This configuration makes the Mediterranean, and in particular the Adriatic microplate, an ideal setting to investigate the interplay between mantle dynamics and plate motion.

In this work, 3D thermomechanical modeling of the Mediterranean region is used to investigate the complex geological history of this region over the last 35 Myr. The results show that the subduction zones strongly interact with each other. The retreat of both the Apennines-Calabrian subduction system to the west of Adria and the Dinaric-Hellenic subduction system to the east of Adria leads to an increased dynamic pressure under the Adriatic microplate. This results in mantle flow to the north and south. In the north, the mantle flow is blocked by the Alpine slab, so that mantle flow parallel to the Alpine trench emerges starting at 20 Ma. Another aspect of the study is the plate motion of the Adriatic microplate. The results indicate that this is primarily controlled by the convergence of the African and Eurasian plates, the horizontal distance between the Calabrian and Hellenic trenches and the Alpine slab retreat to the north of Adria.

The simulation results are used to calculate synthetic shear-wave splitting parameters to quantify seismic anisotropy. The comparison with observations reproduces first-order features, such as the trench-parallel orientation of the fast polarization direction south of the Alpine slab. However, the comparison between the model and observations is not perfect, as some regions, such as the Liguro-Provençal Basin, exhibit differences. These differences may stem from features absent in the model, such as a slab gap of the Apennines slab or lower mantle structures. Overall, the comparison demonstrates the value of shear wave splitting observations as an observational constraint and shows how the model results can help interpret observations.

Thermomechanical simulations typically involve a large number of material parameters, and it is often difficult to quantify the individual influence of each parameter on a specific output of interest, such as the velocity of a subduction plate. With the discrete adjoint method, it is possible to calculate sensitivities that show the influence of material parameters on a specific output of interest. Here, we illustrate the implementation of the discrete adjoint method with automatic differentiation. This approach has the advantage that it allows functions from the Stokes solver to be reused, enabling the design of a problem-agnostic adjoint solver. The resulting sensitivities are scaled to allow a comparison between different parameters. Finally, this method is applied to a 2D subduction zone with a nonlinear visco-elastic rheology, where the effects of slab pull and ridge push on the plate motion are compared quantitatively.

Kurzfassung

Über Millionen von Jahren hinweg wurde der Mittelmeerraum von verschiedenen geologischen Prozessen geformt. Die Region umfasst mehrere zurückweichende Subduktionszonen, von welchen heute noch einige aktiv sind. Außerdem steht die Region im Einfluss der Konvergenz der Afrikanischen Platte im Süden und der Eurasischen Platte im Norden. Das dynamische Verhalten zeigt sich auch in der Erdkruste, da die Region von mehreren Gebirgen und einer komplexen Plattenbewegung gekennzeichnet ist. Die Adriatische Platte befindet sich im Zentrum des Mittelmeerraums und ist von der Afrikanischen und Eurasischen Platte begrenzt. Diese Zusammenstellung macht den Mittelmeerraum und im Speziellen die Adriatische Platte zu einem idealen Ort, um das Zusammenspiel aus Manteldynamik und Plattenbewegung zu untersuchen.

In dieser Arbeit wird thermomechanische 3D-Modellierung verwendet, um die komplexe geologische Geschichte der Region über die letzten 35 Millionen Jahre besser zu verstehen. Die Ergebnisse zeigen, dass sich die Subduktionszonen gegenseitig stark beeinflussen. Das Zurückweichen des apenninisch-kalabrischen Subduktionssystems westlich der Adriatischen Mikroplatte und des dinarisch-hellenischen Subduktionssystems östlich von Adria führt zu einem erhöhten dynamischen Druck im Erdmantel unter der Adriatischen Platte. Dies resultiert in Mantelfluss nach Norden und nach Süden. Im Norden wird der Mantelfluss durch die alpine Subduktionszone blockiert, sodass sich seit 20 Millionen Jahren ein Mantelfluss parallel zur alpinen Subduktionszone entwickelt hat. Ein anderer Aspekt der Studie befasst sich mit der Plattenbewegung der Adriatischen Platte. Die Ergebnisse zeigen, dass diese vor allem von der Konvergenz der Eurasischen mit der Afrikanischen Platte, der horizontalen Distanz der kalabrischen und der hellenischen Subduktionszone sowie dem Zurückweichen der alpinen Subduktionszone abhängt.

Mit den Simulationsergebnissen werden synthetische Parameter für die seismische Doppenelbrechung berechnet, um die seismische Anisotropie zu charakterisieren. Der Vergleich mit Beobachtungen reproduziert Merkmale erster Ordnung, wie die parallele Orientierung der schnellen Polarisationsrichtung zur alpinen Subduktionszone im Süden der Alpen. Der Vergleich zwischen Modellergebnissen und seismischen Beobachtungen zeigt jedoch auch Unstimmigkeiten, wie zum Beispiel im Liguro-Provençal Becken. Diese Unterschiede können auf Merkmale zurückzuführen sein, die im Modell nicht auftreten, wie zum Beispiel eine Lücke in der apenninischen Subduktionsplatte, oder auf Strukturen im unteren Mantel. Insgesamt zeigt der Vergleich, dass die Analyse der seismischen Doppelbrechung eine zusätzliche Möglichkeit zur Verifizierung des numerischen Modells bietet und dass die Modellergebnisse helfen können, die Beobachtungen besser zu interpretieren.

Thermomechanische Simulationen beinhalten typischerweise eine Vielzahl an Modellparametern und es ist oft schwierig, den individuellen Einfluss einzelner Parameter auf ein bestimmtes Resultat, wie z. B. die Geschwindigkeit einer Subduktionsplatte, zu quantifizieren. Mit der diskreten Adjungierten Methode ist es möglich, Sensitivitäten zu berechnen, die den Einfluss von Materialparametern auf ein bestimmtes Ergebnis zeigen. In diesem Zusammenhang ist die Implementierung der diskreten Adjungierten Methode mithilfe automatischer Differentiation beschrieben. Dieser Ansatz hat den

Vorteil, dass Funktionen aus dem Stokes-Löser wiederverwendet werden können, was die Entwicklung von einem problemunabhängigen Adjungierten-Löser ermöglicht. Die resultierenden Sensitivitäten werden skaliert, um einen Vergleich verschiedener Parameter zu ermöglichen. Schließlich wird diese Methode auf eine 2D-Subduktionszone mit einer nichtlinearen, visko-elastischen Rheologie angewendet. Dabei werden verschiedene Prozesse, die die Plattenbewegung beeinflussen, quantitativ miteinander verglichen.

Contents

List of Figures

List of Tables

List of Algorithms

List of Abbreviations

yr	Years
Myr	Million Years (10^6 yr)
Ma	Million Years Ago
2D	Two-Dimensional
3D	Three-Dimensional
REF	Reference Model
Adria	Adriatic Microplate
WMS	Western Mediterranean Slab
AlCS	Alpine-Carpathian Slab
DHS	Dinaric-Hellenic Slab
ApCS	Apennines-Calabrian Slab
GS	Gibraltar Slab
FPD	Fast Polarization Direction
AD	Automatic Differentiation
VJP	Vector-Jacobian-Product
JVP	Jacobian-Vector-Product

Chapter 1

Introduction

1.1 Geology of the Mediterranean

The Mediterranean region is geologically complex and shaped by the interaction between different subduction zones, the convergence of the Eurasian and African plates and lithospheric dynamics like orogenic processes. The tectonic map of the region illustrates the general configuration, with the Eurasian plate to the north and the African plate to the south (Figure 1.1). Multiple collisional plate boundaries subdivide the region, forming several microplates, such as the Adriatic and Anatolian plates (e.g., Jolivet and Faccenna, 2000; Hinsbergen et al., 2020; Le Breton et al., 2021).

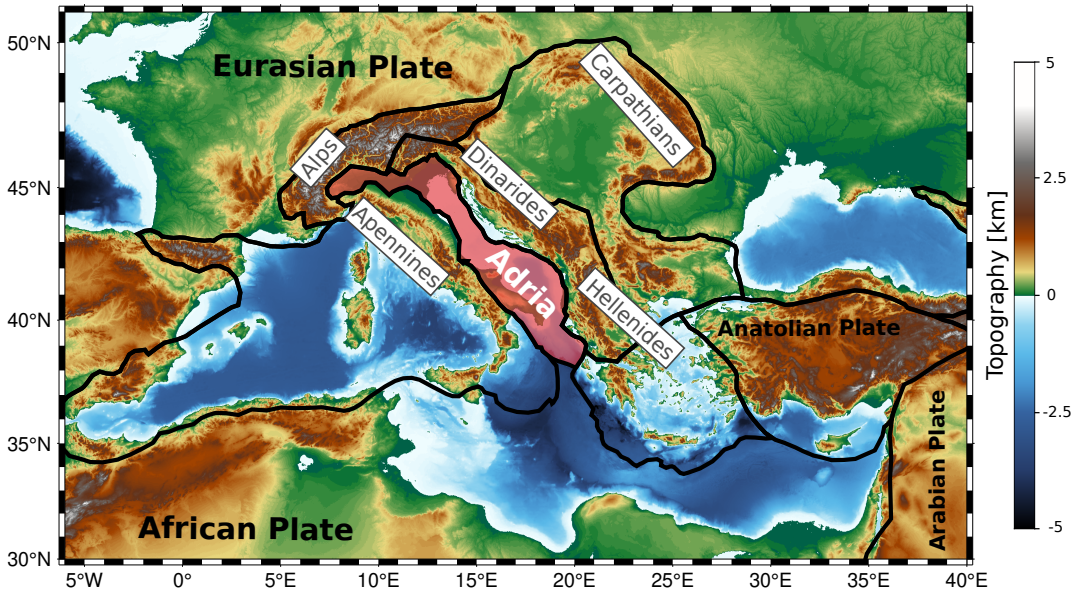

FIGURE 1.1: Topographic map of the central Mediterranean region. Major plate boundaries are outlined in black and adapted from Hasterok et al. (2022). The Adriatic microplate is highlighted in reddish tones. The Alps, Apennines, Dinarides, Carpathians and Hellenides are indicated with textboxes.

The Adriatic microplate, in the following also referred to as Adria, is located between the Eurasian plate in the north and the African plate in the south (see reddish area in Figure 1.1). It is elongated in a north–south direction, extending about 1300 km and reaching up to 200 km at its widest section (Kissling, 2024). Several orogens, including the Alps to the north, the Dinarides to the east, the Hellenides to the southeast and the Apennines to the west surround the microplate. While Adria's crust is mostly covered by the Adriatic Sea, the microplate extends northward into the Po Basin in northern Italy and borders the oceanic lithosphere of the Ionian Basin

to the south (e.g., Catalano et al., 2001; Hinsbergen et al., 2014; Hinsbergen et al., 2020). The exact extent of Adria is difficult to define and varies among studies (e.g., Angrand and Mouthereau, 2021; Le Breton et al., 2021; Jolivet, 2023). Therefore, the plate boundaries shown in Figure 1.1 are approximated and based on Hasterok et al. (2022).

Since the Cretaceous, the Eurasian and African plates have been converging (e.g., Dewey et al., 1989), a process that continues to the present-day (e.g., Serpelloni et al., 2022; Figure 1.2). The African plate moves northwest relative to a fixed Eurasian plate. East of the African plate lies the Arabian plate, which moves northeast at velocities of more than 1 cm/yr, thereby exceeding the plate velocity of the African plate. However, the highest horizontal surface velocities in the Mediterranean are observed southeast of the Adriatic microplate, where the Anatolian microplate moves southwest (Serpelloni et al., 2022; Figure 1.2). Adria, with its continental lithosphere (Piccardi et al., 2011), acts as a relatively rigid block between the African and Eurasian continents and remains largely undeformed (e.g., Anderson and Jackson, 1987). It was long assumed that Adria moves as a promontory of Africa to the north (e.g., McKenzie, 1972; Channell et al., 1979). However, it has been shown that Adria has moved consistently northeastward over the past 20 Myr, and therefore independently from Africa (Le Breton et al., 2017). This also manifests in today's picture of the plate motion (e.g., Battaglia et al., 2004; Serpelloni et al., 2022), which is illustrated in Figure 1.2. Adria's motion clearly deviates from that of the African plate, as seen by comparing western African velocities with those of Adria, showing an almost 90° difference in direction. It can also be seen here that the microplate rotates anticlockwise around a rotation pole located at the northwestern tip of Adria (e.g., Anderson and Jackson, 1987; Hinsbergen et al., 2014; Le Breton et al., 2017).

In addition to its plate boundary setting, the Mediterranean is characterized by various rollback subduction systems, some of which are still active today (e.g., Wortel and Spakman, 1992; Jolivet and Faccenna, 2000; Faccenna et al., 2014). Figure 1.2 shows portions of the plate boundaries in green, which are associated with slabs that are still attached to the lithosphere at present-day. The following provides a broad summary of the present-day slabs and their origins. A detailed description of the geological evolution over the past 35 Myr is provided in Section 2.2 of the next chapter. We first consider the Alpine slab north of Adria, which descends steeply into the mantle (Rappisi et al., 2022) and shows a slab break-off in the east and possibly also in the west (Kästle et al., 2020). This slab was part of a larger subduction system that included the Carpathians region and retreated northward (e.g., Handy et al., 2015). Today, besides the Alpine slab, only a small slab segment in the southeastern Carpathians, the Vrancea slab, is still attached to the lithosphere (Koulakov et al., 2010). The Apenninic, Calabrian, and Gibraltar slabs were once part of a single subduction system in the western Mediterranean, which was initiated around 35 Ma (e.g., Faccenna et al., 2014; Hinsbergen et al., 2020; Le Breton et al., 2021). This subduction system splits into separate subduction zones following a slab break-off along the African plate boundary (e.g., Rosenbaum et al., 2002a; Faccenna et al., 2014). At present-day the Gibraltar slab is retreating towards the Atlantic (Duarte et al., 2024) and the Calabrian slab is located to the southwest of Adria and is retreating towards southeast (Cifelli et al., 2007). Seismicity shows that both subduction zones are still active (e.g., Gutscher et al., 2002; Maesano et al., 2017). The Apenninic slab to the north is separated from the Calabrian slab by a slab window (Fellin et al., 2022). It reaches steeply into the mantle while remaining connected to the Calabrian slab at depth (Rappisi et al., 2022). East of Adria, a large-scale subduction system in the Dinarides–Hellenides retreated southwestward (Menant et al., 2016) and is

currently interrupted by slab gaps, resulting in distinct Dinaric, Hellenic and Cyprus slab segments (Evangelidis, 2017; Rappisi et al., 2022).

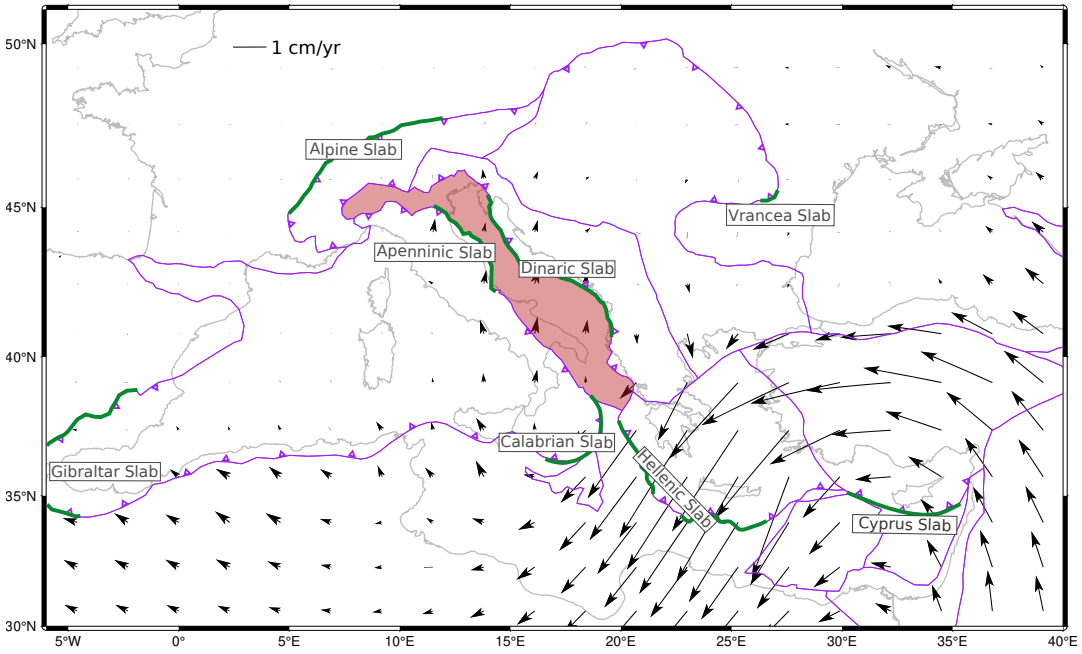

FIGURE 1.2: Horizontal plate velocities in the central Mediterranean region. Plate velocities are adapted from Serpelloni et al. (2022) and shown as black arrows. Coastlines are indicated by grey lines and plate boundaries by purple lines. Purple triangles mark plate boundaries associated with collision and subduction (e.g., Le Breton et al., 2021). The green lines indicate the approximate locations of the plate boundaries associated with subduction zones that are still attached to the lithosphere at present day and are compiled from Faccenna et al. (2014), Evangelidis (2017), Maesano et al. (2017), Civiero et al. (2020), and Rappisi et al. (2022). Text boxes indicate the names of the different subduction slabs.

Overall, the Mediterranean exhibits an interesting role model for the interaction between upper mantle dynamics and lithospheric dynamics. Various subduction zones retreat in close proximity, influencing each other as well as the regional plate motion (e.g., Király et al., 2018b). Additionally, the large-scale convergence of Africa and Eurasia, combined with the complex plate boundary configuration, results in a complicated present-day plate motion pattern. These circumstances make the Adriatic microplate an ideal location to study the interactions among the key drivers of Mediterranean geodynamics.

1.2 Present-Day Mantle Structure

The present-day asthenospheric structure of the Mediterranean has been investigated through numerous seismic studies, including isotropic P-wave tomographies (e.g., Piromallo and Morelli, 2003; Spakman and Wortel, 2004; Paffrath et al., 2021), P- or S-wave receiver function studies (e.g., Lis Mancilla et al., 2015; Monna et al., 2019) or anisotropic P-wave tomography studies (e.g., Wei et al., 2019; Rappisi et al., 2022; Rappisi et al., 2025). However, interpreting seismic tomography in terms of subduction geometry is non-unique and remains challenging (e.g., El-Sharkawy et al., 2020; Handy et al., 2021). To this end, we aim to present an interesting approach that combines different seismic tomography models to identify where most studies agree

on the presence or absence of a slab. This approach is inspired by Kästle et al. (2022), who applied it to the Alpine region. In this approach, different seismic tomography models are analyzed with respect to the possible presence of a slab. A slab is defined as a region with positive velocity anomalies that fall within one standard deviation of the respective dataset. The votemaps indicate the percentage of tomography models that agree on the presence of a slab at a specific location. Overall, 8 different seismic tomographies are evaluated (Lippitsch et al., 2003; Piromallo and Morelli, 2003; Mitterbauer et al., 2011; Koulakov et al., 2015; Zhu et al., 2015; Hua et al., 2017; Paffrath et al., 2021; Rappisi et al., 2022). Note that data from all tomography models are not available at every location. Therefore, the percentage is always calculated relative to the number of valid tomography models at each point.

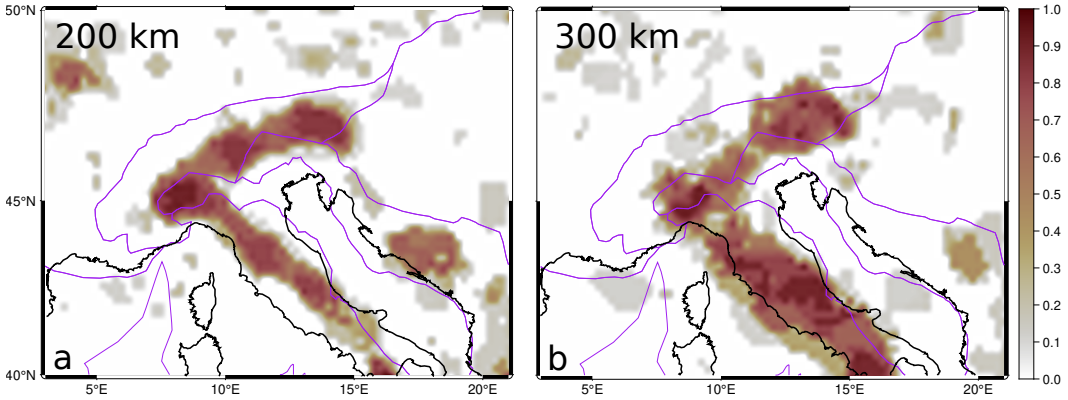

FIGURE 1.3: Votemaps of the Alpine region at two depths: (a) 200 km and (b) 300 km. The votemaps are based on different seismic tomography models of the region. For an explanation and the references of the tomography models that have been used, please refer to the main text.

As an example for the Mediterranean region, the asthenosphere underneath the Alpine area and northern Adria is examined. Figure 1.3 shows votemaps at depths of 200 km and 300 km for the 8 tomography studies. In both depth slices, two main slab regions can be identified where most models agree on the presence of a positive velocity anomaly, interpreted as a slab. North of the Adriatic microplate, the Alpine slab extends from west to east. In contrast, west of Adria, the Apenninic slab is located, oriented parallel to Adria and extending from southeast to northwest. At 200 km depth, the majority of models suggest a connection between the two slabs, while at 300 km depth, the existence of such a connection is less certain. The width of the high-percentage area also increases, indicating greater uncertainties regarding the exact slab location. To the northeast of Adria, the tomography models consistently indicate the absence of a slab, whereas further south, around 50 % of the models detect a circular velocity anomaly at a depth of 200 km.

Although this represents a simplified approach to comparing different data sources, it highlights the difficulty of determining the present-day geometry of the upper mantle structure. Apart from that, the plate tectonic history of the region is also subject to uncertainties, as different reconstructions of the area exist (e.g., Rosenbaum et al., 2002a; Romagny et al., 2020; Le Breton et al., 2021). The uncertainty of geological data, both about the present-day and the past, makes it difficult to infer the underlying mantle and lithospheric processes in the region. Geodynamic modeling can therefore help bridge the gap between reconstructions and present-day observations by aiming to provide a solid understanding of the underlying physical processes.

1.3 Aim and Structure of the Thesis

Overall, this thesis aims to link mantle dynamics with lithospheric processes in the Mediterranean by running and analyzing 3D thermomechanical models, connecting model results with observations and presenting a quantitative approach for studying physical processes in numerical models. The thesis consists of three main chapters and a final concluding chapter. Chapter 2 has been published in *Geochemistry, Geophysics, Geosystems*. The individual chapters address the following topics:

Chapter 2: 3D thermomechanical simulations of the central Mediterranean region are analyzed. The aim is to investigate subduction dynamics in the upper mantle, including the subduction systems of the Dinarides and Hellenides, the western Mediterranean and the Alpine–Carpathian region. The simulations cover the past 35 Myr to explore possible links between mantle dynamics and lithospheric response. Particular attention is given to the plate motion of the Adriatic microplate since 35 Ma in order to investigate how Adria responded to the surrounding geodynamic processes. Furthermore, the interactions between the different subduction systems and their influence on mantle flow in the upper mantle beneath the Mediterranean are examined.

Chapter 3: Here, direct seismic observations from the Mediterranean region are combined with the results of the thermomechanical simulation presented in Chapter 2. To this end, synthetic shear-wave splitting parameters are calculated from the simulation and compared with observed shear-wave splitting data from the region. Particular emphasis is placed on the Alpine region, where the synthetic data are thoroughly compared with the results of Link and Rümpker (2023). This comparison provides an additional constraint for the geodynamic simulation and aids in the interpretation of the observations.

Chapter 4: The implementation of the discrete adjoint method within an existing thermomechanical Stokes code is presented. The use of automatic differentiation to develop a problem-agnostic adjoint solver is described. Furthermore, it is shown how adjoint sensitivities can be used to analyze the physical mechanisms of different geodynamic processes, such as a plume head rising through the lithosphere. Finally, the method is applied to a 2D subduction zone to investigate the processes that control horizontal plate motion.

Chapter 5: This is a concluding chapter that summarizes and connects the results of the previous chapters and finally provides an outlook on what can be done in the future.

1.4 Author contribution

This section lists all contributors to the different chapters along with their individual contributions:

Chapter 2:

Mantle dynamics in the Mediterranean and Plate Motion of the Adriatic Microplate: Insights from 3D Thermomechanical Modeling - *C. Schuler, B.J.P. Kaus, E. Le Breton, N. Riel, A. A. Popov*

C. Schuler developed the concept, ran the simulations, analyzed the data and wrote the manuscript. B.J.P. Kaus acquired project funding, developed the concept and reviewed and edited the manuscript. E. Le Breton acquired project funding, contributed to the concept and reviewed and edited the manuscript. N. Riel assisted with methodological issues and reviewed the manuscript. A.A. Popov developed the

software and reviewed and edited the manuscript.

Chapter 3:

Shear Wave Splitting in the Mediterranean and Alpine Region: Models vs. Observations - *C. Schuler, J.P. Kruse, F. Link, B.J.P. Kaus*

C. Schuler developed the concept of the study, ran the thermomechanical simulation, analyzed the data and wrote the manuscript. J.P. Kruse contributed to the concept of the study, provided the routines to calculate synthetic shear-wave splitting, the ODREX software for texture calculations and the lamem2drexinput software and assisted with their installation and reviewed the manuscript. F. Link provided the data and plotting routines for the figures comparing the data with observations, and reviewed the manuscript. B.J.P. Kaus acquired project funding and reviewed the manuscript.

Chapter 4:

Adjoint Solver for Nonlinear Stokes Flow: Implementation with Automatic Differentiation and Sensitivity Analysis - *C. Schuler, A. de Montserrat Navarro, J. Frasunkiewicz, P.S. Aellig, H. Dominguez, V. Churavy, E. Moulas, A. A. Popov, B.J.P. Kaus, I. Utkin, L. Räss*

C. Schuler developed the concept of the study, implemented the adjoint solver, ran the simulations, analyzed the data and wrote the manuscript. A. de Montserrat Navarro is the developer of the JustRelax.jl software (and implemented the Stokes solver), assisted with implementation issues and reviewed the manuscript. J. Frasunkiewicz contributed to discussions regarding the adjoint solver and sensitivities and reviewed the manuscript. P.S. Aellig provided support with the JustRelax.jl and reviewed the manuscript. H. Dominguez reviewed the manuscript. E. Moulas and A. A. Popov reviewed the methodology section of the manuscript. V. Churavy provided support with issues regarding Enzyme.jl. B.J.P. Kaus acquired project funding. I. Utkin and L. Räss introduced C. Schuler to the adjoint method through an intensive short course on the subject and provided help on theoretical questions.

Chapter 2

Mantle Dynamics in the Mediterranean and Plate Motion of the Adriatic Microplate: Insights From 3D Thermomechanical Modeling

This chapter has been published in:
Schuler, C., Kaus, B. J., Le Breton, E., Riel, N., & Popov, A. A. (2025). Mantle dynamics in the mediterranean and plate motion of the Adriatic microplate: Insights from 3D thermomechanical modeling. *Geochemistry, Geophysics, Geosystems, 26(3), e2024GC011996.* https://doi.org/10.1029/2024GC011996. This version includes minor spelling corrections in comparison with the published version.

Abstract

The motion of the Adriatic microplate is thought to be highly sensitive to the surrounding subduction zones and the convergence of Africa and Eurasia. However, our understanding of the mantle dynamics in the Mediterranean region and its effect on plate motion remains incomplete. Here, we present a large set of 3D thermomechanical models of the entire Mediterranean region over the last 35 Myr to understand what controls the motion of the Adriatic microplate. The simulations take the convergence of the African and Arabian plates with the Eurasian plate into account, along with the dynamics of the subduction systems in the western (Apennines-Calabria), central (Dinarides-Hellenides) Mediterranean and in the Alpine-Carpathian region. Our results demonstrate that the subduction systems around Adria are highly coupled, which gives rise to complex asthenospheric flow in the central Mediterranean. We find that the plate motion of the Adriatic microplate over the last 35 Myr is controlled by the interplay of three main factors: (a) the convergence between the African and Eurasian plates, (b) the retreat of the Alpine subduction zone to the north of Adria, and (c) the distance between the Calabrian and Hellenic subduction zones around Adria. Furthermore, in a system characterised by active convergence between Africa and Eurasia, the slab pull exerted by nearby subduction zones can only notably influence the motion of the Adriatic microplate if these subduction zones are located within a few hundred kilometres of Adria.

Plain language summary

Over the last 35 Myr, different geological processes were active in the Mediterranean. The African and Arabian tectonic plates collided with the Eurasian plate, and as a result of this convergence, different subduction zones were active around the Adriatic microplate, which is situated in the middle of this complex geological system. This study presents 3D thermomechanical simulations of the Mediterranean region over the last 35 Myr. This method lets us simulate how rocks behave and deform over large time and space scales. We look at how different subduction zones affect the motion of the Adriatic microplate. The subduction zones around Adria have opposite polarity and have moved closer together over time, resulting in a complex flow of the subjacent mantle. Our results show that the plate motion of Adria over the last 35 Myr is mainly affected by the African plate pushing it from the south, the retreat of the Alpine subduction zone to the north and of the western Mediterranean and Dinaric-Hellenic subductions to the west and east of Adria. The subduction systems around Adria can notably influence its plate motion only if they are located within a few hundred kilometres of Adria.

Key Points:

- Systematic 3D thermomechanical simulations of the Mediterranean incorporating Africa-Eurasia convergence and all major subduction zones.
- Asthenospheric mantle dynamics in the Mediterranean is dominated by toroidal flow caused by complex subduction dynamics.
- Adria's motion depends on Africa-Eurasia convergence, Alpine slab retreat and the distance between the Calabrian and Hellenic trenches.

2.1 Introduction

The geological evolution of the Mediterranean region is a complex interplay of continental terranes and subduction systems in both time and space. Understanding the interacting processes between different subduction systems, such as in the central Mediterranean with both the Calabrian and Hellenic active subduction zones, remains the subject of an ongoing scientific debate (e.g., Chertova et al., 2014; Faccenna et al., 2001; Faccenna et al., 2014; Király et al., 2021; Royden and Faccenna, 2018; Wortel and Spakman, 2000; Wortel and Spakman, 1992). The last 35 Myr are of particular interest, as this period approximately marks the onset of collision in the Alps and of the rollback subduction of the Apennines-Maghrebides and the Hellenides, both accompanied by upper plate extension in the western Mediterranean and in the Aegean, respectively (e.g., Faccenna et al., 2014; Le Breton et al., 2021; Rosenberg et al., 2021; Hinsbergen et al., 2020). Consequently, 35 Ma serves as an appropriate starting point to investigate the interactions between the retreating subduction zones in the Mediterranean and the associated mantle dynamics. The Adriatic microplate plays a key role in this setting due to its location between the converging European and African plates to the north and south, respectively (Figure 2.1). Africa has been converging with Eurasia since the Cretaceous (e.g., Dewey et al., 1989) and today, the Adriatic microplate is almost entirely surrounded by orogenic belts, with the retreating Calabrian and Hellenic subduction zones to the south, the Apennines to the

west, the Dinarides to the east and the Alps to the north (Figure 2.1). As a result, the Adriatic microplate is highly sensitive to the various processes occurring within the Mediterranean (e.g., Király et al., 2018b; Le Breton et al., 2017; Hinsbergen et al., 2014). It was long assumed that Adria acted as a promontory of Africa (e.g., McKenzie, 1972; Muttoni et al., 2001). However, plate motion velocities show that Adria's present-day motion is clearly different from that of Africa (e.g., D'agostino et al., 2008), with a counterclockwise rotation with respect to Europe and Africa that may have started after approximately 20 Ma (e.g., Le Breton et al., 2017; Rosenbaum et al., 2004; Ustaszewski et al., 2008)

A common approach to explore the geodynamic history of the Mediterranean is to reconstruct the kinematic motion of the plates involved, based on a compilation of geological (structural, metamorphic, magmatic, stratigraphic) and geophysical data, such as seismic tomography models of the mantle (e.g., Handy et al., 2010; Handy et al., 2015; Le Breton et al., 2021; Menant et al., 2016; Rosenbaum et al., 2002b; Schettino and Turco, 2011; Stampfli and Kozur, 2006; Hinsbergen et al., 2020). These reconstructions provide valuable information about plate motion over geological timescales and how it compares with the structure of the mantle today. However, it can be challenging to make quantitative assumptions about the mantle processes that caused the plate motion and the present-day mantle structure. Thermomechanical modelling attempts to narrow this gap by using physically consistent models that can help understand the driving forces and their interactions through geological time.

Previous work on the interaction of different mantle processes using 3D numerical and analogue modelling has mainly focused on a limited number of pre-selected processes. Király et al. (2018b) use analogue models to investigate the effect of a double-sided subduction zone on plate motion, inspired by the Adriatic microplate. Holt et al. (2017) investigate double-sided subduction zones with numerical modelling. Confal et al. (2018) and Lo Bue et al. (2021) use numerical modelling to study the evolution of the Hellenic slab and the Calabrian slab, respectively. Martinod et al. (2024) use analogue models to analyze the influence of slab break-off in the western Mediterranean on Adria's motion and the Alpine dynamics. Duarte et al. (2024) investigate the evolution of the Gibraltar subduction zone and Peral et al. (2022) use numerical modelling to test the hypothesis of opposing subduction systems in the western Mediterranean. Efforts have also been made to investigate the current structure of the upper mantle using instantaneous models (e.g., Faccenna and Becker, 2010; Glerum et al., 2021; Kumar et al., 2022). Other analogue modelling studies focus specifically on smaller-scale structures such as slab gabs (Király et al., 2018b) or detachment processes (Boutelier and Cruden, 2017), as these can be related to the Apennin-Calabrian subduction system and the Alpine subduction zone, respectively.

Nonetheless, a common feature of all these studies is that they focus on rather regional processes while not necessarily taking into account all concurrent processes, such as the convergence of Africa and Eurasia or the surrounding subduction zones. Here, we aim to include all the main driving forces in the Mediterranean region, namely the pushing African and Arabian plates (w.r.t. a fixed Eurasian continent), as well as the subduction systems in the western Mediterranean, the eastern Mediterranean and in the Alpine and Carpathian regions. We created 3D models of the Mediterranean region and carried out thermomechanical forward simulations to study the evolution of this area over the last 35 Myr. The dynamics of the subduction zones is predominantly influenced by internal forces, including slab pull forces, the opening of rift systems and rigid plate interactions at the surface. The motion of the African continent is prescribed at the southern boundary and exerts a far-field force on the subduction dynamics.

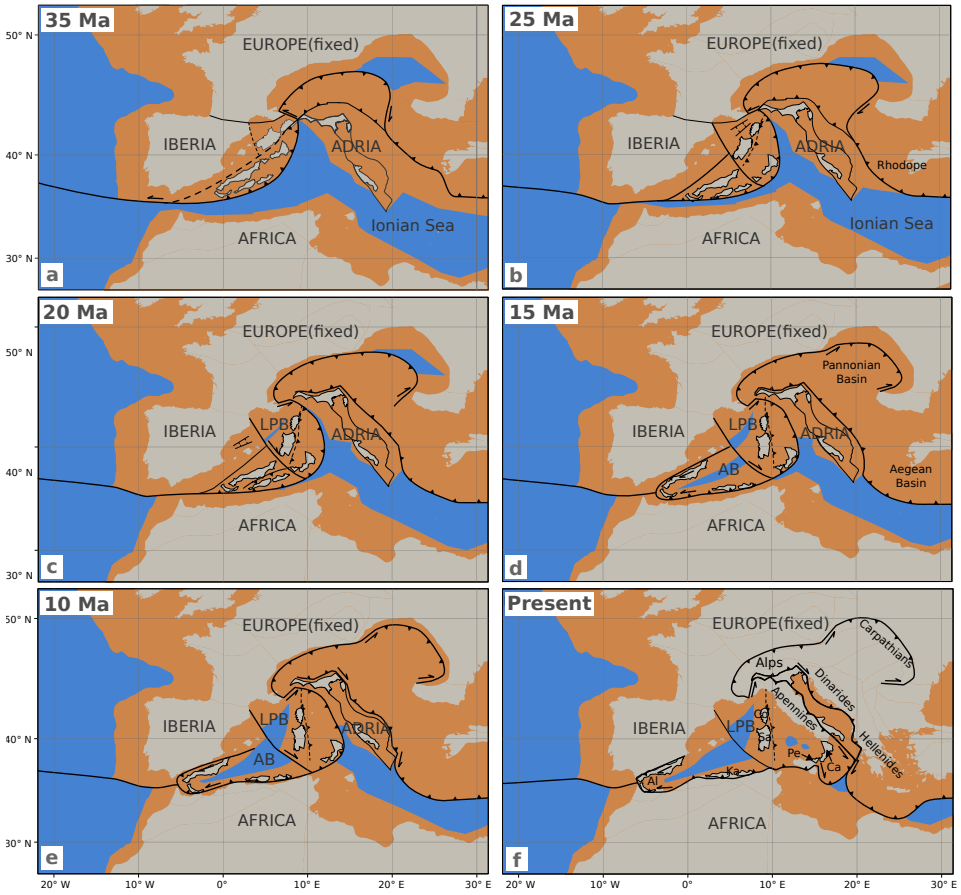

FIGURE 2.1: Kinematic reconstruction of the Mediterranean over the last 35 Myr, modified after Le Breton et al. (2021). Beige colour shows continental crust, orange colour shows thinned continental margin and blue colour shows oceanic crust. Back in time, orange also includes crustal domains deformed during Alpine Orogeny. Black lines with triangles show trench position of the various subduction systems. The Adriatic microplate is bound by black lines. LPB stands for Liguro-Provençal Basin, AB for Algerian Basin, Al for Alboran, Ka for Kabylides, Pe for Peloritani, Ca for Calabria, Co for Corsica and Sa for Sardinia.

In this study, we develop a reference model to reproduce the first-order mechanisms governing the Mediterranean region. We perform a parameter analysis to investigate the driving forces behind subduction dynamics and plate motion of the Mediterranean. Special emphasis is placed on the interaction between the various subduction systems, which remains a topic of debate (e.g., Király et al., 2021), as well as on the motion of the Adriatic microplate. Our aim is to identify the primary drivers of Adria's plate motion and establish a connection to its present-day dynamics.

2.2 Tectonic Evolution in the Mediterranean

The Mediterranean region exhibited pronounced tectonic activity throughout its geological history, which was investigated by various kinematic reconstructions (e.g., Handy et al., 2010; Jolivet and Faccenna, 2000; Le Breton et al., 2021; Menant et al., 2016; Hinsbergen et al., 2020). Since approximately 83 Ma, Africa converged with

respect to Eurasia and the south-dipping Alpine subduction was initiated, which consumed the Piemont-Ligurian (PL) ocean until about 35 Ma. To the east of the Adriatic microplate, the Hellenic-Dinaric subduction retreated and consumed the Vardar oceanic crust. Subsequently, the retreat of the rollback slowed down, as thin continental crust was subducted (e.g., Menant et al., 2016). At approximately 35 Ma, Adria collided with the European continent (e.g., Le Breton et al., 2021; Hinsbergen et al., 2020). This phase of indentation was accompanied by lateral extrusion towards the east, fast rollback of the Carpathians and extension of the Pannonian Basin (Figure 2.1; see also e.g., Faccenna et al., 2014; Handy et al., 2015). From 35 Ma, the onset of fast rollback subduction triggered upper plate extension and the opening of the western Mediterranean basins and extension in the Rhodopes and Aegean Sea (Figure 2.1a - 2.1c; see also e.g., Faccenna et al., 2014). The subduction system in the western Mediterranean retreated towards Africa. After reaching the African continent at around 15 Ma, the trench retreated both towards Gibraltar and towards Adria (Figure 2.1d - 2.1f; see also e.g., Rosenbaum et al., 2002a; Spakman and Wortel, 2004). The retreat of this subduction system is reflected in the motion of continental blocks that dock in the Alborian sea and the Kabylies between 15 Ma and 10 Ma (Figure 2.1d and 2.1e: see also e.g., Rosenbaum et al., 2002a). East of Adria, the Hellenic trench retreat accelerated since 15 Ma due to the subduction of old Ionian oceanic crust (Figure 2.1d - 2.1f; see also e.g., Menant et al., 2016).

The motion of the Adriatic microplate before 20 Ma was mainly influenced by the African continent which induced a northwards motion of Adria relative to Europe (e.g., Le Breton et al., 2021; Ustaszewski et al., 2008). After that, the interplay between the advancing African continent, the indentation in the Alpine orogen to the north and the retreating subduction zones both west and east of Adria must have acted on the counterclockwise rotation and independent motion of Adria relative to Africa (e.g., Le Breton et al., 2017; Hinsbergen et al., 2014). In this study, we aim to test this hypothesis with thermomechanical modelling to learn more on the forces driving the motion of Adria.

2.3 Method

2.3.1 Conservation equations

To account for lithospheric-scale deformation over long timescales, the incompressible Stokes equations are solved, where the momentum and mass conservation equations are formulated as:

$$\frac{\partial \tau_{ij}}{\partial x_j} - \frac{\partial P}{\partial x_i} + \rho g_i = 0\,, \tag{2.1}$$

$$\frac{\partial v_i}{\partial x_i} = 0\,, \tag{2.2}$$

where x_i (i=1,2,3) denote spatial coordinates, τ_{ij} is the deviatoric stress tensor , P is the pressure, ρ is the density, g_i is the gravitational acceleration vector and v_i is the velocity in each direction.

We employed a simplified density parametrization, in which the density ρ depends on temperature T, reference temperature T_0, thermal expansivity α and reference density ρ_0:

$$\rho = \rho_0(1 - \alpha(T - T_0))\,. \tag{2.3}$$

Simultaneously with the mass and momentum conservation equations, we also solve the energy conservation equation which is given by:

$$\rho\, C_{\mathrm{p}} \frac{DT}{Dt} = \frac{\partial}{\partial x_i}\left(k \frac{\partial T}{\partial x_i}\right) + H_{\mathrm{SH}} + H_{\mathrm{A}} + \rho\, A\,, \tag{2.4}$$

where D/Dt denotes the material derivative, T is the temperature. C_{p} is the specific heat capacity of the material and k the thermal conductivity. A is the radiogenic heat production, the shear heating source term H_{SH} is prescribed in the following way:

$$H_{\mathrm{SH}} = \tau_{ij}(\dot{\varepsilon}_{ij} - \dot{\varepsilon}^{\mathrm{el}}_{ij})\,, \tag{2.5}$$

where $\dot{\varepsilon}_{ij}$ is the total deviatoric strain rate and $\dot{\varepsilon}^{\mathrm{el}}_{ij}$ the elastic strain rate component. The term H_{A} accounts for adiabatic heating and is given by:

$$H_A = T\alpha \frac{\partial P}{\partial x_i} v_i\,. \tag{2.6}$$

2.3.2 Rheology

The rheology is defined as visco-elasto-plastic, with the deviatoric strain rate composed of the following components:

$$\dot{\varepsilon}_{ij} = \dot{\varepsilon}^{\mathrm{el}}_{ij} + \dot{\varepsilon}^{\mathrm{dif}}_{ij} + \dot{\varepsilon}^{\mathrm{dis}}_{ij} + \dot{\varepsilon}^{\mathrm{pl}}_{ij} = \frac{\hat{\tau}_{ij}}{2G} + A_{\mathrm{dif}}\,\tau_{ij} + A_{\mathrm{dis}}\,(\tau_{\mathrm{II}})^{n-1}\,\tau_{ij} + \dot{\lambda}\frac{\partial Q}{\partial \tau_{ij}}\,, \tag{2.7}$$

where $\dot{\varepsilon}^{\mathrm{el}}_{ij}, \dot{\varepsilon}^{\mathrm{dif}}_{ij}, \dot{\varepsilon}^{\mathrm{dis}}_{ij} \dot{\varepsilon}^{\mathrm{pl}}_{ij}$ are the elastic, diffusion, dislocation and plastic strain rate, respectively. G is the elastic shear modulus ,$\hat{\tau}_{ij} = \frac{\partial \tau_{ij}}{\partial t} + \tau_{ik}\omega_{kj} - \omega_{ik}\tau_{kj}$ is the Jaumann objective stress rate, $\omega_{ij} = \frac{1}{2}(\frac{\partial v_i}{\partial x_j} - \frac{\partial v_j}{\partial x_i})$ is the spin tensor. A_{dif}, A_{dis} are diffusion and dislocation constants, respectively, n is the power-law exponent for dislocation creep. τ_{II} is the square root of the second invariant of the deviatoric stress tensor (i.e. $\tau_{\mathrm{II}} = (\frac{1}{2}\tau_{ij}\tau_{ij})^{\frac{1}{2}}$). $\dot{\lambda}$ is the magnitude of the plastic strain rate and Q is the plastic flow potential.

The rheological constants of the diffusion and dislocation creep mechanisms, A_{dif} and A_{dis}, respectively, can be expressed in the following generalized way:

$$A = B\; d^{-p}\; (C_{OH})^{r}\; \exp\left(-\frac{E + PV}{RT}\right). \tag{2.8}$$

Here E stands for the activation energy, R the gas constant, V the activation volume, B the specific prefactor constant, d the grain size, p the exponential factor of grain size, which does only apply for diffusion creep processes, C_{OH} the the water content and its exponential factor r. Table (2.2) summarizes the values of experimentally determined material parameters used to compute both creep constants. Both creep mechanisms are thus temperature- and pressure-dependent.

The magnitude of the plastic strain rate is determined by enforcing the Drucker-Prager yield-criterion:

$$F = \tau_{\mathrm{II}} - \tau_{\mathrm{Y}}, \quad \tau_{\mathrm{Y}} = \sin(\phi)P + \cos(\phi)c\,, \tag{2.9}$$

where τ_Y denotes the yield stress, ϕ is the friction angle and c the cohesion. In incompressible materials, plasticity is dilation-free (e.g., Kaus, 2010), which implies that the plastic flow potential function Q equals τ_{II}. Plasticity is only active when $F \geq 0$, such that $\dot{\lambda} F = 0$.

2.3.3 Numerical Implementation

The simulations were conducted using the thermo-mechanical code LaMEM (Kaus et al., 2016) where the conservation equations listed above are discretized using a staggered finite difference approach (Harlow and Welch, 1965). The material properties are advected using a Marker and Cell technique (Harlow and Welch, 1965). To solve the nonlinear system of equations LaMEM utilizes the PETSc infrastructure (Balay et al., 2024) employing distributed arrays (DMDA) that enable LaMEM to run on massively parallelized machines.

The effective viscosity of the nonlinear visco-elastic creep rheology is computed in every control volume by numerically solving the following nonlinear scalar equation $r(\eta_{\text{eff}})$ using a bisection algorithm (e.g., Popov and Sobolev, 2008):

$$r(\eta_{\text{eff}}) = \dot{\varepsilon}^*_{\text{II}} - \frac{\tau_{\text{II}}}{2G\Delta t} - A_{\text{dif}}\,\tau_{\text{II}} - A_{\text{dis}}\,(\tau_{\text{II}})^n\,, \tag{2.10}$$

in which the effective deviatoric stress is evaluated as:

$$\tau_{\text{II}} = 2\eta_{\text{eff}}\,\dot{\varepsilon}^*_{\text{II}}\,, \tag{2.11}$$

and the effective strain rate ($\dot{\varepsilon}^*_{ij}$) incorporates a term resulting from advected and rotated deviatoric history stress from the previous time step (τ^*_{ij}) as follows:

$$\dot{\varepsilon}^*_{ij} = \dot{\varepsilon}_{ij} + \frac{\tau^*_{ij}}{2G\Delta t}. \tag{2.12}$$

History stresses are advected using markers, which is followed by a distance-based averaging of the stress components on the corresponding control volumes of the staggered grid. The stress rotation algorithm is based on the numerical integration of the Jaumann objective stress rate, which gives asymptotically correct results for relatively large finite time steps (Gerya, 2019; Thielmann et al., 2015).

In case that plastic failure occurs, the corresponding effective viscosity is simply evaluated as:

$$\eta_{\text{eff}} = \frac{\tau_{\text{Y}}}{2\dot{\varepsilon}^*_{\text{II}}}\,. \tag{2.13}$$

The discretized system of nonlinear equations is solved with the help of the SNES nonlinear solution infrastructure of PETSc . We utilize a Picard linearization combined with a line search algorithm to facilitate the convergence of nonlinear iterations. The linearized system of algebraic equations is solved using the KSP solver interface of PETSc. We use 5 levels of coupled Galerkin multigrid V-cycle equipped with 5 smoothing sweeps of Richardson iteration with Jacobi preconditioner and damping factor of 0.5. Taking into account the resolution of the simulations ($512 \times 384 \times 128$), the processor partitioning ($8 \times 8 \times 4$) and the number of multigrid levels (5), the final coarse grid resolution per processor is $4 \times 3 \times 2$. The coarse grid system is solved redundantly on 64 cores using the SuperLU_DIST parallel sparse direct solver (Li and Demmel, 2003). The nonlinear solver tolerance was set to a relative value of 10^{-2}. We

compared this with simulations that have a relative tolerance of 10^{-4}, which yielded similar results (see Table 2.4, Simulation Tol).

2.4 Initial Model Setup

The following is a detailed description of the initial setup for the reference model (REF). The setup was developed by finding a reference model that best fits the first-order mechanisms in the Mediterranean since 35 Ma. It is based on various tectonic reconstructions of the area (e.g., Faccenna et al., 2014; Le Breton et al., 2021; Rosenbaum et al., 2002a) and was continuously updated based on the knowledge gained from running over 500 simulations.

The model setup consists of a rectangular area, with dimensions of 6000 km in the east-west direction and 3500 km in the south-north direction. It was shown that for models of this size, the Earth's curvature has a minor effect on the dynamics of the lithosphere and a Cartesian model box is therefore sufficient (Macherel et al., 2024). The vertical extension reaches down to a depth of 660 km (Figure 2.2a and 2.2b). On top of the crustal units, there is a 50 km thick layer of sticky air to account for a free surface (Crameri et al., 2012), so that the total depth of the model is 710 km. The material parameters of this layer are given in Table 2.1. The initial crustal configuration of the model features a diverse composition including a 10 km thick continental margin (thinned continental crust), 10 km thick oceanic crust and 35 km thick continental crust and 40 km thick orogenic crust (Figure 2.2a). Material parameters for these units are given in Table 2.1.

The initial setup displays several weak zones (WZ) in its crust and lithosphere (Figure 2.2a). As shown in Table 2.3 these different weak zones are characterised by different phases and depths. Initially the asthenosphere beneath the crust is homogeneous except for heterogeneities beneath the continental margin and the initial slabs that extend into the mantle. Tilted ellipses are inserted within the mantle lithosphere of the continental margin, creating a weak horizontal layer (2.A). These inclusions consist of a weaker mantle phase (Table 2.1 WZM). The Mediterranean region is characterised by the presence of three distinct subduction systems. The slab surface is composed of 15 km of oceanic crust and is overlaid by a 25 km thick weak zone that imitates the subduction channel. This facilitates the rollback of the slab, enabling it to rapidly reach a realistic geometry. In the western Mediterranean, a slab extends from the northernmost tip of the Adriatic microplate towards the Iberian Peninsula (Figure 2.2a and 2.2b). This western Mediterranean slab (WMS), which initially dips to the north, reaches a depth of 150 km. To the north of the trench, continental blocks can be found that are separated by weak material. In the eastern Mediterranean, the northeast-dipping Dinaric-Hellenic slab (DHS) is prescribed (Figure 2.2a and 2.2b). The Dinaric slab in the north is 300 km deep, while the Hellenic slab in the south initially reaches a depth of 600 km. The length of the slabs at 35 Ma was determined using the present-day length of subducted lithosphere observed in tomographic images (e.g., Piromallo and Morelli, 2003; Rappisi et al., 2022) and subtracting the amount of plate convergence since 35 Ma (e.g., Faccenna et al., 2001; Le Breton et al., 2021). Present-day tomographic images (e.g., Piromallo and Morelli, 2003; Rappisi et al., 2022; Šumanovac et al., 2017) show a slab gap beneath the Dinarides towards the north, which suggests that a slab-breakoff must have occurred. Based on the ages of calc-alkaline, subduction-related, magmatic rocks in the region, the slab breakoff is suggested to have occurred between approximately 37 and 22 Ma (e.g., Schefer et al., 2011; Handy et al., 2019). Therefore the initial setup includes a horizontal weak zone

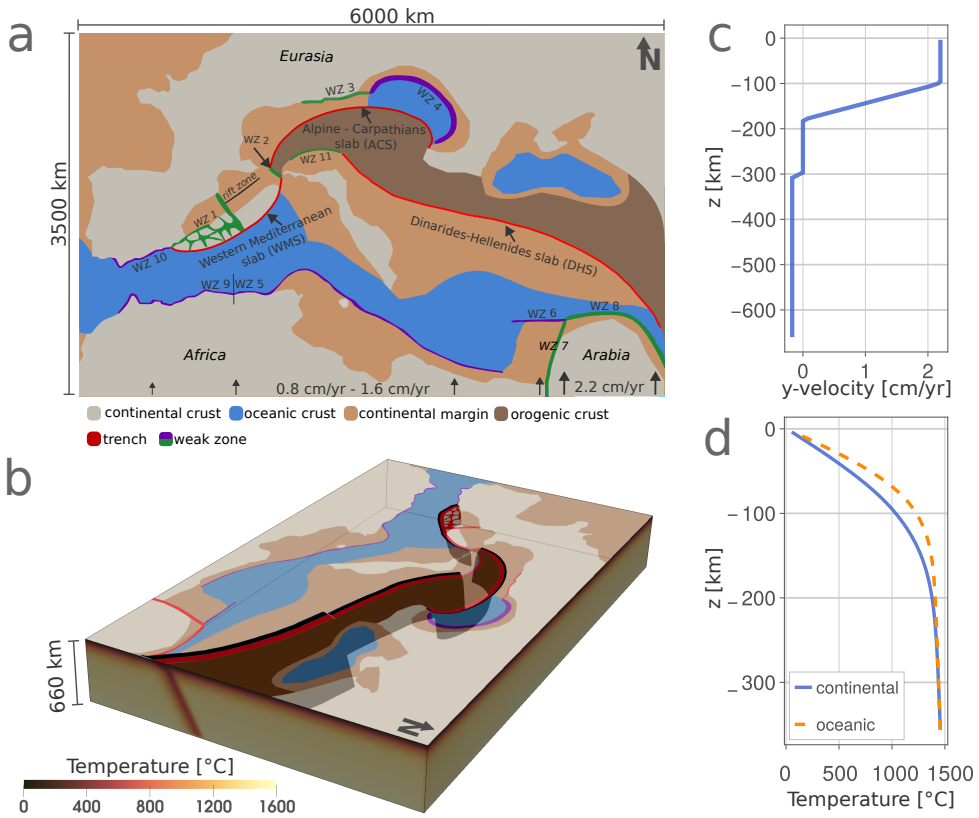

FIGURE 2.2: Initial model setup. (a) mapview of the setup at 35 Ma and the different phases of the crust. (b) 3D perspective of the model setup. (c) inflow boundary velocity with the example of the Arabian plate. (d) vertical temperature profile for continental and oceanic lithosphere.

in the mantle at a depth of 200 km in the northern part of the DHS, which initiates a slab break-off beneath the Dinarides. The Alpine-Carpathians slab (AlCS) in the north dips steeply southwards, with a curved trench geometry and a depth of 250 km (Figure 2.2a and 2.2b). The subduction system in the Alps has been simplified with the introduction of a continuous trench from the Alps in the west to the Carpathians in the east. However, the geological history of this region may have been more complex (e.g., Handy et al., 2010).

The African plate is separated from the Arabian plate by a vertical weak zone (Figure 2.2 a WZ7). During the simulation time of 35 Myr, both the African and Arabian plates are pushed northwards. The Arabian plate is pushed at a constant velocity of 2.2 $\frac{\text{cm}}{\text{yr}}$, the African plate is pushed at a velocity of 0.8 $\frac{\text{cm}}{\text{yr}}$ in its westernmost part and 1.6 $\frac{\text{cm}}{\text{yr}}$ in its easternmost part, with a linearly increasing plate velocity in between. For this purpose, the y-velocities at the southern boundary are prescribed as an inflow boundary condition. The inflow velocity is constant in the vertical direction down to a depth of 100 km, and decreases to zero between a depth of 100 and 180 km (Figure 2.2c). In order to compensate for the inflow of material, an outflow is prescribed at all boundaries between 300 km and 660 km depth. The magnitude of the outflow is uniform throughout the domain and precisely compensates for the inflow prescribed at the southern boundary. The top boundary above the sticky air layer is stress-free and all other boundaries are shear stress free and have zero normal velocity components. This type was chosen to mimic the convergence between Africa and Eurasia in a Eurasia-fixed reference frame. Alternative approaches that would prescribe the velocities of the lithospheric plates and incorporate stress-free boundary

TABLE 2.1: Material parameters of all model units of the reference simulation. SA is sticky air layer, As is asthenosphere, WM is weak mantle, WZ is weak zone, WZC is weak zone continental margin, CC is continental crust, OcC is oceanic crust, CM is continental margin and OrC is orogenic crust. Dislocation and diffusion creep laws are described in Table 2.2.

	SA	**AS**	**WM**	**WZ**	**WZC**	**CC**	**OcC**	**CM**	**OrC**
$\rho\left[\frac{kg}{m^3}\right]$	1000	3300	3300	3300	2800	2800	2850	3300	3300
dislocation	$\eta_{eff} = 10^{19} Pas$	Dry Olivine	Wet Olivine	$\eta_{eff} = 10^{19} Pas$	Dry Olivine	Quarzite	Plagioclase	Wet Quarzite	Wet Quarzite
diffusion	-	-	Dry Olivine	Wet Olivine	Dry Olivine	-	-	-	-
c [MPa]	-	20	20	-	$10 - 20$	20	10	20	20
c sof. [MPa]	-	2	2	-	$1 - 2$	2	1	2	2
$\phi[^\circ]$	-	30	30	-	$4.5 - 12.5$	30	1	10	30
ϕ sof. $[^\circ]$	-	3	3	-	$0.45 - 1.25$	3	0.1	1	3
A $[Wm^{-3}]$	-	2×10^{-8}	2×10^{-8}	2×10^{-8}	2×10^{-8}	2×10^{-6}	2×10^{-7}	2×10^{-6}	2×10^{-6}

* A constant shear modulus $G = 5 \times 10^{10}$ Pa is used.
* A constant conductivity $k = 3\,\mathrm{Wm^{-1}K^{-1}}$ (SA: $k = 100\,\mathrm{Wm^{-1}K^{-1}}$) and heat capacity $C_p = 10^3\,\mathrm{Jkg^{-1}K^{-1}}$ (SA: $C_p = 10^6\,\mathrm{Jkg^{-1}K^{-1}}$) is used.
* A constant thermal expansion $\alpha = 3 \times 10^{-5}\,\mathrm{K^{-1}}$ is used (not used for SA).

TABLE 2.2: Creep law parameters for the creep laws listed in Table 2.1.

Dislocation creep	B $[\mathrm{Pa}^{-\mathrm{n}}\,\mathrm{s}^{-1}]$	E $[\mathrm{J\,mol}^{-1}]$	V $[\mathrm{m}^3\,\mathrm{mol}^{-1}]$	n	p	r
Dry Olivine[a]	1.1×10^5	530×10^3	11.0×10^{-6}	3.5	0.0	0.0
Wet Olivine[a,d]	1.6×10^3	520×10^3	10.0×10^{-6}	3.5	0.0	1.2
Plagioclase (An_{75})[b]	3.3×10^{-4}	238×10^3	0.0×10^{-6}	3.2	0.0	0.0
Quartzite[b]	6.7×10^{-6}	156×10^3	0.0×10^{-6}	2.4	0.0	0.0
Wet Quartzite[b]	3.2×10^{-4}	154×10^3	0.0×10^{-6}	2.3	0.0	0.0
Diffusion creep	B $[\mathrm{Pa}^{-\mathrm{n}}\,\mathrm{s}^{-1}]$	E $[\mathrm{J\,mol}^{-1}]$	V $[\mathrm{m}^3\,\mathrm{mol}^{-1}]$	n	p	r
Dry Olivine [a,c]	1.5×10^9	375×10^3	10.0×10^{-6}	1.0	3.0	0.0
Wet Olivine [a,c,d]	2.5×10^7	375×10^3	8.0×10^{-6}	1.0	3.0	0.8

[a] Hirth and Kohlstedt (2003).
[b] Ranalli (1995).
[c] A constant grain size of $d = 10^{-3}$ m is used.
[d] A water content of $C_{OH} = 1000\,\mathrm{H}/10^6\mathrm{Si}$ is used.

TABLE 2.3: The parameters for all weak zones that are part of the crustal configuration (Figure 2.2 a).

	WZ 1	**WZ 2**	**WZ 3**	**WZ 4**	**WZ 5**	**WZ 6**	**WZ 7**	**WZ 8**	**WZ 9**	**WZ 10**	**WZ 11**
phase	WZ	WZ	WZ	WZC	WZC	WZC	WZ	WZ	WZC	WZC	WZ
depth [km]	100	100	60	40	65	40	240	40	65	65	80
c [MPa]	-	-	-	20	10	20	-	-	20	20	-
ϕ [°]	-	-	-	4.5	5.0	4.5	-	-	12.5	12.5	-

conditions in the mantle are also conceivable. This could lead to a different timing of subduction dynamics close to the boundaries. However, our research focus is on the Adriatic microplate and once the subduction systems reach the vicinity of Adria they are unlikely to be strongly influenced by the lateral boundary conditions.

The initial temperature structure of the model is calculated based on the halfspace cooling model (e.g., Turcotte and Schubert, 2002):

$$T = T_{surf} + \left(T_{Mantle} - T_{surf}\right) \mathrm{erfc}\left(\frac{d}{2\sqrt{\kappa\, t_{age}}}\right), \tag{2.14}$$

where T_{surf} is the surface temperature (0 °C) at the surface of the slab which reaches into the asthenosphere. $T_{Mantle} = 1350$ °C is the temperature at the lithosphere-asthenosphere boundary, d is the depth, $\kappa = 10^{-6}$ $\mathrm{m^2 s^{-1}}$ is the thermal diffusivity. For oceanic crust t_{age} is 60 Myr and for continental crust and continental margin t_{age} is 120 Myr. A gradient of 0.3 K km^{-1} is added to account for the adiabatic gradient in the asthenosphere. To ensure a more realistic initial temperature setup and account for radiogenic heating, the energy equation is solved for 0.2 Myr and 20 timesteps before the simulation begins. The resulting temperature structure is displayed in Figure 2.2b. Figure 2.2d shows the geothermal gradients for oceanic and continental lithosphere, respectively. A temperature and effective viscosity cross-section is displayed in the Appendix B. Phase changes, such as the transition from olivine to wadsleyite, are not considered, as we cannot fully account for them in an incompressible formulation of the Stokes equations. However, this could have an impact on the timing and dynamics of subduction zones.

During the simulation, the effective viscosity is limited to be between 10^{19} Pas and

10^{24} Pas. The bottom temperature is fixed at 1600 °C. The model domain is discretized using a grid of $512 \times 384 \times 128$ grid cells in x, y, z-direction. This results in a spatial resolution of about 12 km × 9 km in the x and y directions, respectively, and a vertical resolution ranging from 6 km in the lower mantle to 4.3 km in the lithosphere. The grid spacing in the z-direction is variable. There are 94 cells between the bottom of the model and -100 km, 24 cells between -100 km and 5 km, and 10 cells between 5 km and 50 km. Plastic softening is applied for all phases, which means that between 10% and 60% of accumulated plastic strain, the cohesion c and the friction angle ϕ are reduced linearly by 90%.

2.5 Results

Over 500 3D simulations were conducted to determine a reference model (REF) that best fits the motion of the various subduction-collision fronts, the continental blocks in the Western Mediterranean (Corsica-Sardinia, Al-Ka-Pe-Ca (see Figure 2.1)) and the motion and rotation of Adria compared to geological reconstructions of the region (section 2.2). Indeed, the REF model reproduces well the trench retreat of the different subduction zones (e.g. ca. 1000 km retreat of the Calabrian and Hellenic subduction zones). We compared the total amount of counterclockwise rotation and northward motion of the Adriatic microplate. The REF model reproduces well the rotation of Adria, while the overall northward motion of Adria is lower in the model (ca. 170 km) compared to the tectonic reconstructions (ca. 280 km). The relation between northward motion of Adria and the subduction dynamics in the Alps is discussed in section 6.3. More information on the quantitative comparison between the REF model and tectonic reconstructions is available in Appendix 2.C.

The following section provides a detailed description of REF, with particular attention paid to the dynamics around the Adriatic microplate. To visualize the subducting slabs, a 80 km thick layer beneath the slab surface and the crust composed of mantle material is used to track the motion. The results will be displayed with reference to geological time (Ma), with 35 Ma marking the starting point of the simulation. We provide animations of the key simulations in the supporting information.

2.5.1 Reference Simulation

The subduction dynamics of REF is dominated by rollback subduction. Generally, the WMS retreats to the south, the DHS retreats to the southwest and the AlCS retreats to the north (Figure 2.3). The slab retreat is influenced by various parameters, such as the extent and shape of the continental and oceanic crust or the temperature structure of the lithosphere. Below, we describe each subduction system in more detail.

At 35 Ma, the WMS extends from the northeast to the southwest and initially reaches a depth of 150 km (Figure 2.3a). The curved trench retreats at an angle perpendicular to its trench-line, with the central part of the slab retreating at a faster rate than its edges. This results in a curved trench geometry (Figure 2.3b and Figure 2.4a). The motion of the trench can be observed by tracking the motion of the continental blocks to the northwest of the trench. The central blocks move in a southerly direction towards Africa, while the western blocks rotate in a clockwise direction towards the west and eventually dock at the Iberian Peninsula at 20 Ma (Figure 2.3c). The easternmost block, which represents the Corsica-Sardinia continental block, rotates anticlockwise towards the east and subsequently settles into a north-south orientation (Figure 2.3d - 2.3f). A rift system opens during the retreat of the WMS slab. A north-south oriented rift zone in the center of the Mediterranean is active between 28

Ma and 20 Ma while the WMS is propagating towards Africa (Figure 2.3b and 2.3c). Finally, around 20 Ma, the subduction zone reaches the African continent, resulting in a slab break-off at approximately 16 Ma (Figure 2.4b). This break-off propagates to the east and west, subdividing the subduction zone into the Gibraltar slab (GS) to the west and the Apennine-Calabrian slab (ApCS) to the east (Figure 2.4c). This results in a relatively narrow GS that extends down to 660 km depth and retreats to the west (Figure 2.4h and 2.4i). As the GS retreats, the gap between the Iberian Peninsula and Africa almost closes. Concurrently, the slab break-off progresses at a faster rate to the east, resulting in the ApCS retreating in that direction (Figure 2.4c).

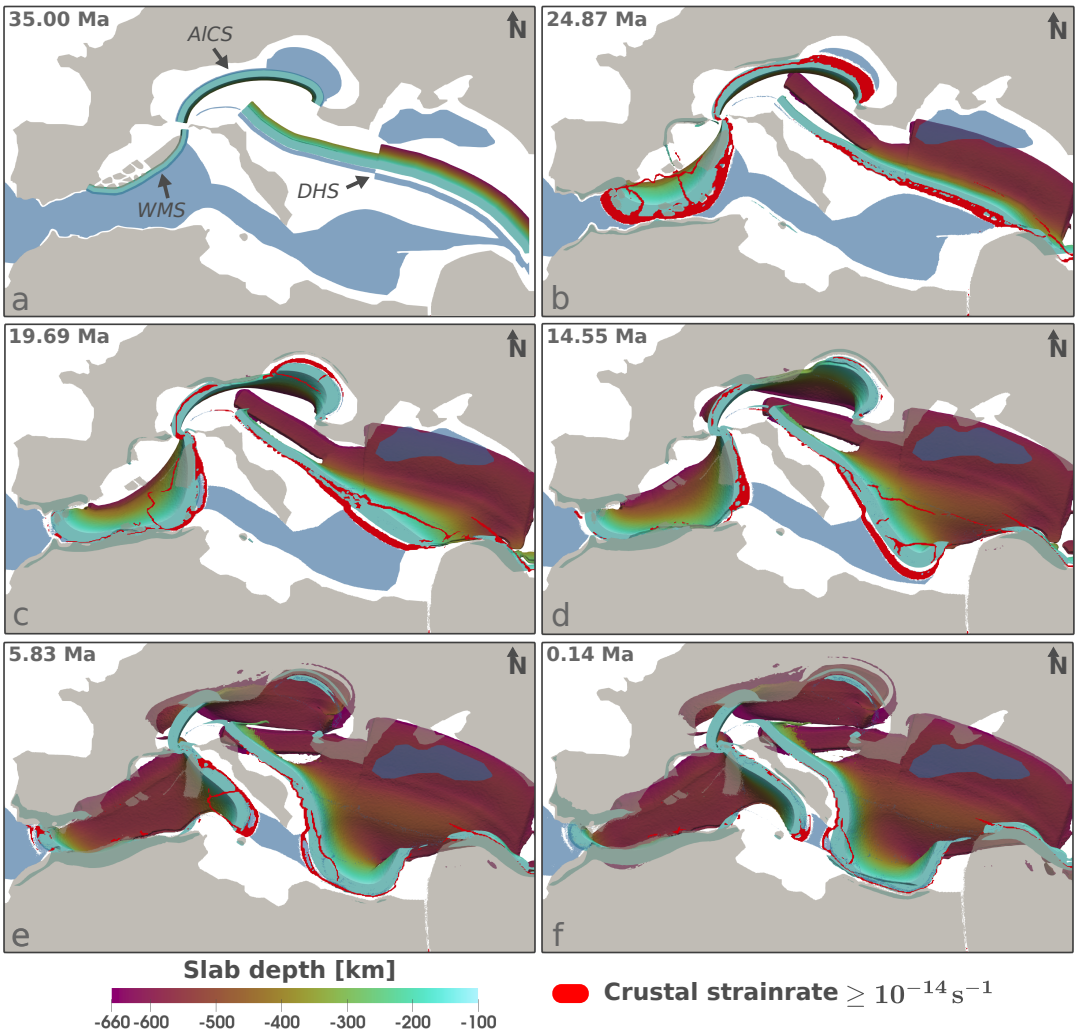

FIGURE 2.3: Evolution of the reference model (REF) over 35 Myr. The figure shows six different timesteps of a mapview of the 3D simulation, with the continental crust (grey) and oceanic crust (blue) depicted slightly translucent. (a) shows the abbreviations for the three different slabs. The red colour highlights the parts of the crust where significant strain rate (second invariant of the strain rate tensor) occurs. The colours ranging from violet to green indicate the depth of the subducted mantle lithosphere between -120 km and -660 km. See Movie S1 in the Supporting Information for an animation of the simulation.

At 20 Ma, the trench of the ApCS is oriented north-south (Figure 2.3c). Subsequently, the Ionian oceanic crust begins to be subducted in the south, while the rift zone opens between the Corsica-Sardinia continental block and Adria (Figure 2.3d - 2.3f), and slab retreat accelerates in this region. The northern part of the ApCS then

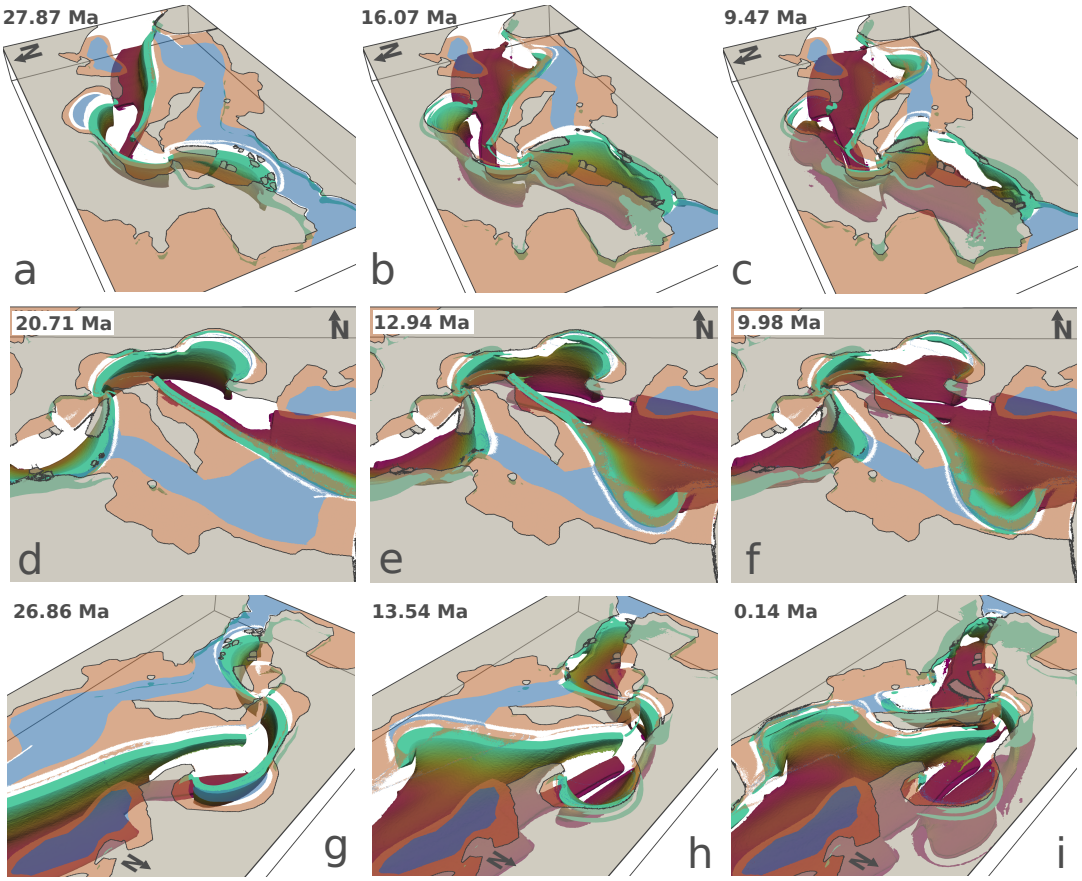

FIGURE 2.4: Different viewing angles of REF. The upper row presents the model box from the northwest, the middle row shows a close-up view from the south, and the lower row displays the 3D box from the northeast. The figure shows different parts of the crust, including continental crust (grey), thinned continental crust (orange-brown) and oceanic crust (blue). Subducted lithosphere is shown between a depth of 115 km and 660 km with the colour scheme identical to that of Figure 2.3.

slows down as it partially consumes the Adriatic continental microplate, while the southern part of the ApCS continues to subduct Ionian oceanic crust resulting in a curved trench geometry of the ApCS (Figure 2.3e and 2.3f). Between 35 Ma and 25 Ma the AlCS retreats northward at a constant velocity across the trench maintaining the initial trench geometry (Figure 2.3a and 2.3b). Since 25 Ma the retreat of the eastern part of the slab has accelerated towards the northeast, consuming the oceanic crust in that region (Figure 2.3c). This leads to a bending of the trench line to the east (Figure 2.3c). At approximately 21 Ma, a slab break-off occurs in the central part of the slab (Figure 2.4d), initiating a slab tearing both to the west and to the east (Figure 2.4e). Initially, the slab tearing propagates at approximately the same velocity in both directions, but then it accelerates to the east around 12 Ma (Figure 2.4f). It quickly acts along the curved trench, resulting in a complete slab break-off in the east at 10 Ma (Figure 2.4f). In contrast, to the west, slab tearing largely ceases around 10 Ma, resulting in a subduction system that remains stagnant in the northwest of Adria (Figure 2.4d - 2.4f). As illustrated in Figure 2.3d - 2.3f, the position of the slab in the west has remained relatively stable over the past 15 Myr. Simultaneously, the DHS retreats to the southwest (Figure 2.3a - 2.3c). At 35 Ma, a weak zone vertically separates the DS in the mantle, causing the lower part of the slab to sink rapidly to a depth of 660 km (Figure 2.4g). North of the Arabian plate, the DHS

breaks off. The slab tearing progresses towards the west until approximately 15 Ma (Figure 2.3b - 2.3d). As the DHS retreats to the southwest, it initially only consumes continental margin (Figure 2.4g). At 25 Ma, the southern part of the DHS reaches oceanic crust (Figure 2.3b) and the slab retreat accelerates to the south, resulting in a curved trench (Figure 2.4h). Additionally, subduction of continental margin to the north continues at a slower rate during the fast slab retreat in the south. Between 21 Ma and 0 Ma the DHS consumes almost the entire oceanic crust southeast of Adria (Figure 2.4i). At present-day, the trench almost reaches the African continental margin and the southern tip of Adria (Figure 2.3f and Figure 2.4i). Although the northern part of the slab reaches Adria along its eastern boundary, the retreat was much slower than in the south. Consequently, the northern slab only extends to a depth of approximately 300 to 400 km (Figure 2.4i). South of Adria, the ApCS and the DHS are in close proximity, with less than 100 km of oceanic crust remaining unsubducted (Figure 2.3f).

2.5.1.1 Mantle Flow

This section provides a detailed description of asthenospheric mantle flow in REF. In general, two types of flow patterns can be observed: poloidal flow, which circulates in a vertical plane, and toroidal flow around the slab edges, which circulates horizontally.

We begin by examining the poloidal flow patterns in the asthenosphere. The direction and magnitude of asthenospheric flow can be observed in Figure 2.5. The DHS retreats to the southwest, inducing trench perpendicular flow between 35 Ma and 25 Ma. This is particularly pronounced in the southern half of the slab (Figure 2.5a and 2.5b). Figure 2.5g shows a vertical cross-section through the model. It can be observed that the retreat of the DHS introduces poloidal flow cells to the southwest and northeast of the slab. The poloidal flow cell to the northeast is located in the lower half of the asthenosphere, above the horizontal slab piece that lies at the bottom of the model. As the slab remains fully connected, the slab pull forces are partly transmitted through the subducting slab to the lower part of the subduction. The greatest velocities are observed in the back-arc of the system, where asthenospheric material ascends. This results in the formation of a poloidal flow cell between the back-arc extensional area and the flat slab at the bottom of the upper mantle. The second poloidal flow cell is situated to the southwest of the slab (Figure 2.5g). It is located below the lithosphere, which is undergoing a northward motion. This results in the formation of a clockwise rotational flow cell. The magnitude of mantle flow associated with poloidal flow in REF is typically smaller than horizontal mantle flow associated with toroidal flow (Figure 2.5). The following section will therefore concentrate on the horizontal mantle flow. The retreat of the different subduction zones introduces horizontal pressure gradients in the asthenosphere, which are the main drivers of mantle flow in the upper mantle. To this end, we introduce a new variable, the dynamic pressure P_{dyn}, which in this study is defined as the pressure P minus the average lithostatic pressure per depth level (Figure 2.6). Between 25 Ma and 21 Ma the DHS slab breaks off north of the Arabian plate, resulting in a slab tearing from east to west until 14 Ma (Figure 2.5a - 2.5d). Through the rapid slab tearing, a strong toroidal flow around the southern slab edge evolves which is strongest around 18 Ma (Figure 2.5c). After 14 Ma a curved trench develops in the south and the magnitude of the toroidal flow gradually weakens until present-day (Figure 2.5d - 2.5f). Nevertheless, the slab is still retreating, as evidenced by the remaining trench perpendicular flow (Figure 2.5f). The northern part of the DHS generally exhibits a

slower rate of retreat than the southern part, which results in a slab bending between north and south.

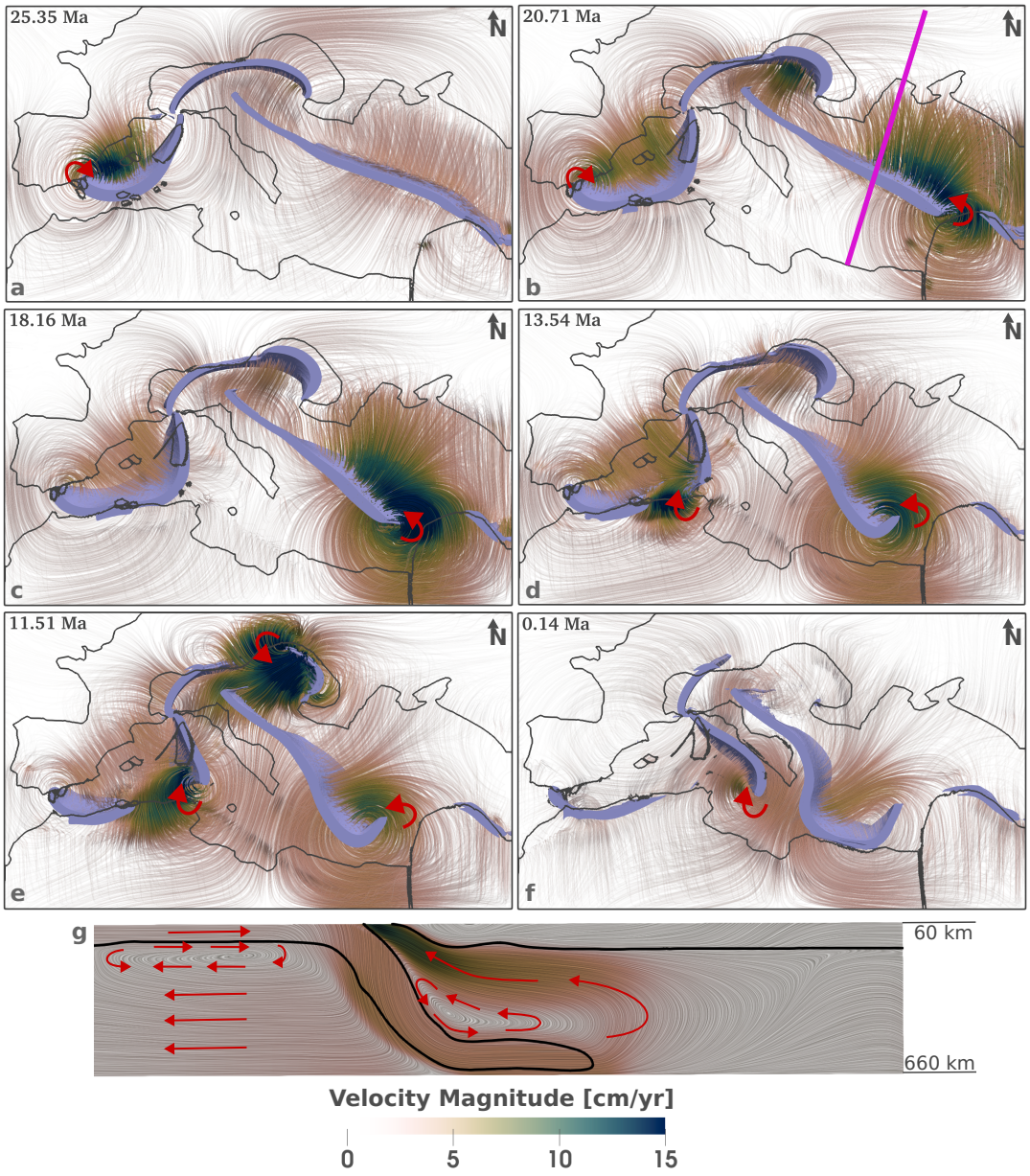

FIGURE 2.5: Mantle flow of REF. (a-f) The grey lines outline the edges of the continents, whereas the purple colour represents the subducting lithosphere between a depth of 120 km and 400 km. Mantle flow directions are displayed by flow lines, coloured by flow magnitude. The red arrows indicate the direction of the toroidal flow cells, while the pink line in (b) represents the location of the vertical cross-section depicted in (g). (g) SW-NE vertical cross-section through the model box. The red arrows indicate the flow direction of the poloidal flow cells, while the black line displays the 1300°C isotherm.

The WMS first induces a trench perpendicular flow in the back of the subduction zone, caused by the retreat of the slab (Figure 2.5a - 2.5c). On the western edge of the subduction zone, this is accompanied by a clockwise rotating toroidal flow. This continues until the WMS breaks off at Africa, which opens a slab gap (Figure 2.5d and Figure 2.6c). The retreat of the slab to the south has resulted in a significant P_{dyn} gradient between the back of the slab and the front (Figure 2.5d, 2.5e, 2.6c, 2.6d).

After the slab gap has opened, a toroidal flow cell develops around the southern edge of the ApCS, resulting in the compensation of horizontal P_{dyn} differences (Figure 2.6c and 2.6d). In the western part of the slab gap, in the vicinity of the GS, the asthenospheric flow is nearly perpendicular to the trench (Figure 2.5e). Following the slab break-off, the toroidal flow accelerates the retreat of the ApCS to the east, ultimately resulting in a curved trench geometry of the ApCS (Figure 2.5d - 2.5f and Figure 2.6d - 2.6f).

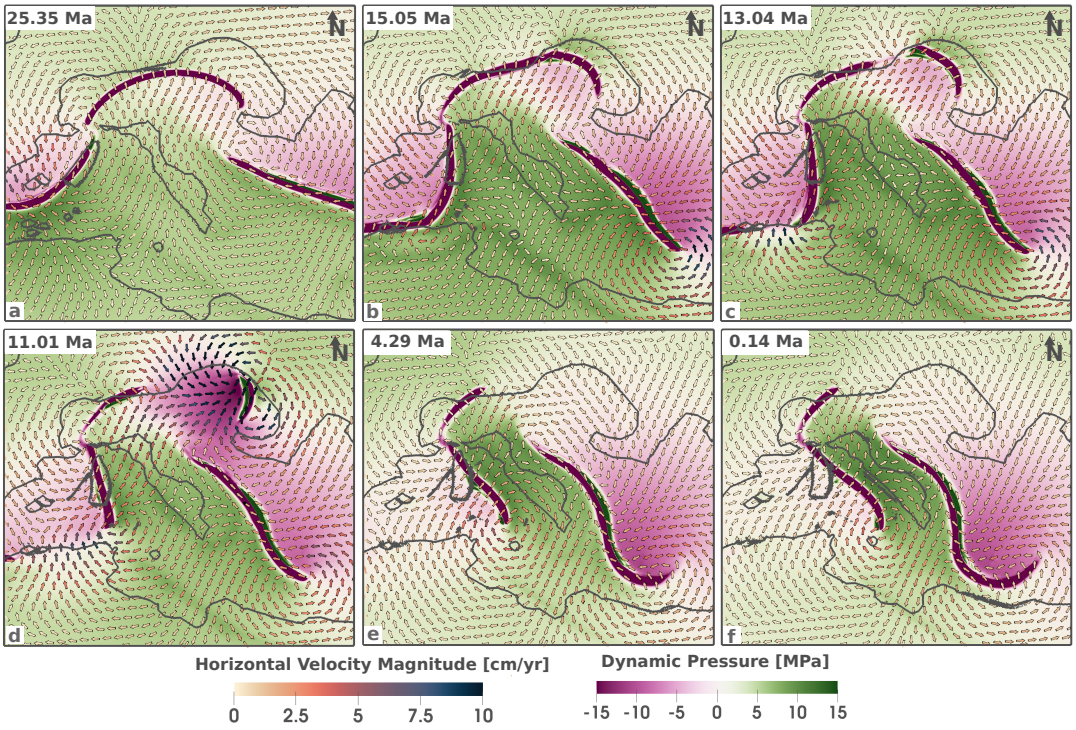

FIGURE 2.6: Dynamic pressure variations at a depth of 300 km. Arrows indicate the direction of horizontal mantle flow, with colours representing the magnitude of the horizontal flow.

The ApCS and the DHS retreat towards each other, creating a region of elevated P_{dyn} between the two slabs (Figure 2.6). From 35 Ma to 25 Ma, the mantle flow between these two slab is directed northwards. However, as the toroidal flow cells south of the ApCS and the DHS are advancing, they cause a southward-directed mantle flow underneath the southern part of Adria (Figure 2.6b), which leads to a switch in asthenospheric flow. After 20 Ma, a transition is observed in the asthenospheric flow beneath Adria. The flow direction undergoes a change from northward in the northern region to southward beneath the southern half of Adria (Figure 2.6b - 2.6f). This pattern can still be observed at present-day (Figure 2.6f).

Between 35 Ma and 25 Ma, the AlCS retreats to the north, inducing a trench perpendicular mantle flow (Figure 2.5a). After 25 Ma, the slab retreat accelerates to the east, which increases the magnitude of trench perpendicular mantle flow in this region (Figure 2.5b). This is followed by the slab break-off in the center of the AlCS. Consequently, an anticlockwise rotating toroidal flow cell develops in the eastern region of the slab gap (Figure 2.5d - 2.5e and Figure 2.6b - 2.6d). The toroidal flow rapidly accelerates, resulting in the complete break-off of the slab in the east at 9 Ma (Figure 2.6d and 2.6e). For approximately 3 Myr, a combination of strong downward-oriented vertical flow and toroidal flow can be observed (Figure 2.5e). On the western edge of

the slab gap, no toroidal flow develops. South of the slab, to the west, the P_{dyn} remains relatively high throughout the simulation, due to asthenospheric escape flow from the south. Conversely, to the east, a region with low P_{dyn} develops as the trench retreats at an accelerated rate after 25 Ma (Figure 2.6). Subsequently, a trench parallel flow establishes south of the AlCS around 15 Ma, which lowers the P_{dyn} difference (Figure 2.6b - 2.6d). This mantle flow distinctly weakens after approximately 10 Ma when the P_{dyn} is almost entirely equilibrated (Figure 2.6e and 2.6f).

2.5.1.2 Plate Motion of Adria

The complex subduction dynamics discussed above also leads to an intricate pattern of plate motion. This section gives a detailed description of the temporal evolution of Adria's plate motion.

Figure 2.7 displays the plate motion of the Adriatic microplate and the surrounding area, like the African continent in the south or the continental blocks within the western Mediterranean. Between 35 Ma and 22 Ma, Adria moves in conformity with Africa to the north (Figure 2.7a). After 22 Ma, the motion of Adria and Africa starts diverging partially. The southern part of Adria still moves exactly in the same direction as Africa, whereas the northern part of Adria undergoes a change in direction to the northwest (Figure 2.7b). As illustrated in Figure 2.7a and 2.7b, after 22 Ma the northernmost extent of Adria moves approximately in the same northwest direction as the retreating trench of the AlCS, situated to the north. Overall, this leads to an anticlockwise rotation of the Adriatic microplate (Figure 2.8a).

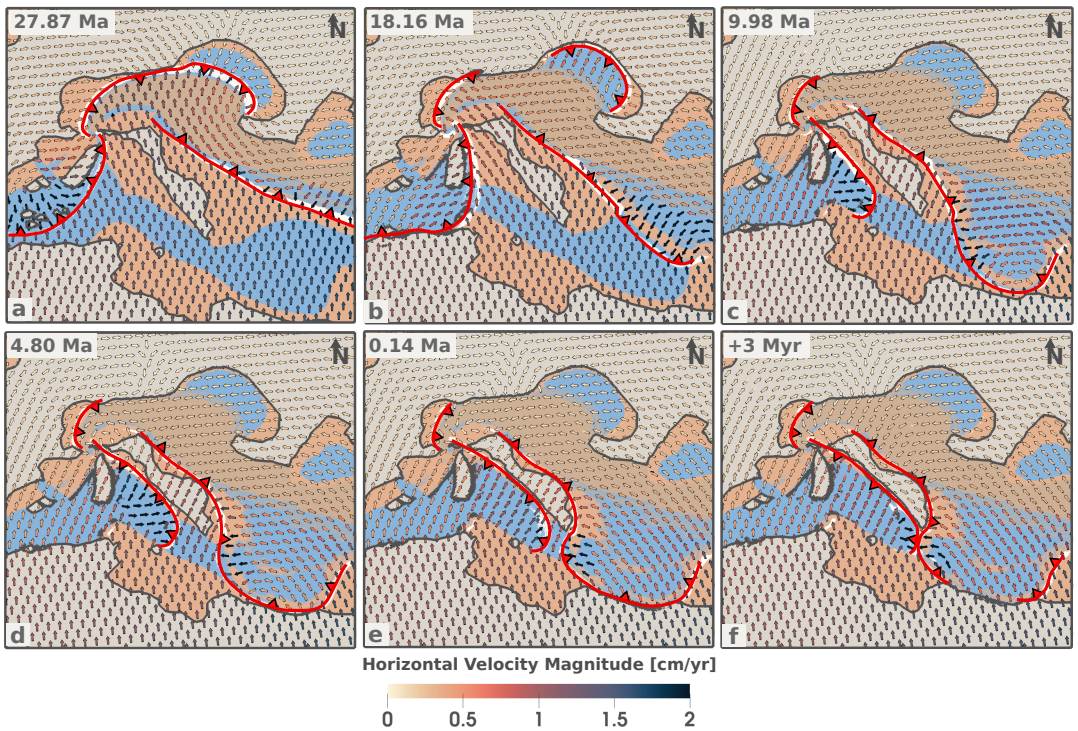

FIGURE 2.7: Plate motion at a depth of 10 km. Arrows indicate the direction of plate motion, while the magnitude is represented by the colour of the arrow. Red lines indicate the trench position of the different subduction systems, while the triangles mark the dipping direction of the slab. (f) presents the results of the simulation after a simulation time of 38 Myr.

The southern part of Adria moves in the same direction as Africa until approximately 13 Ma (Figure 2.8c). Subsequently, the southern part of Adria begins to move differently from Africa, by shifting to the northeast, as the entire Adriatic plate rotates (Figure 2.7c - 2.7e). Between 13 Ma and present-day, the change in direction of southern Adria's plate motion is quite constant (Figure 2.7c - 2.7e, Figure 2.8c). Furthermore, both the southern and the northern parts of Adria rotate to the northeast (Figure 2.8a). At 13 Ma, the angles between "Adria northeast" (green dot in Figure 2.8a) and "Adria south" (blue dot in Figure 2.8a) were approximately 40° offset from each other. However, the direction of plate motion of these two parts converged until the present day, when both are moving in approximately the same direction (2.8c). From 5 Ma, Adria rotates around a rotation pole located to the northwest (purple dot in Figure 2.8a), as this part of Adria almost stops moving around this time (2.8b).

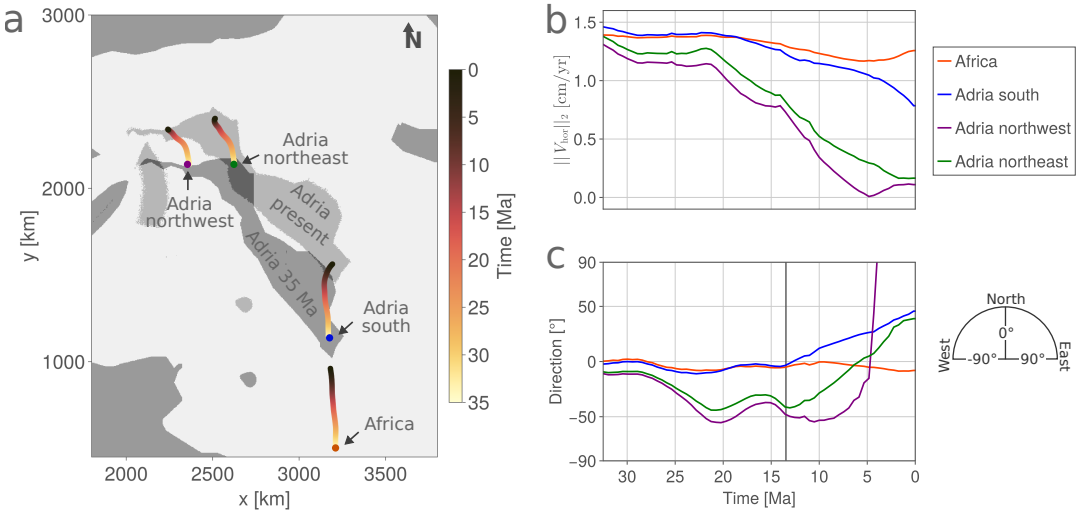

FIGURE 2.8: (a) visualises the plate motion of four selected tracers in the crust. Initially, these tracers are located at a depth of 10 km. Different shades of grey depict the initial position of Adria and Adria's position at present-day. (b) plots the magnitude of plate motion of the four tracers over time. (c) plots the direction of the tracers over time. The direction is indicated by the angle, where 0° represents a northward direction, -90° indicates a westward motion, and 90° represents an eastward motion.

In the initial stages of the simulation, the entire Adriatic microplate moves with the same magnitude as the African plate (Figure 2.7a). At around 22 Ma, the northern part of Adria decelerate in comparison to the southern region (Figure 2.8b). From that point onwards, the velocity constantly decreases until 5 Ma (Figure 2.8b). The decreasing velocity in the northern part of Adria is in alignment with the observed slowing of the Alpine subduction (Figure 2.7a - 2.7c, Figure 2.8b). The southern half of Adria starts to slow down around 18 Ma (Figure 2.8b). This occurs at a slower rate than in the northern part (Figure 2.8b). From 18 Ma onwards, the velocity of the southern part of the Adriatic plate motion decreases at a more rapid rate than that of the African plate (Figure 2.7b).

The REF simulation was run for an additional 5 Myr, and Figure 2.7f illustrates that the direction of Adria changes abruptly from northeast to southeast at approximately 38 Myr since the beginning of the simulation. This abrupt change happens when the Calabrian subduction zone and the Hellenic subduction zone converge south of Adria, cutting off the connection between the Adriatic microplate and the African continent.

2.5.2 Parameter study

Over the course of this study, many simulations were conducted with varying configurations in order to identify a model that adequately represents the first-order processes observed in the Mediterranean. While we cannot present all models, we here discuss a representative selection in which specific parameters are changed with respect to REF, to obtain an understanding of how variations in the model parameters affect the outcome. These simulations are summarized in Table 2.4.

2.5.2.1 Influence of Weak Zones

The weak zones of the model are very sensitive to changes in material properties. Small changes in friction angle quickly lead to changes in subduction dynamics, as observed in Sim12 and Sim13 (Table 2.4). In Sim12 the friction angle of weak zone 4, which encompasses the Carpathians region, is decreased from 4.5° (REF) to 3.5°. This leads to an accelerated slab tearing. However, if the friction angle is increased to 5.5° (Sim13), the slab does not break off entirely, so that part of the slab is still attached after 35 Myr of simulation time. Similar sensitivity tests were conducted for weak zone 9, in the region of the Gibraltar slab, and weak zone 5, at the northern boundary of the African plate. In Sim10 the friction angle of the weak zone 9 is decreased to 11.5° leading to a faster slab retreat of the Gibraltar slab, while an increase of friction angle to 13.5° reduces the retreat velocity in the region and the slab starts to break off in the mantle. The strength of the weak zone 5 is of critical importance, as it determines the retreat velocities of both the Apennine-Calabrian and Dinaric-Hellenic subduction zones. In Sim1, in which the friction angle of weak zone 5 is decreased to 4.5°, the aforementioned subduction zones already converge after 34 Myr, whereas in REF this only happens after 37 Myr. Sim5 has a stronger weak zone 5 ($\phi = 5.25°$), so that the subduction zones have not yet converged after 40 Myr. Changing the friction angle of the weak zone also affects the interaction of different subduction zones. If the friction angle of weak zone 5 is larger, the propagation of the slab break-off at Africa is slower. This results in a longer period of lateral connection between the GS and the ApCS compared to the REF. In the case of the Gibraltar slab, this results in a generally lower retreat velocity, which leads to a complete slab break-off. This is not the case if the friction angle of weak zone 5 is distinctly lower (Sim1).

2.5.2.2 Mantle Rheology

The simulation results are also highly sensitive to the mantle rheology. A combination of diffusion and dislocation is used and by changing parameters such as the activation volume within the error bars given by Hirth and Kohlstedt (2003), the mantle dynamics changes drastically (see Sim18, Sim19, Sim20). By changing the activation volume from $V_{\text{dis}} = 11 \times 10^{-6}$ m^{3}mol^{-1} to $V_{\text{dis}} = 8 \times 10^{-6}$ m^{3}mol^{-1} and $V_{\text{dif}} = 10 \times 10^{-6}$ m^{3}mol^{-1} to $V_{\text{dif}} = 7 \times 10^{-6}$ m^{3}mol^{-1} the mantle rheology becomes remarkably weaker and thus the slab retreat velocities are significantly higher (Sim20).

2.5.2.3 Subduction of Adriatic Lithosphere north of Adria

A subduction of Adriatic lithosphere is not observed in REF. In Sim28, there is no initial AlCS. In this case, the initiation of a subduction process, whereby Adriatic lithosphere is subducted beneath Europe, can be observed to the north of Adria after 2 Myr. A similar behaviour can be observed if the weak zone north of Adria (WZ 11) is deeper than in REF. If the depth of the weak zone initially reaches 160 km instead

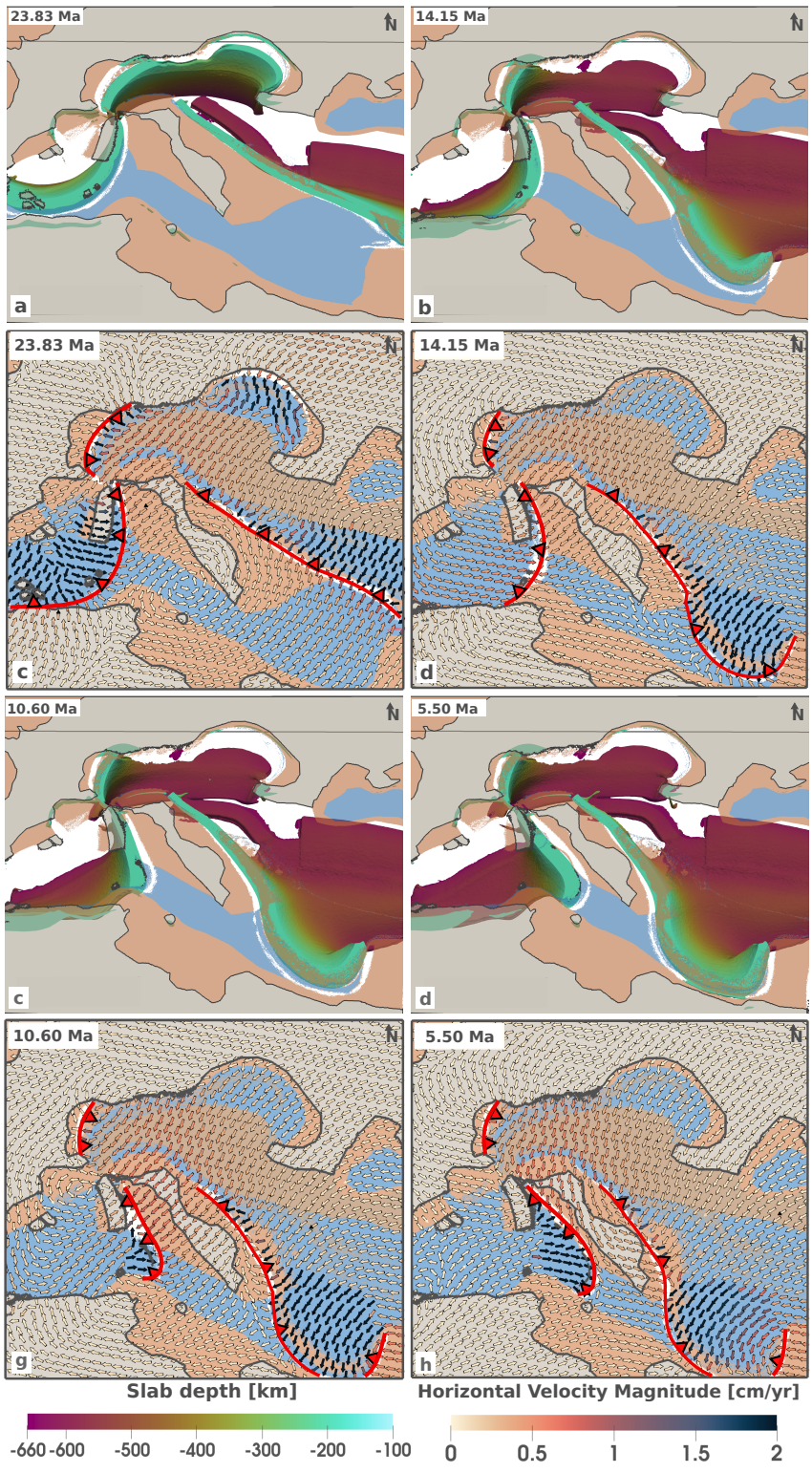

FIGURE 2.9: Simulation results of Sim7, without any northward motion of Africa and Arabia. (a–d) show the subduction dynamics at four different timesteps. The colours ranging from violet to green indicate the depth of the subducted mantle lithosphere. (e–h) show the plate motion and the trench locations at the different timesteps. The colours of the arrows indicate the magnitude of plate motion.

of 80 km (Sim31), a subduction north of Adria is initiated at 25 Myr, after the Alpine subduction has ceased.

2.5.2.4 Extent of Ionian Crust

The extent and shape of the different crustal phases also have a significant impact on the simulation results. Modifying the extent of the oceanic corridor south of Adria influences the subduction dynamics. In Sim24, the oceanic corridor is narrower than in REF, which results in a slower retreat velocity of the ApCS. This, in turn, causes the subduction to cease retreating without reaching the same position as in REF. A wider corridor, however, facilitates the retreat of the Apennine-Calabrian subduction zone (Sim25).

TABLE 2.4: Overview of the numerical simulations and the parameters modified in each case.

Simulation	**Modified parameters**
REF	Reference Simulation
Tol	relative solver tolerance 10^{-4}
Sim1	WZ 5 fr = 4.5°
Sim2	WZ 5 fr = 4.75°
Sim3	WZ 5 fr = 4.0°
Sim4	WZ 5 fr = 4.85°
Sim5	WZ 5 fr = 5.15°
Sim6	WZ 5 fr = 5.25°
Sim7	no push African/Arabian plate
Sim8	African/Arabian plate inflow velocities halved
Sim9	African/Arabian plate inflow velocities quartered
Sim10	WZ 9 fr = 11.5°
Sim11	WZ 9 fr = 13.5°
Sim12	WZ 4 fr = 3.5°
Sim13	WZ 4 fr = 5.5°
Sim14	oceanic crust t_{age} = 80 Myr
Sim15	oceanic crust t_{age} = 40 Myr
Sim16	weak zone southwest of Adria
Sim17	weak zone southeast of Adria
Sim18	asthenosphere: $V_{dis} = 11.5 \times 10^{-6}\ m^3/mol$, $V_{dif} = 10.5 \times 10^{-6}\ m^3/mol$
Sim19	asthenosphere: $V_{dis} = 10.5 \times 10^{-6}\ m^3/mol$, $V_{dif} = 9.5 \times 10^{-6}\ m^3/mol$
Sim20	asthenosphere: $V_{dis} = 8 \times 10^{-6}\ m^3/mol$, $V_{dif} = 7 \times 10^{-6}\ m^3/mol$
Sim21	slabs t_{age} = 60 Myr
Sim22	slabs t_{age} = 100 Myr
Sim23	slabs t_{age} = 120 Myr
Sim24	oceanic crust southwest of Adria narrower
Sim25	oceanic crust southwest of Adria wider
Sim26	no initial continental crust southwest of Hellenic trench
Sim27	no weak mantle phase
Sim28	no Alpine-Carpathian slab
Sim29	no initial slab tearing Dinaric slab
Sim30	Adria's weak zone depth 200 km
Sim31	Adria's weak zone depth 160 km
Sim32	Adria's weak zone width 50 km
Sim33	no Alpine-Carpathian slab and no weak zone north of Adria

2.5.2.5 No Pushing of the African and Arabian Plates

In Sim7, neither the African plate nor the Arabian plate moves northward. The ApCS and the DHS exhibit almost identical dynamic behaviour as in REF, however the Adriatic microplate does not move to the north at all. At around 24 Ma, Figure 2.9a and 2.9e show that Adria undergoes an anticlockwise rotation. During this phase, plate velocities are generally low. This changes for the first time at approximately 14 Ma, when the motion of the Adriatic plate shifts to a southwest direction (Figure 2.9b and 2.9f). This takes place at the same time as the slab break-off of the WMS at the boundary with Africa. The plate velocities of the entire Adriatic microplate increase between 14 Ma and 10 Ma (Figure 2.9f and 2.9g). Between 10 Ma and present-day both the ApCS and the DHS retreat towards the south of Adria and the plate motion of Adria changes to the southeast.

2.6 Discussion

2.6.1 Comparison of Reference Model with Tectonic Reconstructions

The reference model is intended to reproduce the first-order processes observed in the Mediterranean, as inferred from geological reconstructions. There are many model parameters that affect the dynamics of the simulations, and particularly the timing of the processes is frequently very sensitive to small changes in the rheology of the mantle. Yet, we can nevertheless learn some useful lessons from the first-order features observed in the simulations. In the following section, the temporal evolution of the subduction in the western Mediterranean, the Alpine-Carpathian subduction and the Dinaric-Hellenic subduction in REF are portrayed closer and placed into context with other work. In order to facilitate a comparison of other reconstructions with REF, Figure 2.10 illustrates the trench motion of the subduction zones in REF.

In REF at 35 Ma, the western Mediterranean slab extends from Corsica to the Balearic Islands and then retreats to the south and to the west (Figure 2.10a and 2.10b). After 20 Ma, the slab breaks off at the northern African margin and the resulting slab gap propagates to the west and the east (Figure 2.10c and 2.10d). The subduction rollback of this subduction zone is in general agreement with studies such as Faccenna et al. (2014), Le Breton et al. (2021), Rosenbaum et al. (2002a) or Spakman and Wortel (2004). After the slab break-off, two different subduction systems can be identified: an eastward-dipping Gibraltar subduction zone and a westward-dipping subduction zone, which retreats towards Adria. The westward retreating Gibraltar subduction zone is supported by numerical studies (e.g., Chertova et al., 2014; Duarte et al., 2024) and by analysing tomography studies of this area (e.g., Gutscher et al., 2002; Spakman and Wortel, 2004). The eastern part of the subduction zone retreats towards Adria, exhibiting a curved trench geometry at the present-day situation (Figure 2.10f). This is a consequence of accelerated slab retreat in the south, where oceanic crust is subducted. In general, the present-day trench geometry agrees well with that of other reconstructions, such as those presented in kinematic reconstructions like Rosenbaum et al. (2002a), Faccenna et al. (2014) or the numerical models of Lo Bue et al. (2021). Rosenbaum et al. (2002a) also describe the motion of various continental blocks in the western Mediterranean. The Betic/Rif blocks exhibited a clockwise rotation as they move to the west, a phenomenon also observed in REF (Figure 2.10). In addition, Rosenbaum et al. (2002a) propose that the Kabylies blocks have moved to the south and accreted at Africa, which is also consistent with the REF model.

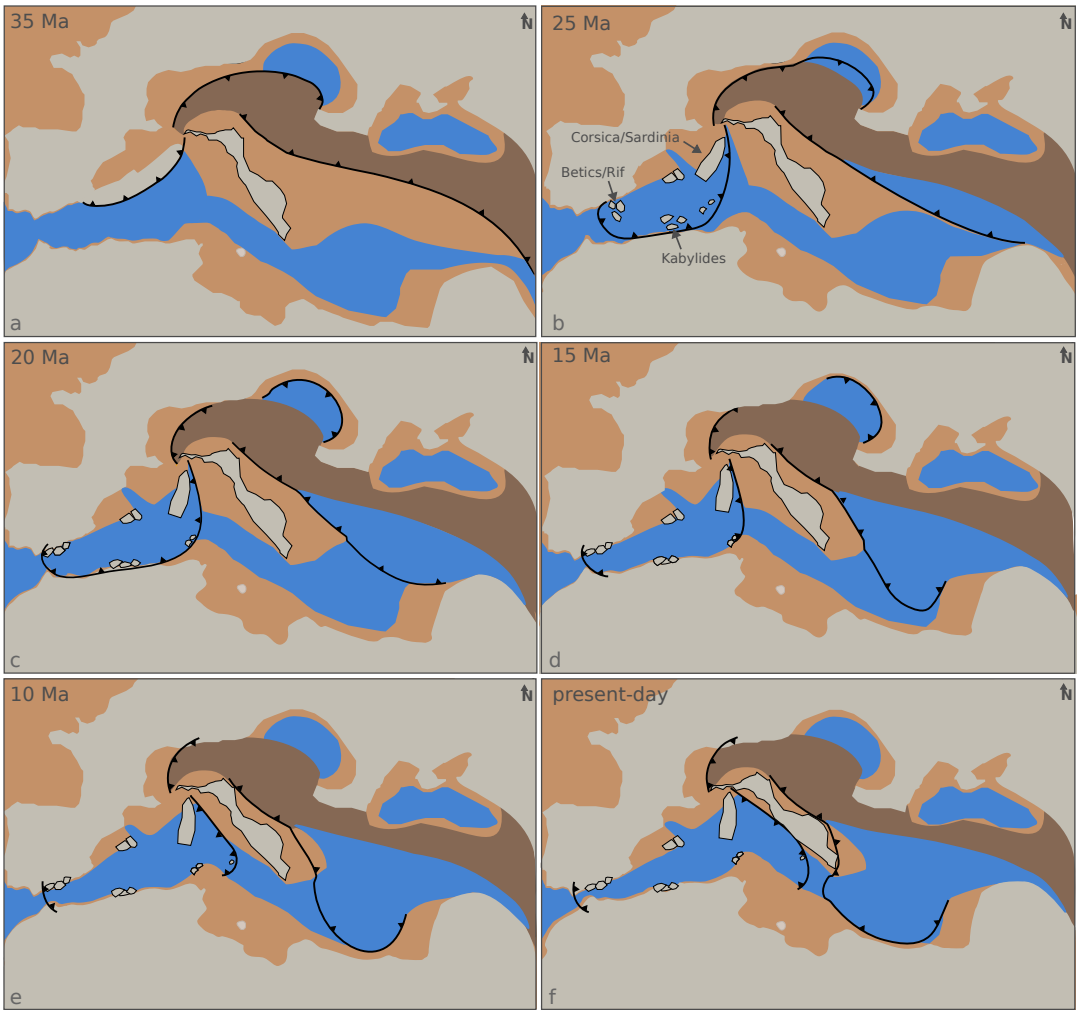

FIGURE 2.10: Trench Evolution of REF at six different timesteps. The beige colour shows continental crust, the orange colour shows continental margin, the blue colour shows oceanic crust and the brown colour shows orogenic crust. The black lines indicate the position of the trench, while the black triangles represent the direction of the slab dip.

The Dinaric and Hellenic subduction system retreated in a southwest direction (e.g., Faccenna et al., 2014; Ring et al., 2010; Menant et al., 2016), which is similar to what can be observed in REF (Figure 2.10). In the REF model, the Hellenic subduction zone subducts continental crust between 35 Ma and 25 Ma (Figure 2.10a and 2.10b), after which the retreat is accelerated while subducting old oceanic crust south of Adria (Figure 2.10c - 2.10f) (e.g., Menant et al., 2016; Pearce et al., 2012; Ring et al., 2010). The accelerated retreat of the Hellenic slab in the south leads to a curved trench geometry at present-day (Figure 2.10f). In REF, the Dinaric slab initially is much shorter than the southern Hellenic part of the slab. This is due to the slab being initially separated horizontally in the mantle, similar to what is proposed by Handy et al. (2015). This results in a more rapid retreat in the southern region when compared to the northern region.

Kinematic reconstructions of the Alpine-Carpathian subduction zone indicate that the Alpine-Carpathian slab underwent northward retreat between 35 Ma and 25 Ma, followed by a slab break-off in the center of the slab (e.g., Faccenna et al., 2014; Handy et al., 2015; Le Breton et al., 2021; Hinsbergen et al., 2020). After 20 Ma, the slab retreated faster in the Carpathian region, which led to a curved subduction

front (e.g., Faccenna et al., 2014; Handy et al., 2015). In REF, the Alpine-Carpathian subduction zone initially propagates to the north. Following a slab break-off event in the center, two distinct subduction systems retreat to the west and east, respectively. The western slab then begins to retreat to the northwest, and this process continues until it stops around 10 Ma (Figure 2.10a - 2.10e). In the east, an acceleration of slab retreat starts around 25 Ma and lasts 10 Myr. The slab break-off propagates in a circular manner to the south, where the slab is finally completely detached at 10 Ma (Figure 2.10c - 2.10e).

2.6.2 Dynamic Interactions Between Subduction Systems in the Mediterranean

A robust finding in all simulations is that mantle flow in the Mediterranean is predominantly toroidal, consistent with previous work (e.g., Kincaid and Griffiths, 2003; Li and Ribe, 2012; Schellart, 2024; Stegman et al., 2006), which show that toroidal flow is favoured by narrow rollback subduction zones. The toroidal flow in the asthenosphere is primarily driven by dynamic pressure variations (e.g., Holt et al., 2017; Pusok and Stegman, 2019). The REF model shows that the different subduction systems active within a few hundred kilometres distance from each other, as is observed in the Mediterranean, result in a highly non-uniform horizontal dynamic pressure pattern. This results in a wide variety of dynamic interactions of the subduction systems, such as trench parallel flow south of the Alpine-Carpathian slab or asthenospheric escape flow underneath Adria. The retreat of the subduction systems is primarily buoyancy-driven. When comparing the retreat of the REF model with Sim7, where there is no convergence between Eurasia and Africa/Arabia, it is evident that the motion of the African and Arabian plates only slightly affects the rollback of the subduction zones in the Mediterranean.

The escape flow under Adria to the north and to the south is caused by the retreat of the subduction systems located to the east and west of Adria. The convergence of these subduction systems results in an increase in dynamic pressure between the slabs, which in turn gives rise to an escape flow in both the north and south directions. This observed trench-parallel flow is consistent with other numerical models of two outward-dipping subduction models (e.g., Di Leo et al., 2014; Király et al., 2018b; Király et al., 2021). In the north, the escape flow is driven by the increased pressure under Adria. The toroidal flow around the northern edge of the Dinaric slab is weaker than the northward-directed escape flow (Figure 2.6f). This is consistent with the SKS splitting results of various studies that have analysed the present-day mantle flow (e.g., Salimbeni et al., 2022; Subašić et al., 2017). In the south, the escape flow has a strong toroidal component around the southern slab edge of the Calabrian slab (Figure 2.6f). This circular flow pattern around the slab edge has also been observed in other studies (e.g., Civello and Margheriti, 2004; Jolivet et al., 2009; Scarfì et al., 2023).

Kovács et al. (2012), Link and Rümpker (2023) or Petrescu et al. (2020a) propose trench parallel asthenospheric flow in the Alpine region, which in our models can be justified by the observed change in flow direction over the past 35 Myr. The flow direction has shifted from a trench-perpendicular orientation prior to 25 Ma to a trench-parallel one in the Alpine region. This phenomenon can be explained by the difference in dynamic pressure between the north of the Adria in the west and the Carpathians in the east. In the western region, the dynamic pressure is elevated between the Apenninic slab and the Dinaric slab. In contrast, in the eastern region, the dynamic pressure is low due to the rapid retreat of the Carpathian slab. This results

in the trench-parallel flow in the Alps, which supports the trench-perpendicular flow in the Carpathians. This, in turn, supports the retreat of the subduction zone in the Carpathians, which has already been proposed by Kovács et al. (2012).

The slabs in REF are a simplified representation of the actual slab structure observed by seismic studies (e.g., Rappisi et al., 2022; Paffrath et al., 2021; Spakman and Wortel, 2004). As previously stated, the existence of slab windows has been identified east and west of Adria (e.g. Rappisi et al., 2022). With the opening of a slab window, toroidal flow cells develop around the slab edges (e.g., Király et al., 2018a; Király et al., 2020). This can also be observed in Sim16, where a slab window opens to the southwest of Adria. A consequence of this is an even more complex flow pattern and a change in trench geometry. This change in trench geometry has been investigated by numerical and analogue models (e.g., Király et al., 2018a; Király et al., 2020). In the case of the Apenninic-Calabrian subduction zone, this led to the formation of the Apenninic and Calabrian arcs, which explains the difference in trench geometry between REF and the observations. In REF the trench of the Apennine-Calabrian slab is straight and elongated, while observations show a curved trench of both the Apennine and Calabrian subduction (Faccenna et al., 2004). However, many of these slab windows appear to be a recent feature such as the slab window between the Apenninic and Calabrian slab which likely happened in the last 2 Myr (e.g., Faccenna et al., 2004; Gueguen et al., 1998; Király et al., 2020; Király et al., 2021). The slab window between the Cyprus slab and the Hellenic slab reaches to about the same depth (Rappisi et al., 2022), with only the slab gap between the Hellenic and the Dinaric slabs reaching a greater depth of approximately 400 km (Rappisi et al., 2022). Given the aforementioned time constraints, it is likely that the overall dynamics of the Mediterranean has not been significantly altered by the presence of slab windows.

2.6.3 Plate Motion of Adria and Driving Forces

The plate motion of Adria over the past 35 Myr is thought to have been significantly influenced by the African plate (e.g., McKenzie, 1972). However, at some point, the direction of Adria's plate motion with respect to Africa changed (e.g., D'agostino et al., 2008). The reference model reproduces fairly well the present-day motion of the Adriatic plate described by geodetic data, which show a counterclockwise rotation of Adria relative to Europe, with a pole located to the northwest of the plate (D'agostino et al., 2008). By examining the plate motion of Adria in REF and the parameter study, we can see that this rotation and independent motion of Adria result from the interplay between the motion of the African plate and the dynamics of the surrounding subduction zones.

It can be observed that while Africa is constantly pushing, Adria begins to rotate with respect to Africa at a certain stage. This proceeds while the Calabrian subduction in the southwest of Adria and the Hellenic subduction in the southeast retreat towards Adria. In order to further understand this, the difference in direction between the southern part of Adria and Africa is plotted against the shortest horizontal distance between the Calabrian trench and Hellenic trench (Figure 2.11). This allows to compare different simulations and make them independent of time, but dependent on the subduction dynamics around Adria. The rotation of the Adriatic microplate with respect to Africa is initiated only when the trenches undercut a threshold of approximately 1000 km $\pm$ 100 km (Figure 2.11a). Prior to reaching this stage, Adria and Africa move in the same direction. Subsequently, the angle difference between Adria and Africa increases linearly as the trench distance decreases (Figure 2.11a). This can be explained by an interplay of various factors. The northern part of Adria

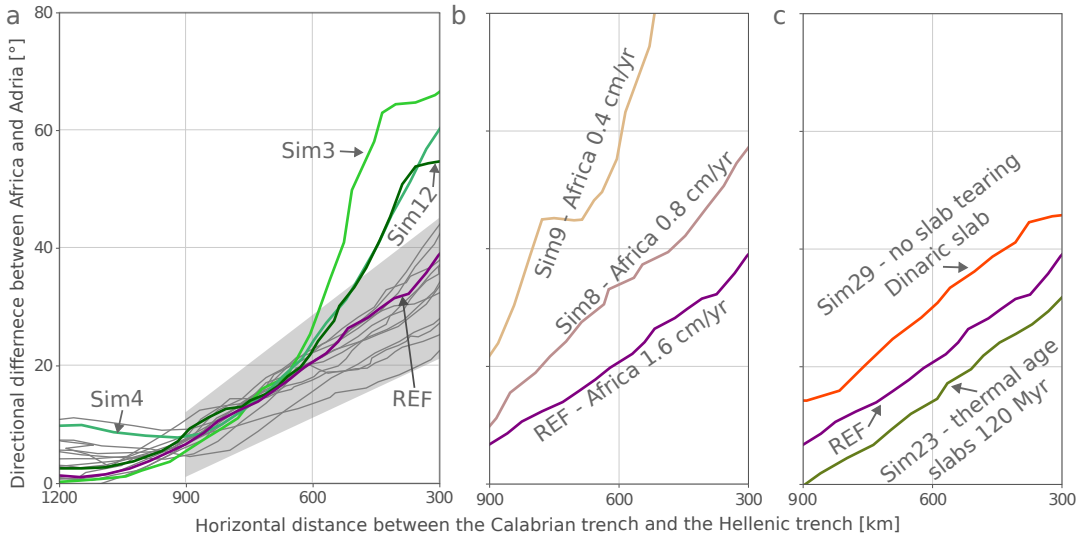

FIGURE 2.11: Comparison of different simulations. The direction of "Adria south" minus the direction of "Africa" (Figure 2.8a for exact locations) is plotted against the horizontal distance of the Calabrian trench and the Hellenic trench. (a) simulations with similar behaviour are coloured in grey, these are Sim1, 2, 6, 10, 11, 13, 14, 21, 22, 25, 27, 28. The plot also shows the REF simulation and Sim3, 4, 12 in colour. (b) shows a comparison of REF with Sim9 and Sim8. (c) shows a comparison of REF with Sim23 and Sim29.

already starts to slow down prior to the rotation of the southern part (Figure 2.8b). This can be attributed to the slowing down of the Alpine subduction zone to the north of Adria. During this period, the African plate is moving northwards at a distinctly faster rate than the northern part of the Adriatic plate. As the Apenninic-Calabrian and Hellenic-Dinaric subduction zones retreat towards Adria, the connection between Adria and Africa is becoming increasingly narrow. This results in Africa only pushing the southeastern part of Adria, where the northwestern part of Adria remains fixed (Figure 2.7b - 2.7d). This geometric constellation forces Adria to rotate anticlockwise, in order to compensate for the northward movement of Africa. The slab pull generated by the surrounding slabs alone is insufficient to pull Adria to the northeast. This can be seen in Sim7 in which Africa is not pushing. In this case, the only factors that determine the plate motion of Adria are the surrounding subduction zones. If these subduction zones are within a few hundred kilometres distance from Adria, Adria's motion will be directed towards the southeast, rather than to the northeast (Figure 2.9h).

However, the plate motion of Adria can still be partly influenced by the surrounding subduction zones. In specific cases, the linear trend in angle change of Adria may be interrupted, resulting in a sudden increase in the rate of change of the angle as can be observed in Sim3, Sim4, and Sim12 (Figure 2.11a). In these simulations, the friction angle of weak zone 4 and 5 is changed. That results in the occurrence of a slab break-off event of the Hellenic slab at the African margin. After this slab breaks-off, the slab pull forces of the Hellenic slab rearrange, which in turn results in an increased plate pull towards the Adriatic microplate. Consequently, the Hellenic slab has a more pronounced influence on the plate motion of the Adriatic microplate. Furthermore, the rate of change of Adria's motion direction is also affected by the velocity of Africa. The slower the motion of Africa, the faster the rotation of Adria with respect to Africa (see Sim8 and Sim9, where the inflow velocities of Africa are

halved and quartered, respectively, Figure 2.11b). If Africa is slower, the slab break-off of the WMS at Africa happens later than in REF. This results in a slower retreat of the Calabrian slab. In that case, the Hellenic slab is always closer to Adria than the Calabrian slab, so that it has a stronger influence on the motion of the Adria and pulls it eastwards.

Another trend can be observed when looking at Figure 2.11c. Sim29 presents a simulation in which the initial slab tearing in the Dinaric slab is absent, resulting in a significantly larger slab volume. This strengthens the slab pull to the northeast and therefore increases the difference between Adria and Africa, allowing for the independent movement to start earlier. In Sim23 the thermal age of the slabs is increased to 120 Mry, which means that the slabs are cooler and denser than in REF. This accelerates the retreat of the slabs. Nevertheless, the retreat of the Apenninic-Calabrian slab is accelerated to a greater extent than that of the Dinaric-Hellenic slab, which in turn increases the slab pull force to the west of Adria and therefore it decreases the difference from Africa compared to REF.

A comparison of the REF simulation with kinematic reconstructions (see Appendix 2.C) reveals a lower absolute northward motion of Adria (e.g., Le Breton et al., 2017; Hinsbergen et al., 2020). Le Breton et al. (2017) propose that during the rotation of Adria, there was still a northward translation of more than 100 km in the last 20 Ma. However in REF, Adria's motion towards the north ceases almost entirely during the rotational phase after 13 Ma, when the subduction stops retreating in the Alps. This also shows the important influence of the Alpine subduction zone on the northward motion of Adria. We note that a subduction of Adriatic lithosphere beneath Europe (e.g. in Sim31) to the north of Adria would pull Adria further to the north. In our simulations, such a subduction is only initiated when the weak zone to the north of Adria reaches a depth of at least 160 km and if the retreat of the Alpine slab has already ceased (Sim31) or if the Alpine slab is not retreating at all (Sim28). All these scenarios are however not consistent with geological reconstructions of plate convergence and recent interpretation of seismic tomography in the Alps (e.g., Handy et al., 2010; Handy et al., 2021).

2.6.4 Limitations of our Modeling Approach

The dimensions of the model are finite, unlike nature. The large-scale flow pattern can be influenced by the dimensions of the model and the prescribed outflow at all boundaries of the box. Furthermore, in our models, the lower boundary, at a depth of 660 km, is closed and there are no interactions with a potential lower mantle. However, this could also influence the dynamics by introducing poloidal flow cells that act across the lower and upper mantle (e.g., Schellart, 2024). Especially in the case of the Hellenic subduction system, the lower mantle may exert an influence on subduction dynamics, given that in REF at 35 Ma the Hellenic slab already reaches down to the 660 discontinuity.

Our model also lacks a westward-moving Anatolian plate, which is likely to change the plate motion of the plate southeast of Adria (e.g., Glerum et al., 2021; Serpelloni et al., 2022). This motion can also contribute to the observed plate motion south of Adria, which in this case is not only related to Africa but also to the Anatolian plate. Nevertheless, it should not significantly affect the dynamics of the model, as this overriding plate is not the primary driving force behind the Hellenic subduction; rather, it is the buoyancy forces of the slab itself. Another limitation is the eastern vertical boundary of the model domain. In our models, the Hellenic slab quickly detaches from the eastern boundary to rapidly rollback westward. The retreat is

enhanced by the slab pull of the detached slab. In reality, the slab remained attached to the east, reducing the slab pull force that facilitates its westward retreat in our models.

It is generally assumed that the convergence between Africa and Europe was active over the last 35 Myr, while the magnitude of this process may have changed over time. In their study Jolivet and Faccenna (2000) propose an increase in the convergence rate between Africa and Eurasia at 30 Ma, followed by a decrease after 20 Ma. Reilinger and McClusky (2011), on the other hand, propose two periods during which the convergence rate slowed down, one occurring approximately after 25 Ma and the other at 11 Ma. In order to account for the convergence of Africa and Eurasia in our simulations, a simplified process was applied by using a constant pushing velocity of Africa over time.

2.7 Conclusions

The present study employed 3D numerical modelling to investigate the subduction dynamics around the Adriatic microplate in the Alpine-Mediterranean region. We were able to reproduce the first-order trench retreats of the major subduction zones in the Alpine-Mediterranean, as well as the motion and rotation of the plates and continental blocks involved. The modelling results highlight the complex interactions between these subduction zones and their influence on mantle dynamics and the kinematics of the Adriatic microplate. It was possible to extensively explore a large parameter space by running more than 500 3D thermomechanical simulations.

The subduction zones around Adria, the Alpine-Carpathian subduction to the north, the Apennines-Calabrian subduction to the west and the Dinaric-Hellenic subduction to the east, exert a strong influence on the mantle flow. The principal findings with regard to mantle flow are as follows:

1. Toroidal flow is the dominant mode of mantle dynamics in the Mediterranean.

2. The retreat of the Dinaric-Hellenic subduction and the Apenninic-Calabrian subduction results in the formation of an escape flow under Adria to the north and to the south.

3. After 20 Ma, a trench parallel flow is observed south of the Alpine slab, driven by the dynamic pressure difference between the high dynamic pressure under Adria and the low dynamic pressure south of the fast retreating Carpathian slab.

4. The two toroidal flow cells, one situated around the southern Calabrian slab edge and the other around the southern Hellenic slab edge, induce a strong southward-directed flow under southern Adria.

Furthermore, the influence of surrounding subduction zones and the convergence between Africa and Eurasia on plate motion of Adria was investigated. It was demonstrated that the northern part of Adria is primarily influenced by the interaction between the African plate motion and the subduction system in the Alps. Once the Alpine slab has ceased its northward retreat, the motion of Adria towards the north also ceases despite the continued northward movement of Africa.

An examination of the entire Adriatic microplate reveals that it begins to rotate with respect to Africa at a specific point. This rotation can be attributed to a number of factors. Firstly, the northern part of the Adriatic plate decelerates as a result of the

ceasing of the Alpine slab. Conversely, Africa continues to move northwards, while the Calabrian subduction to the west and the Hellenic subduction to the east are approaching Adria, effectively narrowing the connection between Adria and the African continent. As the distance between the two trenches narrows (at about less than 1000 km), the influence of Africa's push reduces to the southeastern portion of Adria. Since Adria is fixed in the northeast at this point, this results in a counterclockwise rotation of the microplate. The slab pull of the subduction zones surrounding Adria alone appears to not be sufficient to be the primary driver of Adria's plate rotation. Nevertheless, the closer the trenches are to the Adriatic microplate, the more profound the influence of the surrounding subduction zones on Adria's motion becomes. Abrupt changes in subduction dynamics, such as slab break-offs, can significantly increase the impact of the subduction zone on Adria's plate motion.

In conclusion, in a system where there has been a continuous convergence between Africa and Eurasia, the plate motion of Adria is primarily influenced by the interplay of three factors: 1) the convergence between the African and Eurasian plates, 2) the retreat of the Alpine subduction zone to the north, and 3) the distance between the retreating Calabrian and Hellenic subduction zones around Adria.

2.8 Appendix

2.A Heterogeneities in the Lithosphere

The heterogeneities in the mantle lithosphere are created by the insertion of horizontal ellipses, with horizontal minor axes measuring 100 km in length and vertical minor axes measuring 20 km in length. In order to place them the model is subdivided into horizontal control areas of 100 km edge length each. In each of these control areas the x and y center points are randomly positioned within a 10 km inner square. The depth z is randomly assigned a value between 48 km and 78 km.

2.B Temperature and Viscosity Structure

In Figure 2.12, we show the temperature and effective viscosity structure of a representative cross-section through the REF simulation at 10 Ma.

2.C Quantitative Measurements for Model Validation

Here, we present quantitative measurements used to identify the best-fitting model (REF) compared to published tectonic reconstructions of the area.

First, we show a comparison of the total northward motion and total counterclockwise rotation of the Adriatic microplate over the last 35 Myr in plate kinematic reconstructions of Le Breton et al. (2021) (Figure 2.13a) with the model REF (Figure 2.13b). The counterclockwise rotation of Adria of about 9° is well reproduced by the model. However, the northward movement of Adria is lower in the REF model (170 km) compared to the kinematic reconstructions (280 km). This is discussed in the article (section 6.3). Moreover, the counterclockwise rotation of the Corsica-Sardinia block is well reproduced in the model, with a slightly lower amount of rotation of about 40° (A1 in Figure 2.13c), compared to about 53° in kinematic reconstructions of Le Breton et al. (2021).

We also compared the distance of horizontal trench retreat in the model and in tectonic reconstructions of Hinsbergen et al. (2020) and Le Breton et al. (2021). This is shown in Figure 2.13c. The trench retreat of

1. the Gibraltar subduction zone (D1) is about 530 km in our REF model and about 600 km in the reconstructions.

2. the Calabrian subduction zone (D2) is about 1060 km in the model and about 1000 km in the reconstructions.

3. the Carpathians subduction zone (D3) is about 360 km in the model and ranges between 300 - 500 km depending on the reconstructions (van Hinsbergen et al. 2020 and Le Breton et al. 2021, respectively).

4. the Hellenic-Aegean subduction zone (D4) is about 1000 km in both the model and the reconstructions.

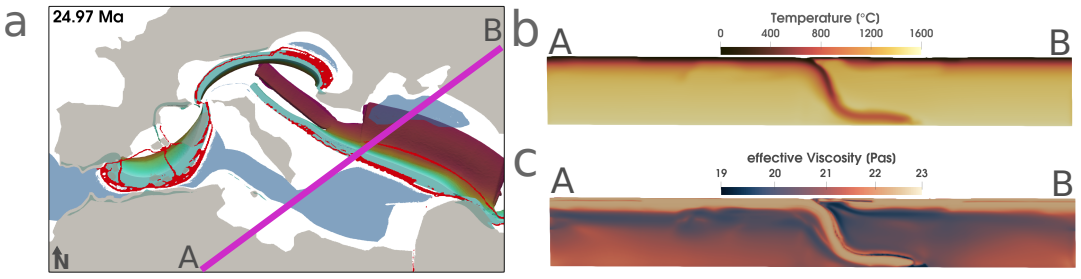

FIGURE 2.12: Cross-sections through the REF model. (a) mapview of REF simulation at 10 Ma (see Figure 2.3 b. The purple line indicates the location of the cross-section. (b) temperature cross-section. (c) Effective viscosity cross-section)

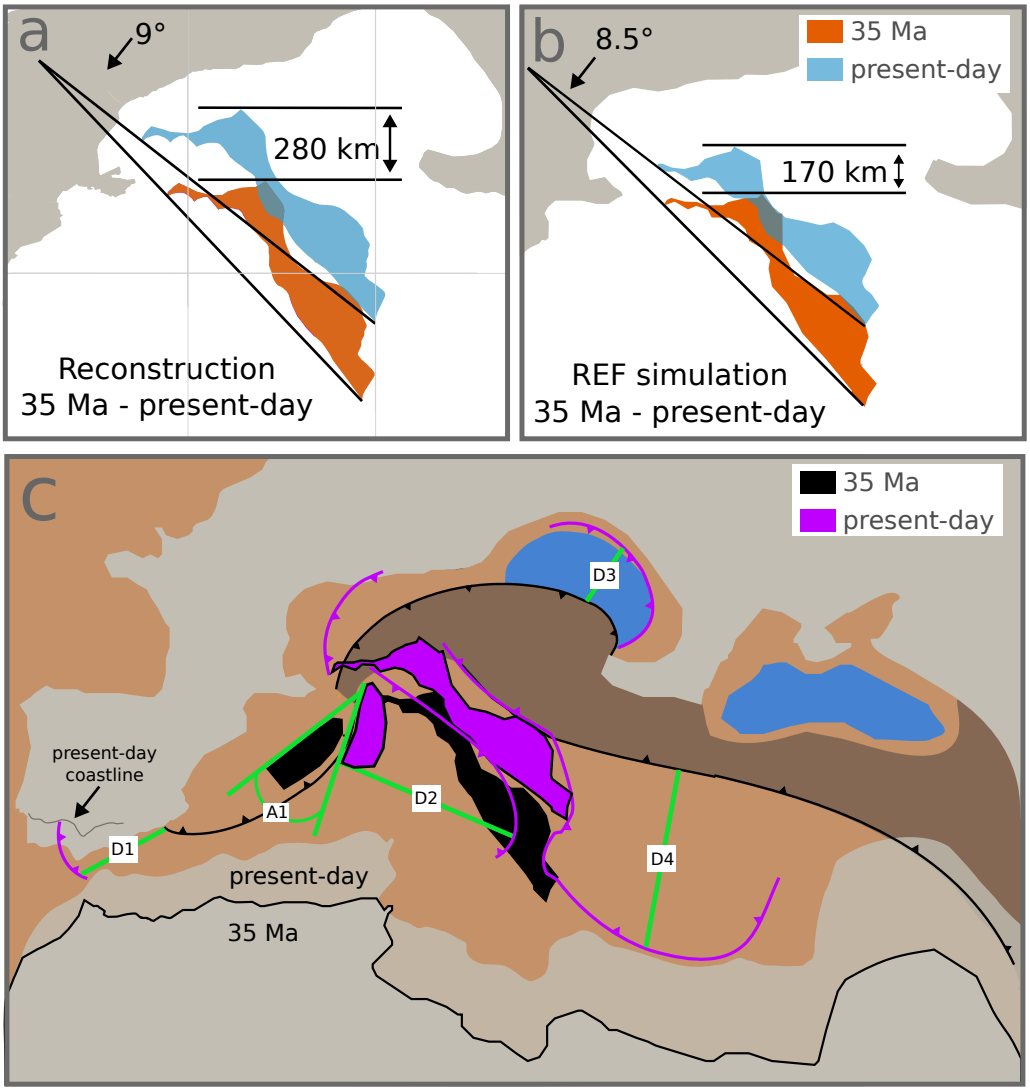

FIGURE 2.13: Quantitative measurements to compare the thermomechanical simulations (in this case the REF simulation) with tectonic reconstructions: (a) northwards motion and rotation of Adria between 35 Ma and present-day according to Le Breton et al. (2021); (b) northwards motion and rotation of Adria between 35 Ma and present-day in REF simulation; (c) Mapview of REF simulation. Black lines are the trench location in REF at 35 Ma and purple lines the trench position in REF at present-day. Adria and Corsica-Sardinia are displayed both at 35 Ma (black) and present-day (purple). The green lines show different distances that were measured to compare the simulations with tec- tonic reconstructions. D1 – trench retreat of Gibraltar subduction, D2 – trench retreat of Calabrian subduction, D3 – trench retreat of Carpathians subduction, D4 – trench retreat of Hellenic subduction. A1 shows the angle of rotation of the Corsica – Sardinia block between 35 Ma and present-day.

2.D Data Availability Statement

The software to run the simulations is available on zenodo via Schuler et al. (2024). This repository contains the version of LaMEM (Kaus et al., 2016) and the geomIO package (Bauville and Baumann, 2019) that were used in the reference simulation, along with the input scripts that were used to run the simulation.

2.E Acknowledgements

We thank Claudio Faccenna for helpful discussions on Mediterranean tectonics and Andrea Piccolo who helped with the visualization. This paper greatly benefited from the constructive reviews of Manuele Faccenda and an anonymous reviewer. Paraview was used for the visualization of the modelling results (https://www.paraview.org/). The authors gratefully acknowledge the computing time granted on the supercomputer MOGON 2 at Johannes Gutenberg University Mainz (hpc.uni-mainz.de). CS acknowledges financial support provided by the German Research Foundation (DFG), SPP project Mountain Building in 4-Dimensions (4D-MB) through grant KA3367/10-1. ELB acknowledges financial support from the German Research Foundation (DFG) through grant BR 4900/4-1.

Chapter 3

Shear Wave Splitting in the Mediterranean and Alpine Region: Models vs. Observations

3.1 Abstract

Shear-wave splitting is an observational technique that can provide information about the deformation history in the mantle and crust. This makes it a powerful tool for comparison with thermomechanical forward simulations. In this study, synthetic shear-wave splitting parameters, specifically the orientation of the fast polarization direction (FPD) and the delay time (dt), are computed from a thermomechanical simulation that models the subduction dynamics of the central Mediterranean over the past 35 Myr. The synthetic observables are then compared with seismically observed shear-wave splitting parameters. A comparison of observations and model results in the Alpine region reveals common features, such as trench-parallel FPD south of the Alps, a flow around the Alpine mountain belt in the north and northwest-southeast oriented FPD east of the Alps. The results also indicate that the model does not perfectly reproduce the observations, as discrepancies are observed in certain regions, such as the Liguro–Provençal Basin: the model predicts a gradual transition from northwest–southeast oriented FPD in the basin to a circular pattern around the Alps, whereas observations reveal an abrupt change at depth. This contrast suggests that deeper mantle processes or a potential slab gap in the Apennines cause the observed pattern. The comparison between model results and observations thus helps to verify the conclusions drawn from the observations, and conversely, the observational data can be used to improve the numerical model.

3.2 Introduction

The phenomenon by which the propagation velocity of a seismic wave changes with its polarization and propagation direction is called seismic anisotropy. This occurs in a variety of settings, including the Earth's upper mantle and crust and offers valuable insights for the geological interpretation of different regions (e.g., Silver, 1996; Silver and Chan, 1988; Long and Becker, 2010; Plomerová and Babuška, 2010; Reiss et al., 2019; Link and Rümpker, 2021). Seismic anisotropy can be attributed to different processes, where generally two main types of anisotropy are differentiated: shape-preferred orientation (SPO) and crystallographic or lattice-preferred orientation (CPO/LPO). In the following, the latter is referred to as CPO. Shape-preferred orientation is a result of the alignment of materials with different isotropic elastic properties, which overall results in an anisotropic medium (e.g., Long and Becker, 2010). This can be caused

by the layering of sediments, the intrusion of magmatic dykes in the crust or the orientation of melt pockets (e.g., Stein and Wysession, 2009). Crystallographic-preferred orientation describes a configuration in which the crystallographic axes of seismically anisotropic minerals are non-randomly oriented (e.g., Tommasi et al., 2000; Jung et al., 2006). It originates through various processes, including dislocation glide and recrystallization (e.g., Karato et al., 2008). Olivine CPO plays a key role in the upper mantle and is therefore assumed to be the most significant mechanism to generate anisotropy in this region (e.g., Ribe, 1989; Boneh and Skemer, 2014; Skemer and Hansen, 2016).

Seismic anisotropy in the upper mantle is primarily studied through shear-wave splitting or surface-wave analysis (e.g. Long and Becker, 2010). This chapter focuses on shear-wave splitting observations of the upper mantle (e.g., Silver and Chan, 1991; Long and Hilst, 2005; Long and Silver, 2008; Link and Rümpker, 2023).

If a shear wave travels through an anisotropic region, it splits into two shear waves, where both shear waves are polarized orthogonal to each other (e.g., Maupin et al., 2007; Long and Becker, 2010). The two phases also travel at different velocities. The shear wave, which is polarized parallel to the fast direction of the anisotropic medium, is propagating faster. This results in two characteristic parameters: the delay time dt, that accumulates between the two waves and the fast polarization direction (FPD), which is typically expressed relative to the north direction. In order to analyze this phenomenon, the polarization of the shear wave before it enters the anisotropic medium should be known. A commonly used approach is to analyze XKS waves, which are S-waves that are converted from P-waves at the outer core and are polarized linearly when entering the mantle (Stein and Wysession, 2009, Long and Becker, 2010). Another advantage is that they travel almost vertically through the upper mantle, so that they contain information about the anisotropy of a vertical column through the Earth's upper mantle and crust (Long and Becker, 2010).

The interpretation of shear-wave splitting observations is not always straightforward and often non-unique (Long and Becker, 2010, Becker and Lebedev, 2021). To address this limitation, it can be useful to incorporate geodynamic modeling into the interpretation of seismic anisotropy. Faccenda and Capitanio (2012), Faccenda and Capitanio (2013) and Kruse et al. (2024) calculated synthetic SKS splitting parameters from geodynamic subduction models to improve the interpretation of anisotropy measurements around subduction zones. Becker et al. (2006) linked global mantle convection models with seismic anisotropy. Several studies have employed regional geodynamic models to investigate anisotropic patterns in the mantle. Confal et al. (2018) focused on the eastern Mediterranean, Lo Bue et al. (2021) and Lo Bue et al. (2022) on the central and western Mediterranean and Alpert et al. (2013) on the Alboran region in the western Mediterranean.

In this chapter, we address seismic anisotropy in the upper mantle and discuss how direct measurements of anisotropy can improve numerical models through their direct link to deformation history and, conversely, how numerical models can improve the interpretation of anisotropy measurements. To this end, we evaluate the CPO for the thermomechanical model of the Mediterranean presented in the previous chapter, calculate synthetic XKS splitting parameters and compare the results with existing shear wave splitting studies of the Mediterranean, with particular focus on the Alpine region in comparison to Link and Rümpker (2023).

3.3 Methods

3.3.1 Thermomechanical Simulation

In this chapter, we calculate the CPO of polycrystalline upper mantle aggregates based on the results of the thermomechanical model from the previous chapter, analogous to Kruse et al. (2024). We use a modified version of the REF model (Schuler et al., 2025), termed REF2. This modification is motivated by two reasons. First, the software ODREX (Kruse et al., 2024) used here requires uniform grid spacing, which is adopted for REF2. Second, because this study focuses on the Alpine region, the northern boundary was extended by 500 km to the north in order to reduce its influence on the area. The new REF2 model is used throughout this chapter. Its dynamics are similar to those of the REF model, with a detailed comparison provided in Appendix 3.A.

3.3.2 Determining the CPO in the Upper Mantle: ODREX

The textural evolution of polycrystalline aggregates was simulated using the ODREX software (Kruse et al., 2024). The resulting elastic tensors serve as a measure of CPO in the mantle. ODREX is a modification of the original code D-REX (Kaminski et al., 2004) that improves numerical efficiency and can therefore be used for large-scale 3D models that are analyzed in this chapter. For details about the choice of model parameters, the reader is referred to Kruse et al. (2024).

Apart from that, the velocity gradient tensor of the thermomechanical simulation and its temporal evolution are required. Therefore the softare lamem2drex is used (Kruse et al., 2024). With this software, the velocity gradient tensor is calculated backward in time. To capture the temporal evolution, this is done every 0.1 Myr, starting from the simulation results at present-day and tracing back to 24 Ma, thereby covering 24 Myr. For more information about lamem2drexinput, details are provided in Kruse et al. (2024).

Our interest lies in the CPO evolution of the sublithospheric mantle. At the start of the simulation, 80 km of mantle material beneath the crust is defined as lithospheric mantle, which is assumed to be isotropic in these calculations. Additionally, the CPO is set to zero, when an aggregate is entering the transition-zone below 410 km depth in order to account for phase changes. This is in agreement with other studies like e.g. Faccenda and Capitanio (2013), Lo Bue et al. (2021) and Kruse et al. (2024).

The strength of anisotropy can be determined based on the elastic tensor. This is achieved in a manner consistent with the approach outlined in Kruse et al. (2024) by solving the Kelvin-Christoffel equation. This results in the polarization directions as well as the phase velocities of three body waves for a specific propagation direction. In the case of anisotropy, two different phase velocities are obtained for the two shear waves. This can be used to establish a measure of the strength of anisotropy (Mainprice and Silver, 1993). The strength of anisotropy is therefore expressed as a percentage and denoted by ξ.

$$\xi = 100 \frac{(\mu_\mathrm{f} - \mu_\mathrm{s})}{0.5\,(\mu_\mathrm{f} + \mu_\mathrm{s})}\,, \tag{3.1}$$

where μ_f and μ_s are the slowness of the fast and slow S-wave, respectively.

In the following, we use the anisotropy strength ξ together with the polarization direction of the fast shear wave, denoted as p, to characterize the anisotropy of the model.

3.3.3 Synthetic XKS Splitting

To evaluate the synthetic splitting parameters, synthetic waveforms are simulated that travel through a stack of layers and the splitting parameters of these waveforms are calculated based on the solution of the Kelvin-Christoffel equation. To do so, we need the elastic tensor for each layer, which comes from ODREX. Based on the waveforms that would be recorded at a virtual receiver at the surface, we compute the splitting intensity (Chevrot, 2000; Monteiller and Chevrot, 2010). This is done for waveforms with different initial polarizations, yielding different splitting intensities. These different splitting intensities are then fitted to achieve one-layer splitting parameters. For a detailed description, the reader is referred to Kruse et al. (2024).

3.3.4 Characterization of Mantle Anisotropy

To characterize the anisotropy pattern in the mantle, we introduce the quality factor α, which is based on the gradient of p with respect to depth and on the maximum and minimum values of ξ within each depth column. The α value for each depth column is calculated as follows:

$$\alpha = \frac{\xi_{\max} - \xi_{\min}}{\xi_{\mathrm{ch}}} + \frac{\left(\frac{\partial p}{\partial z}\right)_{\max}}{p_{\mathrm{ch}}} \quad , \tag{3.2}$$

where $\xi_{\max} - \xi_{\min}$ is the difference between the maximum and minimum values of ξ within each depth column and $\left(\frac{\partial p}{\partial z}\right)_{\max}$ is the maximum gradient of p with respect to z within each depth column. ξ_{ch} and p_{ch} are characteristic values of ξ and p that can be chosen to represent a significant change in anisotropic properties.

In addition, we aim to identify regions strongly influenced by fast-axis orientations of the crystals that are primarily vertical rather than horizontal. Therefore, we introduce the accumulated (viscous) strain, defined as the integral of the largest absolute eigenvalue of the strain-rate tensor over the particle path (see Kruse et al., 2024 for details). We use the full strain-rate tensor, which serves as an approximation of the viscous strain rate, as mantle deformation over large timescales occurs predominantly in the viscous regime (Bessat et al., 2020). The accumulated strain, averaged over each depth column, is denoted as γ. The values of γ calculated for the reference model over a period of 24 Myr are provided in Appendix 3.B. Regions showing high γ but low delay time dt likely indicate a strong influence of rather vertical oriented fast axis orientations of the crystals (Kruse et al., 2024). To capture this, we introduce the quality factor β, which highlights regions with a large γ relative to dt:

$$\beta = \frac{\gamma}{\gamma_{\max}} \cdot \left| \frac{dt}{dt_{\max}} - 1 \right|, \tag{3.3}$$

where $\gamma_{\max}$ is the maximum value of γ and $dt_{\max}$ the maximum value of the delay time dt.

3.4 Results

The present study focuses on the central Mediterranean region, encompassing the Alpine-Carpathian region to the north of the Adriatic microplate, the Apennines-Calabrian subduction zone (ApCS) to the west of Adria, and the Dinaric-Hellenic subduction system (DHS) to the southeast of Adria. The Alpine subduction to the north of Adria is abbreviated with AS. Figure 3.2a shows the location of these three

subduction zones. The results of the thermomechanical simulation REF2 are analyzed within a rectangular area around Adria, extending 4000 km in the x-direction (east–west) and 3500 km in the y-direction (north–south). The exact location of this area in the reference model REF2 is shown in Figure 3.2a. The results are presented in three steps. First, the depth-dependent anisotropy factor ξ and the fast polarization direction p are shown for three depth slices: 150 km, 250 km, and 350 km (Figure 3.1). Next, the delay time dt and the FPD, calculated from the synthetic SKS splitting intensity results for this area, are presented (Figure 3.2b). Finally, the depth profiles of ξ and p at four locations are analyzed (Figure 3.3). These locations were found using the quality factors α and β.

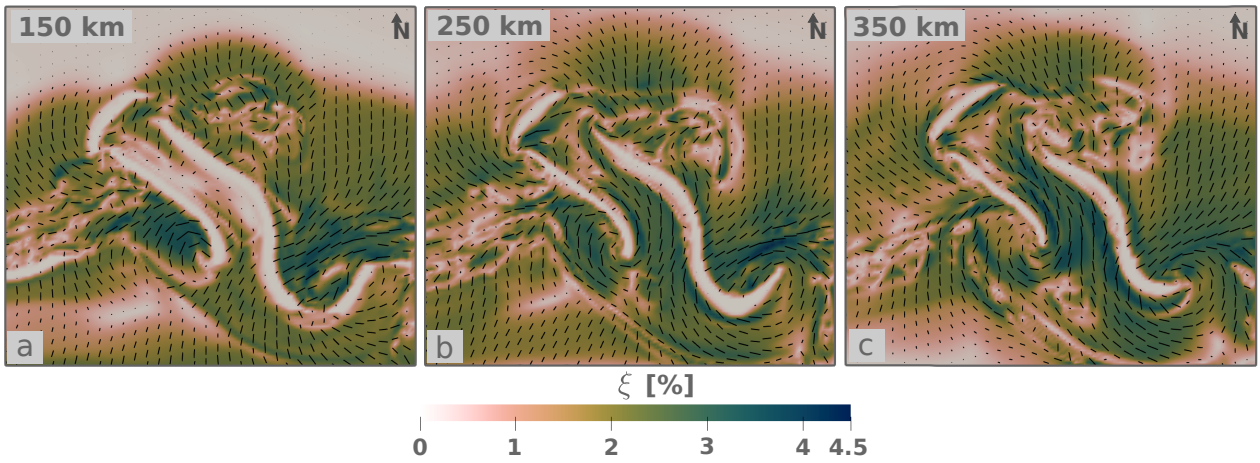

FIGURE 3.1: Depth-dependent seismic anisotropy properties of the forward model. The color indicates the strength of anisotropy ξ, while the bars represent the fast polarization direction p. Three depths are shown: (a) 150 km, (b) 250 km and (c) 350 km.

3.4.1 Seismic Anisotropy Properties

Figure 3.1 shows the strength of anisotropy, represented by ξ, together with the direction of the fast polarization axis. These quantities are shown for three depths: 150 km, 250 km and 350 km. In general, the slabs appear completely isotropic, since only the CPO evolution of the asthenosphere is considered. As a result, AS in the north, the ApCS west of Adria and the DHS east of Adria can be identified. At a depth of 150 km, the strongest anisotropy occurs west of the southern ApCS and east of the southern DHS, where p is oriented perpendicular to the trench. The ξ value has its maximum in these regions with about 4.5%. Beneath Adria, the anisotropy is weak with ξ close to zero, whereas south of the Alpine slab, intermediate anisotropy appears, oriented slightly trench-parallel. North of the Alpine slab, a circular anisotropy pattern around the slab is observed. In the western Mediterranean, anisotropy shows no clear orientation and ξ remains generally small. In the southern Carpathians region, the anisotropy exhibits a complex pattern, while in the north p is oriented in a northwest-southeast direction.

Figure 3.1b shows the results at a depth of 250 km. A crucial difference compared to 150 km can be observed beneath Adria, where a strong ξ signature develops. In this case, p aligns parallel to the trenches of the ApCS and DHS, also producing a pronounced circular anisotropy pattern around the southern slab edge of the ApCS. A similar pattern is observed at the southern slab edge of the DHS, where the strongest anisotropy occurs, with ξ values of about 4.5%. South of the AS, a clear trench-parallel anisotropy develops, while the circular anisotropy pattern north of the slab becomes

more pronounced compared to 150 km depth. The complex anisotropy pattern of the Carpathians shifts slightly southward and a strong north–south-oriented anisotropy pattern emerges to its north. At a depth of 350 km the anisotropy pattern looks quite similar to a depth of 250 km. The circular pattern around the southern part of the ApCS weakens, as does the circular anisotropy around the southern DHS, compared to 250 km depth. In contrast, the trench-parallel anisotropy beneath Adria strengthens. South of the Alpine slab, the polarization direction remains parallel to the Alpine trench, and high ξ values are observed between the AS and the ApCS. The anisotropy in the Carpathians region is overall slightly weaker than at 250 km depth.

In general, at shallower depths, the strongest anisotropy occurs in circular patterns around the southern edges of the ApCS and DHS. At greater depths, ξ is still high, but the strongest ξ values are found beneath Adria, where the p is oriented trench-parallel with respect to the surrounding slabs. In the Alpine region, at depths of 250 kmand 350 km, strong anisotropy is observed parallel to the Alpine trench. This orientation is nearly orthogonal to the anisotropy observed beneath Adria.

3.4.2 Shear wave splitting results

In this section, the shear-wave splitting results for the observation area are illustrated. The results are presented in Figure 3.2b. Overall, the highest delay times dt of about 2.5s are observed southwest of the ApCS and northeast of the southern DHS. In both areas, the FPD exhibits a clear trench-perpendicular orientation. Around the slab edges, dt decreases and the FPD forms a circular pattern. Beneath Adria, a quasi–trench-parallel FPD is observed, with delay times reaching up to about 1.5s. To the southwest of the ApCS, the anisotropy is mostly dominated by the aforementioned perpendicular-aligned anisotropy. However, further north in the Apennines region, the FPD is oriented sub-parallel to the trench while delay times decrease to around 1s. This orientation merges into a broader circular pattern around the AS in the north. To the south of the AS, the FPD is strictly parallel to the AS. This contrasts with the trench-parallel FPD beneath Adria, producing a near 90° difference between the two regions. In the transition zone between these regions, the FPD rotates westward in the west and eastward in the east. Note that a clear anisotropic signal is observed between the AS and the ApCS, oriented trench-parallel to the AS. To the east of the AS, a large-scale, north-south-oriented FPD with delay times of around 1.5s can be identified. Further to the south, the anisotropy offers a more complex picture. In this area, the delay times are relatively small. Around the northern part of the DHS, the FPD forms a circular pattern around the slab edge. While the delay times are generally small in this region, they increase towards the south in the region of the Hellenides. There, the trench of the DHS is circular and the FPD aligns perpendicular to it.

In summary, the most prominent features are the strong anisotropy and trench-perpendicular FPD northwest of the Calabrian slab (southern part of ApCS) and northeast of the Hellenic slab (southern part of the DHS). In contrast, the FPD beneath Adria is trench-parallel. North of Adria, the FPD undergoes a sharp transition, becoming trench-parallel with respect to the Alpine slab.

3.4.3 Depth profiles of ξ and p

In this section, depth profiles of ξ and p at four locations within the observation area are presented. The locations are indicated in Figure 3.3a and b. Figure 3.3a shows the quality factor α, where high α values hint at a depth profile with pronounced

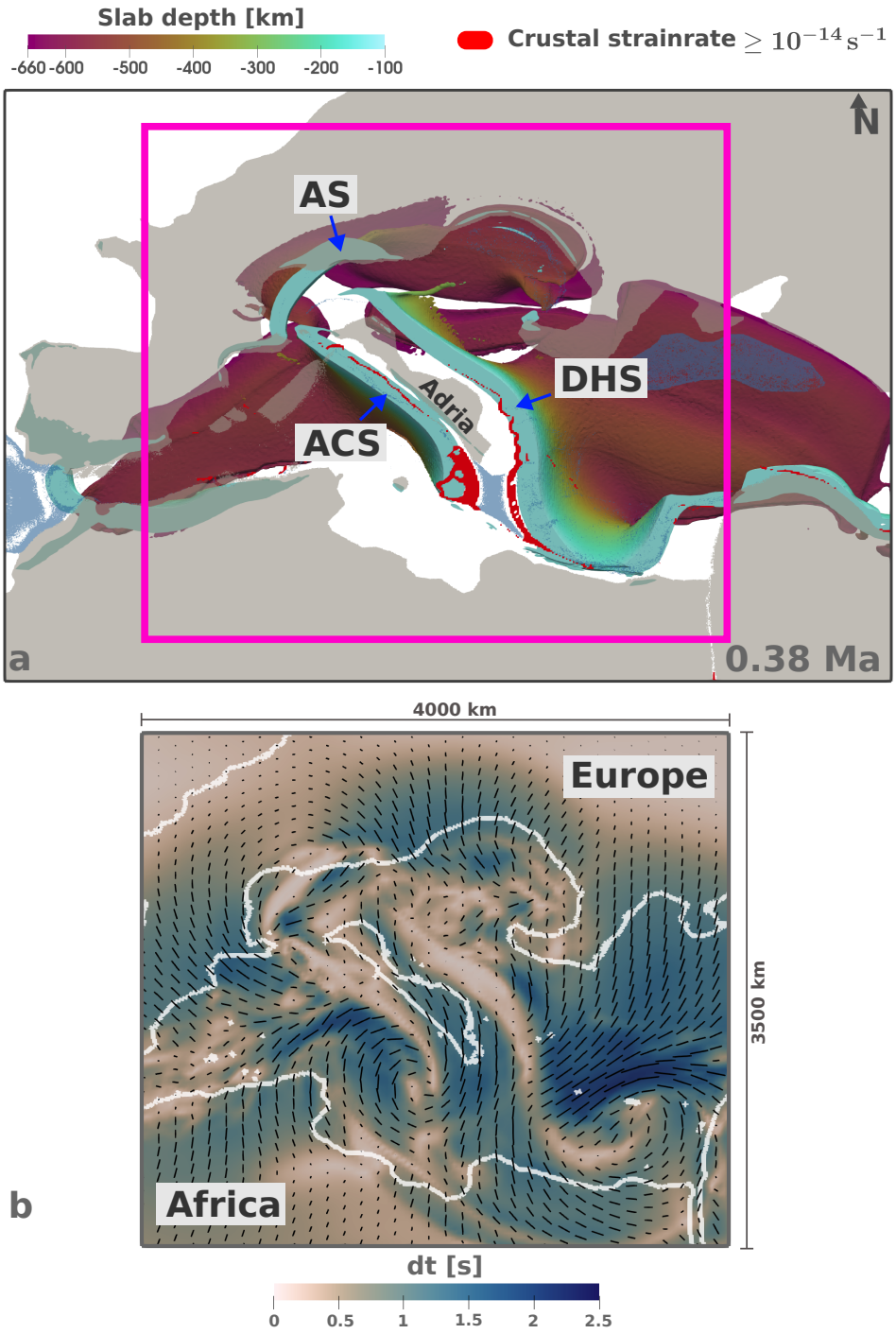

FIGURE 3.2: (a) shows the location where the seismic properties were calculated, indicated by the pink rectangle. The figure depicts the reference model REF2 after a simulation time of approximately 35 Myr. The names of the three distinct slabs are indicated in the figure: AS refers to the Alpine slab to the north, ApCS to the Apennines–Calabrian slab east of the Adriatic microplate, and DHS to the Dinaric–Hellenic slab west of Adria. The visualization is based on Schuler et al. (2025). (b) shows the splitting parameters of this area, evaluated through splitting intensities. The color indicates the delay time, while the bars represent the FPD. The white lines indicate the contours of the European continental crust in the north, the African continental crust in the south, and the Adriatic microplate in between.

variations in ξ and p. Figure 3.3b displays the quality factor β. High values of β suggest a region of high accumulated strain γ, but rather low delay time dt.

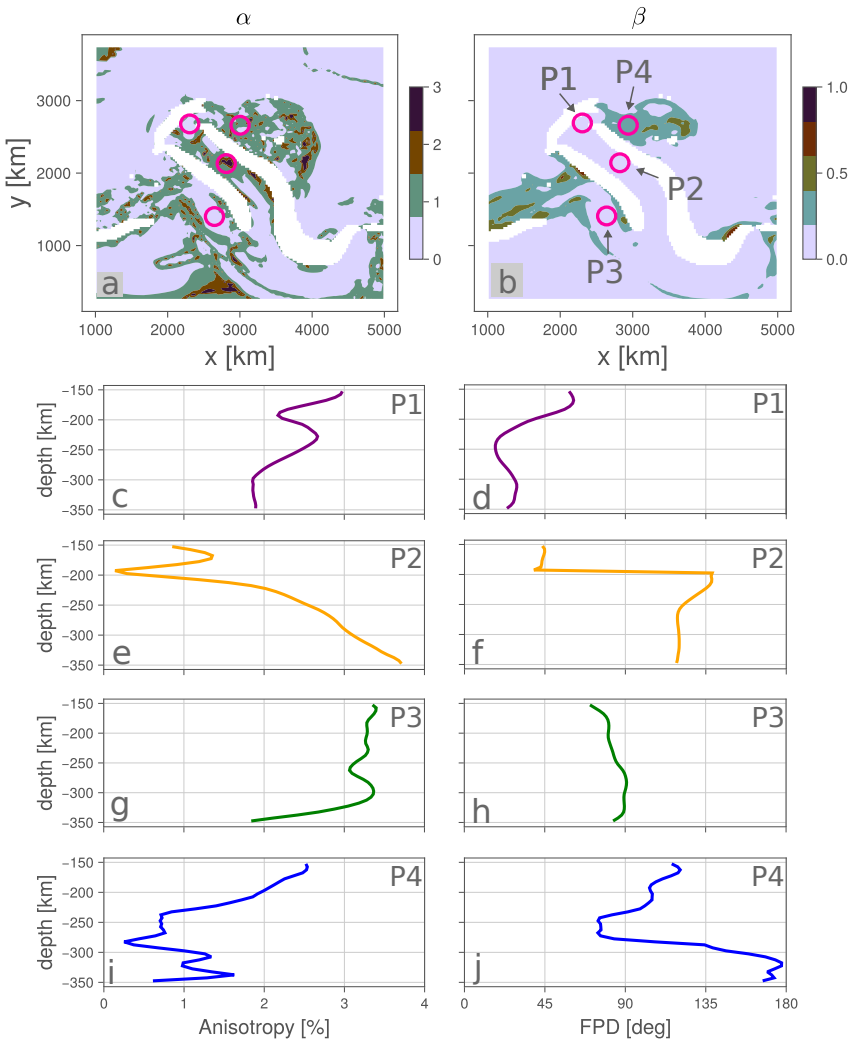

FIGURE 3.3: Depth profiles of ξ and p at four different locations. (a) and (b) show the quality factors α and β, respectively. For α, a ξ_{ch} of 3% and a p_{ch} of 45° were chosen. (c), (e), (g) and (i) display ξ at the four locations P1, P2, P3 and P4, while (d), (f), (h) and (j) show p at the same locations. (a) and (b) also indicate the positions of P1, P2, P3 and P4. 0° marks the north direction.

The accumulated strain γ for the observation region is plotted in Appendix 3.B. Points P1 to P4 were selected for several reasons. P1 is located in an area of low α and β south of the AS and the same applies to P3 west of the ApCS. P2 is characterized by high α and low β, whereas P4 lies in a region of intermediate α and β values. At location P1 ξ generally decreases from shallower to greater depths. p is constantly oriented northeast-southwest, while only slightly changing with depth. Similar to P1, location P3 is characterized by small changes in ξ with depth. Only beneath 300 km depth, ξ decreases rapidly and p remains nearly constant at around 90°. In contrast, location P2 shows a different pattern: two distinct layers are apparent in both ξ and p. Above 200 km depth, ξ is relatively low, around 1%, and p is approximately 45°. Below 200 km, p abruptly shifts to about 120°, while ξ rapidly increases to over 3.5% at a depth of 350 km. Location P3 shows quite constant p values for the whole depth range, around 90°. ξ remains nearly constant down to a depth of 300 km, below which

it decreases markedly. At location P4, the anisotropic strength decreases steadily from over 2% at 150 km depth to below 1% at 250 km depth and fluctuates around 1% at greater depths. The parameter p ranges between 80° and 120° above 300 km depth and increases sharply to 180° below this depth.

Overall, distinct domains were identified across the four observation points P1 to P4. P1 and P2 exhibit relatively constant ξ and p values, indicating that the upper mantle in these regions is largely homogeneous in terms of anisotropic seismic properties. In contrast, P3 and P4 show strong variations, including abrupt jumps in the polarization direction p.

3.5 Discussion

3.5.1 Model Verification through Comparison with Observations

The calculated splitting parameters for the central Mediterranean region and around the Adriatic microplate can now be compared with shear-wave splitting observations of this area. First, this comparison is carried out more generally for the entire area in order to verify the model results. We begin with the Apennines and Calabria region east of Adria and proceed counterclockwise around Adria to compare the different regions.

Southwest of the Apennines slab, represented in the model by the northern part of the ApCS, the FPD is oriented parallel to the trench. This is consistent with Hein et al. (2021) and Link and Rümpker (2023), indicating a first-order agreement with the model results. Further south, Scarfì et al. (2023) report trench-perpendicular FPD in central Italy, transitioning to a trench-parallel orientation at the arcuate tip of the Calabrian subduction zone. Southeast of this zone, a circular FPD pattern can be observed, consistent with observations from other studies (e.g., Civello and Margheriti, 2004; Baccheschi et al., 2007). This pattern is reproduced in the model results. In the central part of Adria, strong anisotropy is observed, with delay times up to 2.5s and the FPD oriented perpendicular to the trench. Further south, the FPD rotates toward a sub-parallel orientation with the Calabrian trench, but does not become fully parallel as is observed by Scarfì et al. (2023). One possible explanation is the shape of the modelled subduction zone, which is less circular than the actual Calabrian subduction zone (Maesano et al., 2017; Rappisi et al., 2022). Nevertheless, the circular FPD pattern around the Calabrian slab is well captured by the model and can be interpreted as toroidal flow around the slab edge (Civello and Margheriti, 2004). This is also in agreement with studies that calculated synthetic shear-wave splitting parameters based on geodynamic modeling of the central Mediterranean (Lo Bue et al., 2021, Lo Bue et al., 2022).

The anisotropy northeast of the Hellenic slab is constrained by Evangelidis et al. (2011), Yolsal-Çevikbilen (2014), Kaviris et al. (2018) and Erman et al. (2022), which report trench-perpendicular FPD induced by the retreating Hellenic slab, consistent with our model results. Further north, in the Dinarides region, the FPD is predominantly trench-perpendicular (Subašić et al., 2017, Salimbeni et al., 2022). In the splitting results of the model, the FPD is generally trench-perpendicular, but the delay times are smaller than reported near the Dinaric trench by Subašić et al. (2017). In the Pannonian Basin, a general northwest–southeast FPD is observed (Qorbani et al., 2016; Song et al., 2019; Petrescu et al., 2020b; Link and Rümpker, 2021), which is reproduced in the model results.

Generally, the model results show good agreement with shear-wave splitting data from previous studies. While not identical in all details, both the simulations and

the observations share first-order features, such as circularly oriented FPD around the slab edges of the Calabrian and Hellenic slabs, as well as trench-perpendicular FPD in the back-arc regions. In contrast, other areas, such as the Dinarides, reveal more pronounced discrepancies. Overall, the model provides a solid starting point for investigating the Alpine region in greater detail.

3.5.2 Detailed Comparison with Shear Wave Splitting Results of the Alpine region

In this section, we focus more closely on the Alpine region to characterize seismic anisotropy, identify possible explanations for the observed patterns and compare our results with those of Link and Rümpker (2023). The model outcomes are evaluated against both single-layer and two-layer anisotropy results presented in that study. This comparison helps to identify potential contributions from lithospheric and crustal anisotropy, components that are not explicitly accounted for in our model.

Seismic anisotropy beneath the Alps has been investigated by several studies by means of shear wave splitting analysis (e.g., Petrescu et al., 2020a; Hein et al., 2021; Link and Rümpker, 2023). For the comparison of model results and observations, the model output is converted into longitude/latitude coordinates in order to directly compare it with the measurements (Figure 3.4a). Before the detailed comparison, it should be noted that the conversion of the model to longitude–latitude coordinates is a simplification and the model's spatial geometry differs from reality. Therefore, comparisons should be made relative to specific regions rather than at exact longitude–latitude locations. Thus, in the model results, locations are referenced relative to the subducting slab, where delay times are near zero. In the observations, locations are referenced relative to the slab segments, framed with pink lines in the figures, which are compiled from seismic tomography studies.

First, the model results shown in Figure 3.4a are compared with the single-layer anisotropy results of Link and Rümpker (2023), depicted in Figure 3.4b. In the model, north of the Alpine slab, the FPD forms a circular pattern around the slab. The delay times are strongest in the west and gradually decrease toward the east. A similar circular pattern can be detected in the observations north of the slab, while the delay times remain consistently high. Further to the east, a transition to northwest–southeast aligned FPD is observed in both the model and the data, although the model predicts higher delay times. South of the Alpine slab, the model shows the FPD oriented parallel to the Alpine trench, with delay times reaching a maximum of around 1.5s. This pattern also extends through the gap between the Alpine and Apenninic slabs. In the observations, FPD parallel to the Alpine trench can also be seen in Figure 3.4b. However, this pattern is restricted to the region between the Adriatic microplate and the Alpine slab and is not present between the Alpine and Apenninic slabs. Instead, the FPD transitions into a circular pattern around the northeastern tip of Adria. Finally, the region west of the Apennines is considered. In the observations, a strong trench-parallel component is apparent, while further southwest, the FPD align with the extension direction of the Liguro-Provençal Basin (Link and Rümpker, 2023).

In the model, the FPD orientations southwest of the Apennines are quasi trench-parallel, as shown in Figure 3.2b and gradually transitions into the circular pattern observed around the Alps.

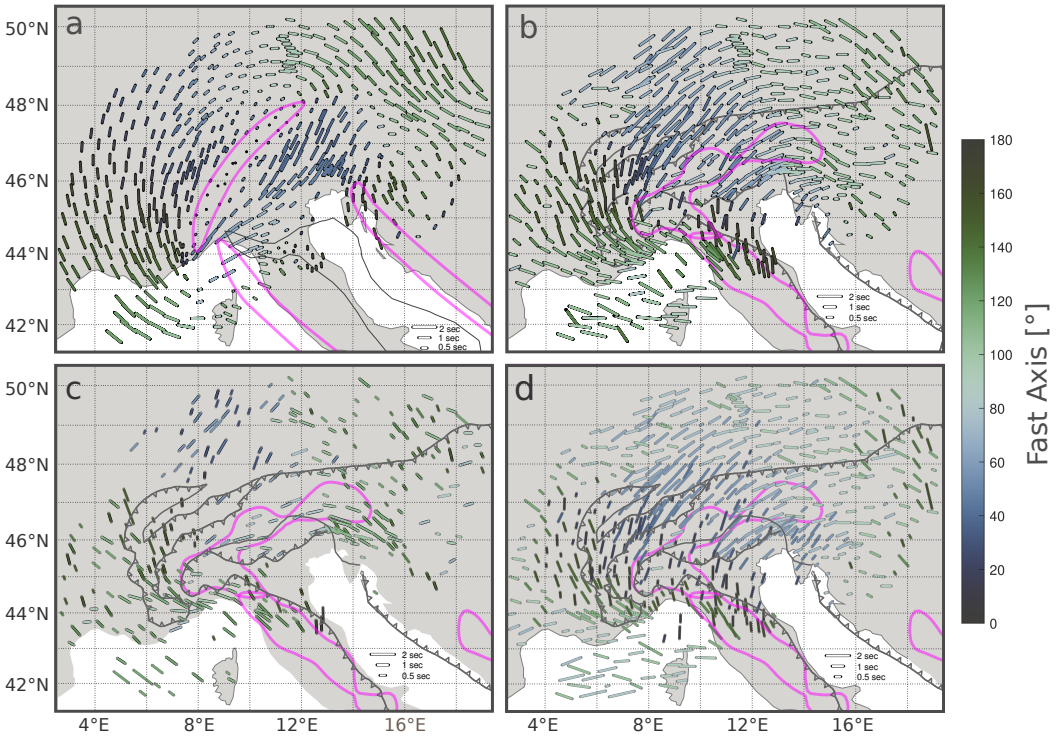

FIGURE 3.4: Comparison of model results with shear wave splitting observations. (a) shows the model results, while (b) shows the one layer shear wave splitting anisotropy from Link and Rümpker (2023). (c) and (d) show the results for a two-layer anisotropy model, with (c) representing the upper layer and (d) the lower layer, respectively. The color and orientation of the bars indicate the FPD, while their length represents the delay time. In (b), (c) and (d), the pink outline marks existing slab segments at a depth of 200 km, compiled from seismic tomography data (see Link and Rümpker, 2023). In (a), the pink outline represents the slab segments of the numerical model at a depth of 200 km. The data and plotting routines were provided by Frederik Link and are adapted from Link and Rümpker (2023). For information about the data and stations refer to Link and Rümpker (2023).

To further analyze the shear-wave splitting results, it is useful to consider the two-layer anisotropy measurements by Link and Rümpker (2023). In this approach, the inversion is carried out for two anisotropic layers with distinct delay times and FPD. Although the thickness of each layer is not known, comparisons with tectonic structures in the crust and large-scale asthenospheric flow often allow the anisotropic structure to be attributed to either lithospheric or asthenospheric origins. Figure 3.4c shows the results of the upper layer anisotropy. According to Link and Rümpker (2023), most of the features in the upper anisotropic layers can be attributed to lithospheric phenomena. The FPD in the Liguro-Provençal Basin to the west and the Pannonian Basin to the east align with the regional extension directions. In the Apennines and the Alps, the FPD aligns with the tectonic fault structure in the crust. Only two regions are considered to provide information about upper asthenospheric flow. One is the area northwest of the Alpine slab, where high delay times are observed and the FPD is perpendicular to the trench. Link and Rümpker (2023) hypothesize a possible recent slab break-off of the Alpine slab in this region. The other region, where the fast axes do not align with tectonic features and are therefore attributed to shallow asthenospheric flow, corresponds to the area northeast of the Alpine slab, where fast axes are oriented northwest–southeast. The model results show similar FPD in this

region as the upper-layer anisotropy. In the model, this feature extends throughout the entire asthenospheric depth, as shown in the depth-dependent anisotropy in Figure 3.3. Figure 3.4 shows the lower-layer anisotropy results, where northeast of the Alpine region the northwest–southeast oriented FPD persists in the lower layer, in good agreement with the model results. All of the lower-layer observations are interpreted to be of asthenospheric origin (Link and Rümpker, 2023). Therefore, they serve well as a basis for interpreting the model results. It exhibits many similarities with the model, including the large-scale circular pattern around the Alpine slab. In both the observations and the model results, the delay times decrease from west to east toward the northeastern slab edge of the Alpine slab. In the model, the flow around the Alps is continuous, whereas in the observations, FPD orientations perpendicular to the main flow appear at the outer margins of the flow field. Similarities are also observed south of the Alpine slab, where the FPD is trench-parallel and a circular pattern is observed around the northeastern edge of the Adriatic microplate. However, in the model, this trench-parallel trend continues through the gap between the Alpine and Apennines slab. Discrepancies are observed in the Liguro-Provençal Basin, where the FPD in the observations is aligned east–west and exhibits a sharp transition to the north. In contrast, the model shows a smooth rotation of the FPD from the Basin toward the north. The depth-dependent anisotropy (Figure 3.3) does not indicate distinct anisotropic layers, as the FPD remains nearly constant with depth.

3.5.3 Interpretation of the Model Results

By comparing the model results with the observations, a considerable number of similarities have been identified. This helps in interpreting the shear wave splitting results in these areas more robustly. The FPD north of the Alpine slab can in both cases be found as a northeast-southwest directed flow, parallel to the Alpine mountain belt. This can be interpreted as a mountain belt parallel asthenospheric flow around the Alps (e.g., Barruol et al., 2011; Petrescu et al., 2020a). The delay time decreases toward the east, reaching its lowest values around the northeastern edge of the Alpine slab. The FPD then continues around the northeastern edge of the Alpine slab, shifting to a northwest–southeast orientation, which corresponds to a slab gap in the eastern Alps (e.g., Qorbani et al., 2016; Kästle et al., 2020; Link and Rümpker, 2021). In the model, the slab gap extends to the base of the asthenosphere and the resulting synthetic splitting data corresponds well with the observations of Link and Rümpker (2023). This suggests that mantle flow through the slab gap occurs across most of the asthenosphere, which is also consistent with the combined P-wave and splitting-intensity anisotropic tomography by Rappisi et al. (2025). South of the Alpine slab, the FPD is mainly parallel to the Alpine trench (e.g. Löberich and Bokelmann, 2020). The model shows, that this can be interpreted as an asthenospheric escape flow from beneath the Adriatic microplate to the northeast (e.g., Holt et al., 2017; Király et al., 2018a; Király et al., 2018b). At point P1 in Figure 3.3, the polarization direction remains nearly constant with depth, indicating that a single anisotropic layer can be assumed in this area.

In other areas, differences between the model and the observations become apparent. These discrepancies may be attributable to a number of factors. The model may be incorrect in certain locations, while the observations may be erroneously interpreted in others. One discrepancy is the notable delay time between the Alpine and Apennines slab and the FPD, which is oriented parallel to the Alpine slab. In the model, this can be attributed to mantle flow between these two slabs. In the observations, the FPD turns from northwest-southeast in the region of the Apennines

to northeast-southwest in the Alpine region. This means that the FPD stays trench-parallel. This strongly suggests that the connection between the Alpine and Apennine slabs acts as a barrier to mantle flow, allowing escape flow only towards the east (e.g., Rappisi et al., 2025). Another difference is the abrupt change in FPD orientation at the outer margin of the flow around the Alps. This phenomenon is evident in the observations, whereas the asthenospheric flow in the model produces a continuous FPD pattern. Therefore, the deviation observed could be attributed to features unrelated to asthenospheric flow, such as crustal structures. Apart from that, we see deviations in the region of the Liguro-Provençal Basin. In the observations, two distinct layers are differentiated. The upper one is a continuation from the flow around the Alpine slab, whereas the lower one shows an abrupt shift in FPD to east-west orientation. In the model, the FPD in the region of the Liguro–Provençal Basin represents a continuation of the flow around the Alps. The model results offer no evidence for an abrupt change in anisotropic properties with depth. Therefore, the FDP seems to be a direct result of the large-scale asthenospheric flow, which remains largely consistent with depth (Figure 3.1). We argue that the lower-layer anisotropy in this area (Figure 3.4d) may originate from lower mantle anisotropy or from a different slab geometry than in the model. Rappisi et al. (2025) suggest a slab gap in the Apenninic slab at around 400 km, which may also affect the region above the transition zone, generating anisotropy there.

To summarize the interpretation of the synthetic shear-wave splitting results, the Alpine region is subdivided into areas A–G (Figure 3.5). Area A is interpreted as a region where anisotropy remains nearly constant with depth (Figure 3.1). Close to the Apennines subduction, the FPD is sub-trench-parallel. Further to the northwest, the FPD transitions into the greater flow field around the Alps and thereby shifts its direction to the north. This region is labeled with B and denotes the flow around the Alpine subduction zone. As can be seen in Figure 3.1, the FPD stays constant with depth. Region C shows a shift in FPD relative to region B, with the orientation changing to northeast–southwest. This can be attributed to the slab gap, which opened in the model around 20 Ma (Figure 3.7). In this area, the FPD is also relatively constant with depth.

South of the Alps, two different regions D and E can be identified. Both are characterized through trench-parallel FPD with respect to the Alpine slab, however, region D indicates an escape flow through the gap between the Alpine slab and the Apennines slab to the northwest, while region E indicates an escape flow to the northeast between the Alpine slab and the Adriatic microplate. The observations show no evidence of a slab gap between the Apennines and the Alps based on the splitting results. Region E agrees well with observations and is interpreted as mantle escape from Adria, with the Alpine slab acting as a barrier. Point P1 in Figure 3.3 shows the depth profile in this region. Although some variations in the anisotropic properties can be detected, this part as a whole can be interpreted as one anisotropic layer. Region F describes the region below the Adriatic microplate. This region shows a strong signal in FPD, which is trench-parallel to the Apennines and Dinaric slab. By looking at the depth profile at Point P2 (Figure 3.3), two distinct anisotropic layers are observed. Above 200 km depth, the FPD is northeast, following the plate motion of the Adriatic microplate. At greater depths, the FPD switches to a northwest-southeast direction, which produces the signal that can be seen in the splitting parameters.

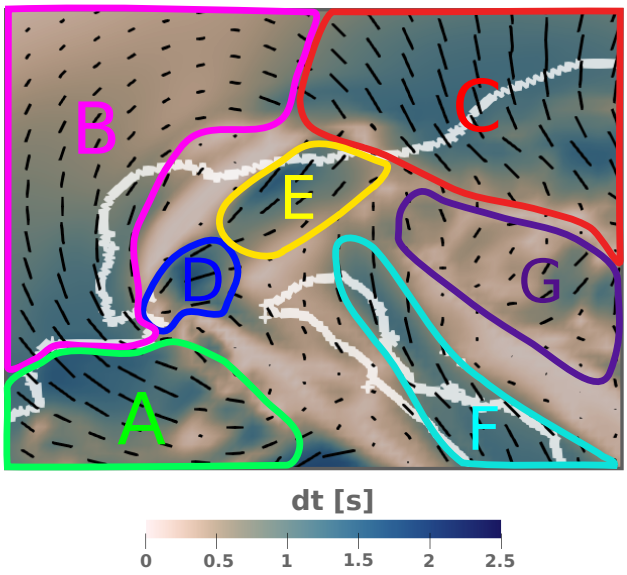

FIGURE 3.5: Synthetic shear-wave splitting results for the Alpine region. Different colors indicate regions labeled A–F.

Lastly, region G is discussed, which shows the highest complexity in the study area with a spatially changing FPD and delay time. Depth slices show that in this region, anisotropy varies with depth, so that the splitting parameters show no preferred orientation. The depth profile of point P4 in Figure 3.3 reveals two layers. The upper layer is trench perpendicular to the Dinaric slab and the lower layer, starting beneath 250km is oriented north-south. However, this pattern changes to the south (Figure 3.1). Generally, the region between the Dinarides and Carpathians is characterized by low delay times, but high accumulated strain (see β parameter in Figure 3.3b). This may indicate rather vertically oriented fast axes of the crystals in these regions (Kruse et al., 2024). The same holds for the western Mediterranean region. In both regions, a slab break-off event occurred, followed by rapid slab sinking. However, the analysis of these regions needs more in-depth analysis of the fast axis orientations, which is beyond the scope of this chapter.

3.5.4 Limitations and Future Directions

As previously discussed, vertical fast axis orientation of the crystals can also play a role in the Mediterranean (e.g. Rappisi et al., 2025). The fast axis orientation in the model can be estimated from the elastic tensor and provides additional insight for interpretation. Additionally, the CPO calculation employed here is based on the assumption that only A-type olivine is present. However, in wet environments, such as subduction zones, B-type olivine plays an important role (e.g. Kneller et al., 2005). B-type olivine offers different seismic properties and could therefore change the anisotropic pattern. Furthermore, the contribution of lithospheric anisotropy has not been taken into account. However, this may help align observations and model results, as strong anisotropy is also evident in slab regions (Figure 3.4). In general, it should be noted that the thermomechanical model is an approximation of reality. For example, the subducting slabs in the model are relatively continuous and do not develop small-scale slab windows, such as those observed in the Apennines–Calabrian and Dinaric–Hellenic slab systems (e.g., Faccenna et al., 2004; Rappisi et al., 2022). These features influence mantle flow and can therefore also affect the alignment of crystals within the mantle.

The model results provide temporal snapshots of mantle flow, allowing the calculation of seismic anisotropic properties and synthetic splitting data for different time intervals and stages. This would enable a more precise identification of the processes responsible for the observed shear wave splitting results and help distinguish between mantle flow patterns that are preserved in the splitting signal and patterns that are overprinted.

3.6 Conclusions

We thoroughly compared synthetic seismic splitting data of a thermomechanical simulation of the Mediterranean subduction dynamics with observations. In particular, the Alpine region was compared in detail with the shear-wave splitting results of Link and Rümpker (2023). It was especially helpful to consider the results of two-layer anisotropy inversion, as they help interpret the splitting observations in terms of asthenospheric flow.

Overall, we found evidence of large-scale mantle flow around the Alpine subduction zone, parallel to the Alpine belt. In the east, this pattern is interrupted by northwest–southeast FPD, likely reflecting a break-off of the Alpine slab. South of the Alpine slab, trench-parallel fast-axis orientations in both the model and observations indicate an escape flow from Adria towards the northeast. The similarities between synthetic and observed splitting parameters strengthen these conclusions, as they can be directly linked to the 3D mantle flow in the thermomechanical simulation. However, differences between the model and the observations also became apparent. For instance, a gap between the Apenninic slab and the Alpine slab in the model causes strong delay times and trench-perpendicular FPD. Since this signal is completely absent in the observations, we conclude that the Alps and Apennines act as a barrier, preventing mantle flow in that direction. In the Liguro–Provençal Basin, the model suggests constant anisotropy with depth and a smooth transition of the FPD into circular flow around the Alpine slab. In contrast, the observations show an abrupt FPD change between the basin and the northern region, which cannot be explained by the modelled asthenospheric flow and may reflect deeper mantle anisotropy. Furthermore, the asthenosphere beneath Adria exhibits two distinct anisotropic layers. In the upper layer, the FPD is aligned with the motion of the Adriatic microplate since it began rotating relative to Africa, whereas the lower layer is aligned trench-parallel to the surrounding Apennines and Dinaric slabs, indicating an escape flow of mantle material to the north.

3.7 Appendix

3.A Comparison to Reference Model

Here, we compare the REF model (previous chapter and Schuler et al. (2025)) with the REF2 version introduced in this chapter. The REF2 model has a different numerical resolution, with 192 grid cells in the z-direction instead of 128 in REF. Apart from that, the grid spacing is uniformly distributed, yielding a vertical resolution of about 3.7 km. Some parameters of several weak zones have also changed. The north–south extent has been increased from 3500 km to 4000 km. The friction angle of weak zones 4 and 6 was reduced from 4.5° to 3.5°. In weak zone 5, the cohesion decreased from 10^7 MPa to $5 \cdot 10^6$ MPa, and the friction angle from 5° to 3°. For weak zones 9 and 10, the friction angle was reduced from 12.5° to 10°. The depth of weak zone 3 was decreased to 40 km, while the depths of weak zones 1 and 9 were increased to 120 km and 60 km, respectively.

Figure 3.6 shows a comparison of the REF model with the REF2 model. The mapview indicates that both simulations exhibit similar behaviour. The subduction zones southwest and southeast of Adria reach almost identical positions, while the continental block in the western Mediterranean shows slightly different motion. Figure 3.7 allows a clear comparison of the retreat and dynamic behaviour of the Alpine slab between both models. Overall, the dynamics of the Alpine slab are almost identical, with only a small time shift of about 1 Myr. The plate motion of Adria also appears similar, as shown in Figure 3.7.

3.B Accumulated Strain

The accumulated strain for the model over the last 24 Myr has been calculated based on the approach of Kruse et al. (2024). Note that in these calculations, the total strain rate was used rather than only the viscous strain as in Kruse et al. (2024). The resulting γ for the observation area is shown in Figure 3.8. Regions of high γ are observed in the Carpathians, west of the ApCS in the western Mediterranean and northeast of the southern part of the DHS.

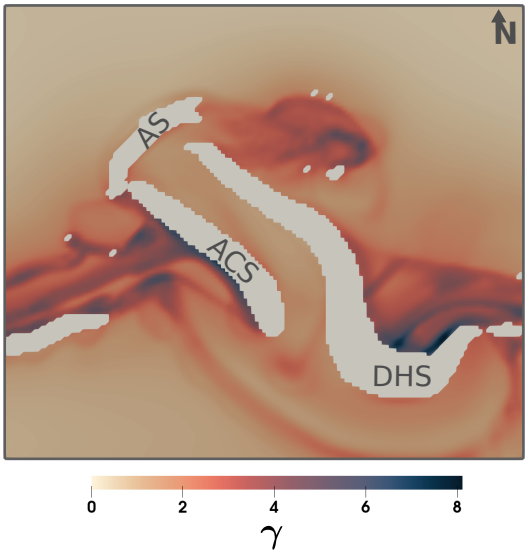

FIGURE 3.8: Depth-averaged accumulated viscous strain γ. White areas indicate regions where more than 20% of the particles in the depth column were not mantle material.

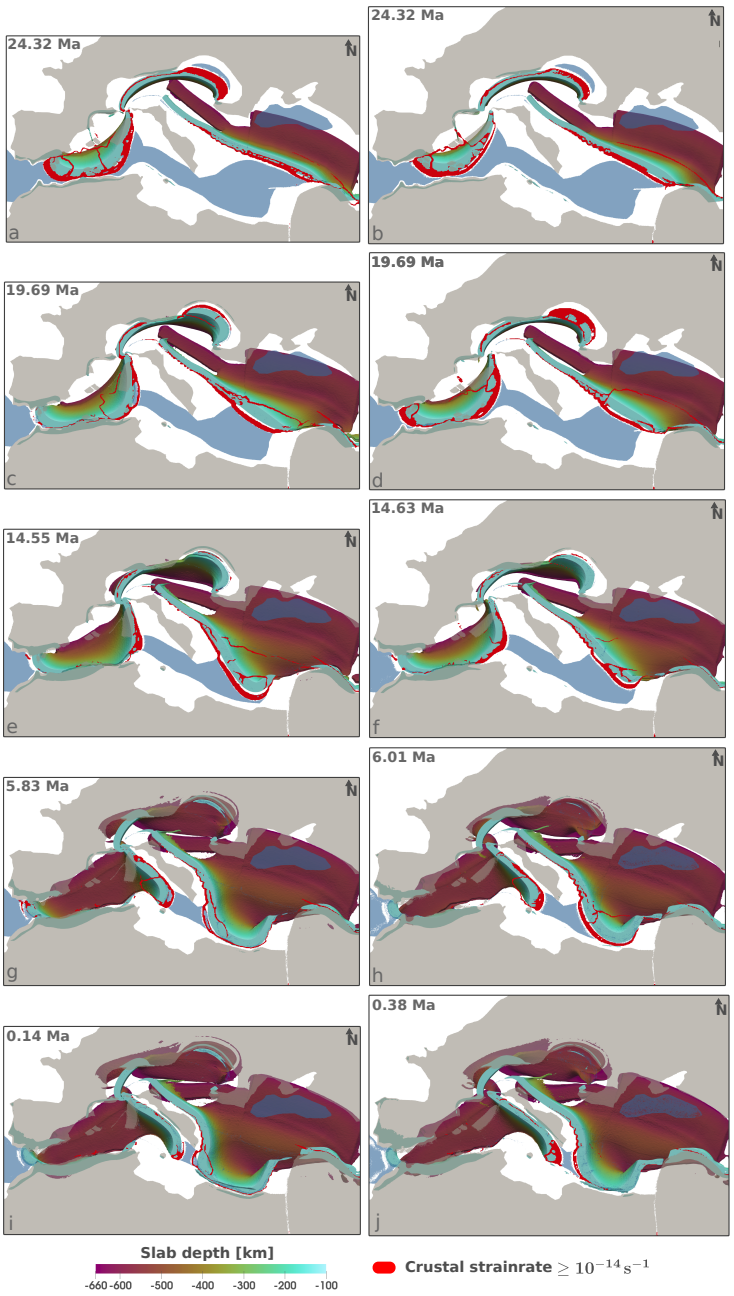

FIGURE 3.6: Comparison of the reference model (REF) from Chapter 2 and the reference model (REF2) from this chapter. The left column shows the time evolution of REF in mapview, while the right column shows REF2, also in mapview. The visualization is based on Schuler et al. (2025).

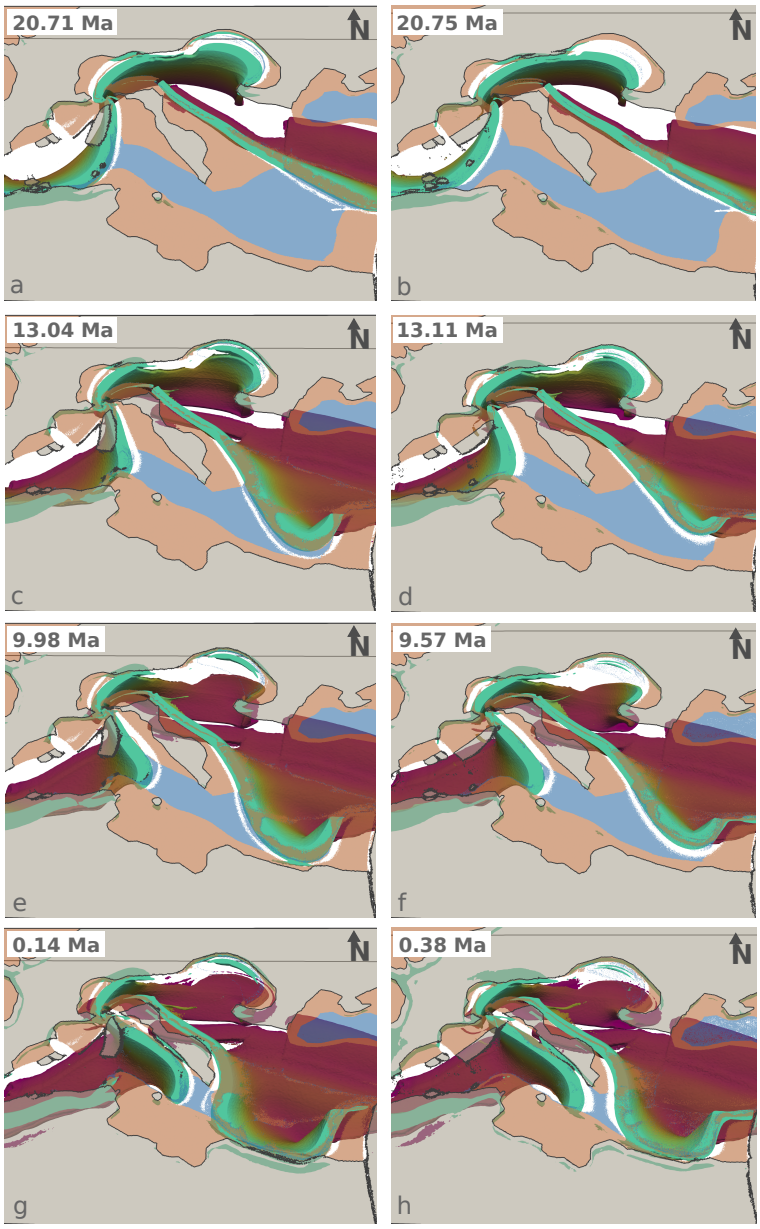

FIGURE 3.7: Comparison of the reference model (REF) from Chapter 2 and the reference model (REF2) from this chapter. The left column shows the time evolution of REF in a zoomed view of the area around the Adriatic microplate. The right column shows the same section for REF2. The visualization is based on Schuler et al. (2025).

Chapter 4

Adjoint Solver for Nonlinear Stokes Flow: Implementation with Automatic Differentiation and Sensitivity Analysis

4.1 Introduction

To investigate large-scale mantle and lithospheric deformation over million-year timescales, or to examine crustal deformation at smaller scales, the Stokes equations can be solved to gain insight into these processes (e.g., Duretz and Schmalholz, 2015; Lourenço et al., 2020; Duarte et al., 2024). In numerical modeling, the focus often lies on particular processes, such as the plate motion of a subducting plate or the ascent velocity of a mantle plume in the asthenosphere. This leads to a key question: which input parameters exert the greatest influence on the output of interest?

Answering this question can be challenging, as the number of input parameters, often referred to as material parameters, can be extremely large. In typical simulations employing viscous rheologies with nonlinear creep laws as viscosity parameterizations, each phase, such as mantle or crustal phases, can involve 10 to 20 parameters (e.g., Pons et al., 2023; Schuler et al., 2025). The influence of material parameters on an output of interest can be straightforwardly evaluated using a finite-difference approach. Therefore, we introduce a scalar-valued function F, referred to as the objective function. This function depends on the solution of the Stokes equations. Given a solution to the Stokes equations, F computes a meaningful measure that represents the quantity of interest. In the case of a rising plume, the objective function F could, for example, be defined as the average uplift in the crust above the plume. In the second step, we aim to quantify how the material parameters influence the objective function F. In other words, we are interested in the gradients $\frac{dF}{d\mathbf{p}}$, where $\mathbf{p} \in \mathbb{R}^k$ is a vector containing all material parameters. To compute the gradient $\frac{dF}{dp_i}$, where p_i denotes the i-th component of $\mathbf{p}$, the simplest approach is to solve the Stokes equations twice and apply a forward (or backward) finite-difference scheme:

$$\frac{dF}{dp_i} \approx \frac{F(\mathbf{u}(\mathbf{p} + h\mathbf{e}_i)) - F(\mathbf{u}(\mathbf{p}))}{h}. \tag{4.1}$$

Here, $\mathbf{u}$ denotes the forward solution of the Stokes equations, which depends on $\mathbf{p}$, h is a small scalar perturbation and $\mathbf{e}_i$ is the i-th unit vector. To evaluate the gradients with respect to all parameters in $\mathbf{p}$, a total of $k + 1$ simulations must be performed. As the number of phases and associated material parameters increases, the computational cost of this approach grows rapidly. Dropping the assumption of

phase-wise parameters, where each parameter is constant within a phase, significantly increases the complexity. Instead, we now aim to perturb every material parameter at every point in the numerical domain. In this case, the computational cost of the finite-difference approach described in Equation 4.1 becomes prohibitively high. The number of required forward simulations then scales with numerical resolution, making the approach infeasible for large-scale 2D models and in 3D settings.

To address this issue, the adjoint method can be used to efficiently calculate the gradients of an objective function F (e.g., Giles and Pierce, 2000; Gunzburger, 2000; Givoli, 2021; Reuber, 2021). The adjoint method can be derived in two different ways: the "continuous" or "optimize-then-discretize" approach and the "discrete" or "discretize-then-optimize" approach (e.g., Giles and Pierce, 2000, Reuber, 2021). In the optimize-then-discretize approach, the starting point is to minimize an objective functional under the constraint, that the forward problem is satisfied. This can be formalized as a constrained optimization problem using a Lagrangian functional. The variations of this functional need to vanish, which finally yields gradients $\frac{dF}{dp_i}$. This method has previously been applied to Stokes flow in geodynamics (e.g., Liu and Gurnis, 2008; Horbach et al., 2014; Worthen et al., 2014; Ratnaswamy et al., 2015; Ghelichkhan and Bunge, 2016; Horbach, 2020; Reuber et al., 2020a). In this chapter, the second approach, the "discretize-then-optimize" method, is used. It is based on the already discretized forward problem, which in our case corresponds to the Stokes equations. Therefore, any change in the forward problem also requires changes to the adjoint solver. To address this, we use automatic differentiation (AD) to construct the adjoint solver. With this approach, updates to the forward solver are automatically incorporated into the adjoint solver, avoiding manual adjustments.

In this chapter, we use the Julia programming language (Bezanson et al., 2017), in particular, the AD-capabilities of Enzyme.jl (Moses and Churavy, 2020; Moses et al., 2021), to implement a problem-agnostic adjoint solver for the Stokes solver JustRelax.jl (Aellig et al., 2025). The discrete adjoint method itself has previously been applied to Stokes flow in geodynamics (e.g., Li et al., 2017; Reuber et al., 2018; Reuber et al., 2020a). When combined with AD, it has been employed in various fields (e.g., Müller and Cusdin, 2005; Marta et al., 2007; Roth and Ulbrich, 2013; Zhang et al., 2023; Utkin et al., 2025), and also in geodynamics for viscous Stokes flow simulations (Ghelichkhan et al., 2024). In this work, we build on previous efforts by developing an AD-based adjoint solver using the discrete adjoint method and applying it to the compressible Stokes equations, with a particular focus on lithospheric dynamics and complex nonlinear visco-elastic rheology, including a combined dislocation and diffusion creep rheology.

The first part of this chapter details the implementation of the adjoint solver and the use of automatic differentiation. In the second part, the example of a mantle plume head rising through the asthenosphere is used to demonstrate the application of the discrete adjoint method for sensitivity analysis (e.g. Reuber et al., 2018; Reuber et al., 2020a). The rising velocity of the plume head is quantified by the objective function F, and in that case, the gradients of F with respect to the material parameters are referred to as sensitivities (e.g., Reuber et al., 2018; Reuber et al., 2020a). This part outlines how sensitivities for different material parameters can be scaled to enable a comparison and to determine the most influential parameters. In the final part of the chapter, the adjoint solver is applied to a 2D subduction model with a nonlinear visco-elastic rheology, investigating the horizontal motion of the subducting plate through adjoint sensitivities.

4.2 Forward Problem

4.2.1 Stokes Equations

In order to account for deformation over long timescales, we solve the compressible Stokes equations, where the momentum and mass conservation equations are formulated as follows:

$$\nabla \cdot \boldsymbol{\tau} - \nabla P + \rho \mathbf{g} = \mathbf{0}, \tag{4.2}$$

$$\nabla \cdot \mathbf{v} + \frac{1}{K}\frac{DP}{Dt} = 0, \tag{4.3}$$

where $\mathbf{v} = (v_x, v_z)^T$ is the velocity vector, $\boldsymbol{\tau}$ is the deviatoric stress tensor, P the pressure, ρ the density and $\mathbf{g}$ is the gravitational acceleration vector, which is only non-zero in the vertical z-direction. K is the bulk modulus and $\frac{D}{Dt}$ is the material derivative.

We employ a viscoelastic rheology, wherein the shear stress $\boldsymbol{\tau}$ is related to the strain rate $\dot{\boldsymbol{\varepsilon}}$ through the following constitutive equation:

$$\dot{\boldsymbol{\varepsilon}} = \frac{\boldsymbol{\tau}}{2\eta} + \frac{1}{2G}\frac{D\boldsymbol{\tau}}{Dt}, \tag{4.4}$$

where η is the viscosity and G is the shear modulus. The strainrate $\dot{\boldsymbol{\varepsilon}}$ is defined as:

$$\dot{\boldsymbol{\varepsilon}} = \frac{1}{2}\left(\nabla \mathbf{v} + \nabla \mathbf{v}^{\mathrm{T}}\right). \tag{4.5}$$

Unless stated otherwise, free-slip boundary conditions are applied at the boundaries of the rectangular numerical domain. This implies that the velocity component normal to the boundary is zero at the boundary, and also the tangential component of the deviatoric stress is zero.

4.2.2 Numerical Implementation

Equations 4.2 and 4.3 are solved with the accelerated pseudo-transient method (Räss et al., 2022). Therefore, a pseudo-time derivative is added to Equations 4.2 and 4.3 and the solution variables are updated by explicit time integration until the residuals satisfy a prescribed tolerance:

$$\nabla \cdot \boldsymbol{\tau} - \nabla P + \rho \mathbf{g} = \tilde{\rho}\frac{\partial \mathbf{v}}{\partial \phi}, \tag{4.6}$$

$$\nabla \cdot \mathbf{v} + \frac{1}{K}\frac{DP}{Dt} = \frac{1}{\tilde{K}}\frac{\partial P}{\partial \phi}, \tag{4.7}$$

where ϕ is the pseudo time and the parameters $\tilde{\rho}$ and $\tilde{K}$ are numerical parameters (see Appendix 4.A). These equations are then explicitly discretized. A pseudo-transient term is also added to Equation 4.4:

$$\dot{\boldsymbol{\varepsilon}} - \frac{\boldsymbol{\tau}}{2\eta} - \frac{1}{2G}\frac{D\boldsymbol{\tau}}{Dt} = \frac{1}{2\tilde{G}}\frac{\partial \boldsymbol{\tau}}{\partial \phi}, \tag{4.8}$$

where $\tilde{G}$ is a numerical parameter (see Appendix 4.A). For a better convergence, this equation is discretized using an implicit scheme (Räss et al., 2022):

$$\dot{\boldsymbol{\varepsilon}} - \frac{\boldsymbol{\tau}^{n+1}}{2\eta} - \frac{(\boldsymbol{\tau}^{n+1} - \boldsymbol{\tau}^{o})}{2G\Delta t} = \frac{1}{2\tilde{G}} \frac{\boldsymbol{\tau}^{n+1} - \boldsymbol{\tau}^{n}}{\Delta\phi} \,, \tag{4.9}$$

where $\boldsymbol{\tau}_o$ is the old stress from the previous timestep, which is rotated (e.g., Rubinstein and Atluri, 1983; Gerya, 2019). Δt describes the discrete physical timestep and the superscript n describes the pseudo-transient step. Equation 4.9 can be rearranged for $\Delta\boldsymbol{\tau} = \boldsymbol{\tau}^{n+1} - \boldsymbol{\tau}^{n}$, which updates $\boldsymbol{\tau}$ every pseudo timestep:

$$\boldsymbol{\tau}^{n+1} - \boldsymbol{\tau}^{n} = \left(2\eta\dot{\boldsymbol{\varepsilon}} + \eta\frac{\boldsymbol{\tau}^{0} - \boldsymbol{\tau}^{n}}{G\Delta t} - \boldsymbol{\tau}^{n}\right)\left(\frac{\eta}{\tilde{G}\Delta\phi} + 1 + \frac{\eta}{G\Delta t}\right)^{-1} . \tag{4.10}$$

For the implementation, we introduce the variable $\dot{\boldsymbol{\varepsilon}}_v = (\dot{\varepsilon}_{xx}, \dot{\varepsilon}_{yy}, \dot{\varepsilon}_{xy})^T$, representing the strain rate tensor $\dot{\boldsymbol{\varepsilon}}$ in Voigt notation. Analogously, we define a vector $\boldsymbol{\tau}_v = (\tau_{xx}, \tau_{yy}, \tau_{xy})^T$ to represent the stress tensor $\boldsymbol{\tau}$. Algorithm 1 displays the pseudo-transient iteration loop of the forward solver. This is particularly useful for later comparison with the implementation of the adjoint solver. First, the velocity divergence is computed. This is then used to evaluate the residual R_P (residual of Equation 4.3), allowing the pressure P to be updated in line 4. Next, the strain rate is computed, which is then used in line 6 to calculate the stress update $\Delta\boldsymbol{\tau}_v$. The new stress $\boldsymbol{\tau}_v^n$ is then obtained by updating it based on the stress from the previous iteration $\boldsymbol{\tau}_v^{n-1}$ and the stress update $\Delta\boldsymbol{\tau}_v$. Using this information, the residual $\mathbf{R_v}$ (residual of Equation 4.2) can be calculated, and the velocity $\mathbf{v}$ is updated. These steps are repeated until the error is below a predefined tolerance.

Algorithm 1 : Pseudocode of forward solver. Implementation details of the Stokes solver in the Julia package JustRelax.jl. The pseudocode shows the inner iteration loop of the pseudo-transient solver.

Data : Material Parameters η, ρ, G, K
Result : Solution of Forward Problem $\mathbf{v}$, P
`# Pseudo-Transient Iteration loop`
1 **while** *error* $>$ *tolerance* **do**
2 compute $\mathrm{div}(\mathbf{v})$
3 compute $R_P(\nabla\mathbf{v}, P)$
4 update $P(R_P)$
5 compute $\dot{\boldsymbol{\varepsilon}}_v(\mathbf{v})$
6 compute $\Delta\boldsymbol{\tau}_v(\boldsymbol{\tau}_v^{n-1}, \dot{\boldsymbol{\varepsilon}}_v, \boldsymbol{\tau}_{old})$
7 update $\boldsymbol{\tau}_v^n(\boldsymbol{\tau}_v^{n-1}, \Delta\boldsymbol{\tau}_v)$
8 compute $\mathbf{R_v}(\boldsymbol{\tau}_v^n, P)$
9 update $\mathbf{v}(R_\mathbf{v})$

4.2.3 Code Architecture of JustRelax.jl

The forward solver and the adjoint solver, which is discussed in the next section, are both implemented in the Julia programming language. Material properties and the deformation history are advected using a Particle-In-Cell method (Harlow and Welch, 1965) provided by the Julia package JustPIC.jl (de Montserrat et al., 2025). This package offers an easy-to-use interface for the advection. It is not part of the forward solver itself and can therefore be modified independently of the main routine. GeoParams.jl performs scalar rheology calculations and manages the material

parameter database. The code is parallelized for both CPU and GPU architectures. This is done with the help of two packages: ParallelStencil.jl (Omlin and Räss, 2024) and ImplicitGlobalGrid.jl (Omlin et al., 2022). With ParallelStencil.jl, efficient kernel functions can be written for both CPU and GPU. These kernel functions can also be combined with the Julia package Enzyme.jl for automatic differentiation via ParallelStencil.jl. ImplicitGlobalGrid.jl handles domain decomposition and communication between GPUs or CPUs.

4.3 Adjoint Problem

4.3.1 Discretize-Then-Optimize Method

The discretize-then-optimize adjoint method can be used to calculate gradients of a scalar-valued objective function F with respect to the input parameters of the forward problem. This is commonly applied in optimization problems that aim to minimize the discrepancy between the model result and observations (e.g., Bunge et al., 2003; Li et al., 2017; Ghelichkhan et al., 2024). However, the adjoint method can also be applied for an objective function F that depends solely on the solution of the forward problem (e.g., Reuber et al., 2018; Reuber et al., 2020a; Reuber, 2021). This can be beneficial for sensitivity analysis of the forward model with respect to a specific output of interest. In this chapter, we define the objective function F as the sum of one velocity component of the forward solution, in this case the z-component v_z:

$$F(v_z(\mathbf{p}))\,, \tag{4.11}$$

where $\mathbf{p} = (\eta, \rho)^T$ are the material parameters of the forward problem. It should be noted that, throughout this chapter, we are interested in the sum of the velocities at specific locations within the model domain rather than over the entire domain. If different components of the solution vector are combined in the objective function, they will need to be weighted according to the application (e.g. Ghelichkhan et al., 2024). However, this is beyond the scope of this chapter. The resulting gradients are hereafter referred to as sensitivities, following the terminology used in Reuber et al. (2020a) and Reuber (2021). The discretize-then-optimize approach starts with the discretized forward problem, which we express in residual form:

$$\mathbf{r}(\mathbf{u}(\mathbf{p}), \mathbf{p}) = \begin{pmatrix} \mathbf{R_v} \\ R_P \end{pmatrix} = \begin{pmatrix} \nabla \cdot \boldsymbol{\tau} - \nabla P + \rho \mathbf{g} \\ \nabla \cdot \mathbf{v} + \frac{1}{K}\frac{DP}{Dt} \end{pmatrix}. \tag{4.12}$$

Here, we introduce the combined solution vector of the forward problem $\mathbf{u}(\mathbf{p}) = (\mathbf{v}, P)^T$, where $\mathbf{u}$ depends on the input parameters $\mathbf{p}$. As $\mathbf{u}$ is the discrete solution to the converged forward problem it satisfies:

$$\mathbf{r}(\mathbf{u}(\mathbf{p}), \mathbf{p}) = \mathbf{0}\,. \tag{4.13}$$

We are interested in the gradients of F with respect to the material parameters $\mathbf{p}$. Therefore the total derivative of F with respect to the input parameters $\mathbf{p}$ is evaluated:

$$\frac{dF}{d\mathbf{p}} = \frac{\partial F}{\partial \mathbf{p}} + \frac{\partial F}{\partial \mathbf{u}}\frac{d\mathbf{u}}{d\mathbf{p}}\,. \tag{4.14}$$

In the absence of a regularization term, $\frac{\partial F}{\partial \mathbf{p}}$ is zero. $\frac{\partial F}{\partial \mathbf{u}}$ can be calculated by differentiating the objective function with respect to $\mathbf{u}$. For the last term $\frac{d\mathbf{u}}{d\mathbf{p}}$, we make use

of the fact that, for different parameter sets $\mathbf{p}$, the residual of the forward problem should generally satisfy $\mathbf{r} = \mathbf{0}$ within a numerical tolerance:

$$\frac{d\mathbf{r}}{d\mathbf{p}} = \frac{\partial \mathbf{r}}{\partial \mathbf{p}} + \frac{\partial \mathbf{r}}{\partial \mathbf{u}} \frac{d\mathbf{u}}{d\mathbf{p}} = \mathbf{0}\,. \tag{4.15}$$

This can be rearranged for $\frac{d\mathbf{u}}{d\mathbf{p}}$:

$$\frac{d\mathbf{u}}{d\mathbf{p}} = -\left(\frac{\partial \mathbf{r}}{\partial \mathbf{u}}\right)^{-1} \frac{\partial \mathbf{r}}{\partial \mathbf{p}}\,, \tag{4.16}$$

where $\frac{\partial \mathbf{r}}{\partial \mathbf{u}}$ is the Jacobian matrix $\mathbf{J}$ of the forward problem:

$$\frac{d\mathbf{u}}{d\mathbf{p}} = -\mathbf{J}^{-1} \frac{\partial \mathbf{r}}{\partial \mathbf{p}}\,. \tag{4.17}$$

The equation can be reformulated:

$$\mathbf{J} \frac{d\mathbf{u}}{d\mathbf{p}} = -\frac{\partial \mathbf{r}}{\partial \mathbf{p}}\,. \tag{4.18}$$

Thus, to solve for $\frac{d\mathbf{u}}{d\mathbf{p}}$, N_p solves of the forward problem are needed, where N_p is the number of model parameters. This is equivalent to directly perturbing every input parameter. In the following, a more efficient way of computing the gradients $\frac{dF}{d\mathbf{p}}$ is presented. Therefore, Equation 4.17 is substituted into Equation 4.14:

$$\frac{dF}{d\mathbf{p}} = -\frac{\partial F}{\partial \mathbf{u}} \left(\mathbf{J}^{-1} \frac{\partial \mathbf{r}}{\partial \mathbf{p}}\right). \tag{4.19}$$

Rewriting with different bracketing yields:

$$\frac{dF}{d\mathbf{p}} = -\left(\frac{\partial F}{\partial \mathbf{u}} \mathbf{J}^{-1}\right) \frac{\partial \mathbf{r}}{\partial \mathbf{p}}\,. \tag{4.20}$$

In order to solve this, a new variable is introduced, the adjoint variable $\boldsymbol{\lambda}$:

$$\boldsymbol{\lambda}^T = \frac{\partial F}{\partial \mathbf{u}} \mathbf{J}^{-1}\,, \tag{4.21}$$

$$\mathbf{J}^{\mathbf{T}} \boldsymbol{\lambda} = \frac{\partial F}{\partial \mathbf{u}}^T\,. \tag{4.22}$$

To solve for $\boldsymbol{\lambda}$, a single linear solve with the same degrees of freedom as the forward problem is required. The actual derivatives can then be computed by substituting $\boldsymbol{\lambda}$ into Equation 4.20:

$$\frac{dF}{d\mathbf{p}} = -\boldsymbol{\lambda}^T \frac{\partial \mathbf{r}}{\partial \mathbf{p}}\,. \tag{4.23}$$

Now, an efficient method for computing $\frac{dF}{d\mathbf{p}}$ is established (e.g., Giles and Pierce, 2000; Reuber, 2021). In summary, the calculation of adjoint sensitivities involves a two-step process. First, the linear system 4.22 must be solved to get the adjoint parameter $\boldsymbol{\lambda}$. The second step involves evaluating the actual sensitivities through Equation 4.23.

In our context, the discretize-then-optimize method is chosen, as automatic differentiation allows the direct use of the forward problem and its residual equations to construct the adjoint solver. This method also guarantees the computation of exact gradients of the discretized objective function and thus facilitates debugging of the adjoint solver (Giles and Pierce, 2000). Details of the adjoint solver implementation using automatic differentiation are provided in sections 4.3.2 and 4.3.3.

4.3.2 Numerical Implementation

To compute the sensitivities, the first step involves solving the linear system introduced in Equation 4.22. With $\boldsymbol{\lambda} = (\boldsymbol{\lambda}_\mathbf{v}, \lambda_P)^\mathrm{T}$, Equation 4.22 can be separated into different blocks. To solve for $\boldsymbol{\lambda}$, a pseudo-transient approach is chosen (e.g. Kiss et al., 2023) and pseudo-time derivatives are added to the equations:

$$\frac{\partial \mathbf{R}_\mathbf{v}}{\partial \mathbf{v}}^\mathrm{T} \boldsymbol{\lambda}_\mathbf{v} + \frac{\partial R_P}{\partial \mathbf{v}}^\mathrm{T} \lambda_P - \frac{\partial F}{\partial \mathbf{v}}^\mathrm{T} = \frac{\partial \boldsymbol{\lambda}_\mathbf{v}}{\partial \phi}\,, \tag{4.24}$$

$$\frac{\partial \mathbf{R}_\mathbf{v}}{\partial P}^\mathrm{T} \boldsymbol{\lambda}_\mathbf{v} + \frac{\partial R_P}{\partial P}^\mathrm{T} \lambda_P - \frac{\partial F}{\partial P}^\mathrm{T} = \frac{\partial \lambda_P}{\partial \phi}\,. \tag{4.25}$$

A central difficulty in this context is that solving for $\boldsymbol{\lambda}$ requires the computation of the gradient terms appearing in Equations 4.24 and 4.25. Given the definition of the objective function in Equation 4.11, $\frac{\partial F}{\partial P}^\mathrm{T}$ is 0 and $\frac{\partial F}{\partial \mathbf{v}}^\mathrm{T}$ is equal to 1 at locations where the corresponding solution variable contributes to the objective function, and 0 elsewhere. The other gradient terms appearing in Equations 4.24 and 4.25 can be directly evaluated as Vector-Jacobian-Products (VJP). The evaluation of the terms including $\frac{\partial R_P}{\partial \mathbf{v}}^\mathrm{T}$, $\frac{\partial \mathbf{R}_\mathbf{v}}{\partial P}^\mathrm{T}$ and $\frac{\partial R_P}{\partial P}^\mathrm{T}$ is straightforward, since the differentiated variable appears explicitly in R_P and $\mathbf{R}_\mathbf{v}$, respectively. For the term $\frac{\partial \mathbf{R}_\mathbf{v}}{\partial \mathbf{v}}^\mathrm{T}$, the chain rule must be applied, as $\mathbf{R}_\mathbf{v}$ does not depend directly on $\mathbf{v}$. Note that the subscript v again denotes Voigt notation of the tensor.

$$\frac{\partial \mathbf{R}_\mathbf{v}}{\partial \mathbf{v}}^\mathrm{T} \boldsymbol{\lambda}_\mathbf{v} = \left(\frac{\partial \mathbf{R}_\mathbf{v}}{\partial \boldsymbol{\tau}_v}\frac{\partial \boldsymbol{\tau}_v}{\partial \dot{\boldsymbol{\varepsilon}}_v}\frac{\partial \dot{\boldsymbol{\varepsilon}}_v}{\partial \mathbf{v}}\right)^\mathrm{T} \boldsymbol{\lambda}_\mathbf{v}\,, \tag{4.26}$$

$$\frac{\partial \mathbf{R}_\mathbf{v}}{\partial \mathbf{v}}^\mathrm{T} \boldsymbol{\lambda}_\mathbf{v} = \frac{\partial \dot{\boldsymbol{\varepsilon}}_v}{\partial \mathbf{v}}^\mathrm{T} \frac{\partial \boldsymbol{\tau}_v}{\partial \dot{\boldsymbol{\varepsilon}}_v}^\mathrm{T} \frac{\partial \mathbf{R}_\mathbf{v}}{\partial \boldsymbol{\tau}_v}^\mathrm{T} \boldsymbol{\lambda}_\mathbf{v}\,. \tag{4.27}$$

Once the adjoint variables $\boldsymbol{\lambda}_\mathbf{v}$ and λ_P have been computed, the adjoint sensitivities $\frac{dF}{d\mathbf{p}}$ can be determined. This is achieved by utilizing Equation 4.23:

$$\frac{dF}{d\mathbf{p}}^\mathrm{T} = -\frac{\partial \mathbf{R}_\mathbf{v}}{\partial \mathbf{p}}^\mathrm{T} \boldsymbol{\lambda}_\mathbf{v} - \frac{\partial R_P}{\partial \mathbf{p}}^\mathrm{T} \lambda_P\,. \tag{4.28}$$

The pseudo-transient terms differ from the ones that are used in the forward solve and are summarized in Appendix 4.B. Section 4.3.4 provides details on the implementation.

4.3.3 Automatic Differentiation

In the previous section, we described the numerical implementation for computing adjoint sensitivities. To compute the adjoint variable $\boldsymbol{\lambda}$ and the sensitivities themselves, it is necessary to evaluate local VJPs of the forward functions and $\boldsymbol{\lambda}$. This section therefore explains how this can be achieved using automatic differentiation (AD). The

goal is to create a problem-agnostic adjoint solver that does not require modification when the forward solver changes.

In general, AD can be described as a technique to compute partial derivatives of a function which is evaluated by a computer program. There are two main types of AD: forward-mode and reverse-mode (e.g., Griewank and Walther, 2008; Baydin et al., 2018; Elliott, 2018). The following section outlines the concepts of both AD modes, without going into implementation details. The explanation in this section (4.3.3) follows the approach of Baydin et al. (2018), while being presented in original terms and adapted to the specific context and objectives of this chapter. For in-depth explanations of the concepts and implementation details, the reader is referred to Griewank and Walther (2008), Baydin et al. (2018) and Margossian (2019) and the references therein. In the following, an evaluation with forward-mode AD or reverse-mode AD is called forward pass and reverse pass, respectively.

In order to illustrate both forward- and reverse-mode AD, we introduce the function f: $\mathbb{R}^2 \to \mathbb{R}$:

$$f(x_1, x_2) = (x_1)^2 + ln(x_1 x_2) = y\,, \tag{4.29}$$

where x_1 and x_2 are the input variables and y is the output variable of function f. If f is differentiated with respect to x_1 and x_2 respectively, we end up with the following terms:

$$\frac{\partial f}{\partial x_1} = 2x_1 + \frac{1}{x_1}\,, \tag{4.30}$$

$$\frac{\partial f}{\partial x_2} = \frac{1}{x_2}\,. \tag{4.31}$$

To understand how these derivatives can be computed with AD, we begin by examining how such a program would evaluate the function f itself. This is illustrated in the computational graph 4.1. Here, we follow a notation which is common in AD literature (e.g., Baydin et al., 2018) and is based on Griewank and Walther (2008). In our example, v_{-1} and v_0 are the input variables, v_1 to v_3 are intermediate variables, and v_4 is the output variable.

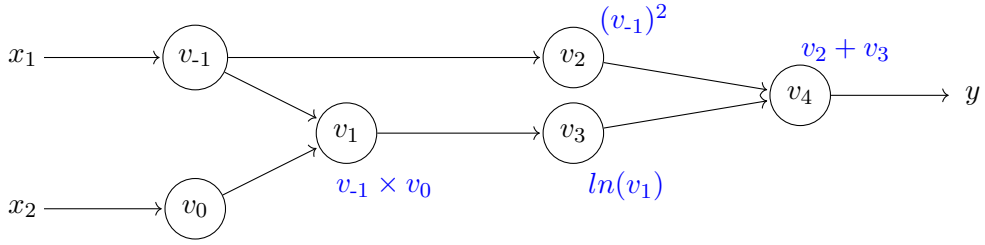

FIGURE 4.1: Computational graph for the function f. See text for explanation of v_{-1} to v_4. At each node, the operation that is used to compute the corresponding variable is indicated in blue.

f can be evaluated by successively evaluating v_1 to v_4, where v_4 yields the final result. v_1 depends on both x_1 and x_2 and needs to be computed to evaluate v_3. v_2 only depends on x_1 and is then, together with v_3, used to calculate the final result v_4.

4.3.3.1 Forward-Mode Automatic Differentiation

Forward-mode AD is based on the principle that derivatives of the intermediate variables with respect to the input variables are calculated in the same order as in the

forward solve. To explain this, we first use the chain rule for the derivative of function f with respect to the input variable x_1:

$$\frac{\partial f}{\partial x_1} = \frac{\partial v_4}{\partial v_2}\frac{\partial v_2}{\partial v_{-1}}\frac{\partial v_{-1}}{\partial x_1} + \frac{\partial v_4}{\partial v_3}\frac{\partial v_3}{\partial v_1}\frac{\partial v_1}{\partial v_{-1}}\frac{\partial v_{-1}}{\partial x_1}\,. \tag{4.32}$$

This derivative evaluated at $x_1 = 2$ and $x_2 = 4$ yields the following:

$$\frac{\partial}{\partial x_1} f(2,4) = 4.5\,. \tag{4.33}$$

Now, we want to compute this with forward-mode AD. At each intermediate variable, the derivative of this variable with respect to the input arguments is calculated. We start with $\frac{\partial v_{-1}}{\partial x_1} = 1$ and $\frac{\partial v_0}{\partial x_1} = 0$. The next step is to evaluate the derivative $\frac{\partial v_1}{\partial x_1}$:

$$\frac{\partial v_1}{\partial x_1} = \frac{\partial v_1}{\partial v_{-1}}\frac{\partial v_{-1}}{\partial x_1} + \frac{\partial v_1}{\partial v_0}\frac{\partial v_0}{\partial x_1} = v_0\frac{\partial v_{-1}}{\partial x_1} + v_{-1}\frac{\partial v_0}{\partial x_1} = 4\cdot 1 + 2\cdot 0 = 4\,. \tag{4.34}$$

In the next step, we evaluate $\frac{\partial v_2}{\partial x_1}$:

$$\frac{\partial v_2}{\partial x_1} = \frac{\partial v_2}{\partial v_{-1}}\frac{\partial v_{-1}}{\partial x_1} = 2v_{-1}\frac{\partial v_{-1}}{\partial x_1} = 2\cdot 2\cdot 1 = 4\,. \tag{4.35}$$

Now $\frac{\partial v_3}{\partial x_1}$ can be evaluated as:

$$\frac{\partial v_3}{\partial x_1} = \frac{\partial v_3}{\partial v_1}\frac{\partial v_1}{\partial x_1} = \frac{1}{v_1}\frac{\partial v_1}{\partial x_1} = \frac{1}{8}\cdot 4 = 0.5\,. \tag{4.36}$$

Finally, the derivative $\frac{\partial v_4}{\partial x_1}$ can be computed:

$$\frac{\partial v_4}{\partial x_1} = \frac{\partial v_4}{\partial v_2}\frac{\partial v_2}{\partial x_1} + \frac{\partial v_4}{\partial v_3}\frac{\partial v_3}{\partial x_1} = 1\cdot 4 + 1\cdot 0.5 = 4.5\,. \tag{4.37}$$

In summary, we saw that forward-mode AD calculates the derivatives in the same order as the function is evaluated. Therefore, the evaluation of the function and the derivative can be performed while evaluating the function. However, to evaluate the second partial derivative $\frac{\partial f}{\partial x_2}$, another forward mode evaluation with $\frac{\partial v_{-1}}{\partial x_2} = 0$ and $\frac{\partial v_0}{\partial x_2} = 1$ must be computed.

4.3.3.2 Reverse-Mode Automatic Differentiation

In reverse-mode AD, the chain rule is applied in reverse order to compute the partial derivatives. Therefore, the derivatives of the function output with respect to the intermediate variables are calculated successively. This is again illustrated with the partial derivative $\frac{\partial f}{\partial x_1}$. This time, we first set the derivative $\frac{\partial y}{\partial v_4}$ to 1. Next, $\frac{\partial y}{\partial v_2}$ and $\frac{\partial y}{\partial v_3}$ are calculated:

$$\frac{\partial y}{\partial v_2} = \frac{\partial y}{\partial v_4}\frac{\partial v_4}{\partial v_2} = 1\cdot 1 = 1\,, \tag{4.38}$$

$$\frac{\partial y}{\partial v_3} = \frac{\partial y}{\partial v_4}\frac{\partial v_4}{\partial v_3} = 1\cdot 1 = 1\,. \tag{4.39}$$

Then, $\frac{\partial y}{\partial v_1}$ can be determined:

$$\frac{\partial y}{\partial v_1} = \frac{\partial y}{\partial v_3}\frac{\partial v_3}{\partial v_1} = \frac{\partial y}{\partial v_3} \cdot \frac{1}{v_1} = 1 \cdot \frac{1}{8} = \frac{1}{8}\,. \tag{4.40}$$

Finally, $\frac{\partial y}{\partial v_{-1}}$ can be evaluated, in this case, the contributions of v_2 and v_1 are added:

$$\frac{\partial y}{\partial v_{-1}} = \frac{\partial y}{\partial v_1}\frac{\partial v_1}{\partial v_{-1}} + \frac{\partial y}{\partial v_2}\frac{\partial v_2}{\partial v_{-1}} = \frac{\partial y}{\partial v_1} \cdot v_0 + \frac{\partial y}{\partial v_2} \cdot 2v_{-1} = \frac{1}{8} \cdot 4 + 1 \cdot 4 = 4.5\,. \tag{4.41}$$

Additionally, the derivative to the second input argument x_2 can be calculated $\frac{\partial y}{\partial v_0}$:

$$\frac{\partial y}{\partial v_0} = \frac{\partial y}{\partial v_1}\frac{\partial v_1}{\partial v_0} = \frac{\partial y}{\partial v_1} \cdot v_{-1} = \frac{1}{8} \cdot 2 = \frac{1}{4}\,. \tag{4.42}$$

As demonstrated here, in reverse-mode AD, the partial derivatives of both input arguments could be calculated in one reverse pass. In contrast to the forward pass, first the function must be evaluated, and then reverse-mode AD calculates the derivatives in the opposite direction.

4.3.3.3 Generalization

By comparing both methods, it becomes apparent that, for our scalar-valued function f with two inputs, both partial derivatives can be computed in a single reverse pass. In contrast, forward-mode AD requires a separate forward pass for each partial derivative.

These methods can be generalized to functions $f : \mathbb{R}^n \to \mathbb{R}^m$ (e.g., Baydin et al., 2018; Hill and Dalle, 2025). In such cases, one can compute the full Jacobian matrix $\mathbf{J} \in \mathbb{R}^{m \times n}$, which can be written as follows:

$$\mathbf{J} = \begin{bmatrix} \frac{\partial y_1}{\partial x_1} & \cdots & \frac{\partial y_1}{\partial x_n} \\ \vdots & \ddots & \vdots \\ \frac{\partial y_m}{\partial x_1} & \cdots & \frac{\partial y_m}{\partial x_n} \end{bmatrix}. \tag{4.43}$$

In every forward pass, one column of the Jacobian $\mathbf{J}$ can be computed. For the i-th column, this can also be seen as a Jacobian-Vector-Product (JVP) of $\mathbf{J}$ with the column vector $\mathbf{e}_i$, with $\mathbf{e}_i$ as the i-th unit vector. More generally, the JVP can also be evaluated with an arbitrary column vector $\mathbf{a} \in \mathbb{R}^n$ (Baydin et al., 2018). In that case, a forward pass directly computes the following JVP:

$$\mathbf{J}\ \mathbf{a} = \begin{bmatrix} \frac{\partial y_1}{\partial x_1} & \cdots & \frac{\partial y_1}{\partial x_n} \\ \vdots & \ddots & \vdots \\ \frac{\partial y_m}{\partial x_1} & \cdots & \frac{\partial y_m}{\partial x_n} \end{bmatrix} \begin{bmatrix} a_1 \\ \vdots \\ a_n \end{bmatrix}. \tag{4.44}$$

Similarly, one row of $\mathbf{J}$ can be computed with a single reverse-mode AD evaluation, as this corresponds to evaluating a scalar-valued function with n input variables. For the i-th row, this corresponds to the Vector–Jacobian Product (VJP) of the row vector $\mathbf{e}_i{}^{\mathrm{T}}$ with the Jacobian $\mathbf{J}$.

In the general case, a VJP with an arbitrary vector $\mathbf{b}^\top \in \mathbb{R}^{1\times m}$ can be evaluated with one reverse pass (Baydin et al., 2018):

$$\mathbf{b}^\top \mathbf{J} = \begin{bmatrix} b_1 & \cdots & b_m \end{bmatrix} \begin{bmatrix} \frac{\partial y_1}{\partial x_1} & \cdots & \frac{\partial y_1}{\partial x_n} \\ \vdots & \ddots & \vdots \\ \frac{\partial y_m}{\partial x_1} & \cdots & \frac{\partial y_m}{\partial x_n} \end{bmatrix} . \tag{4.45}$$

Note that $(\mathbf{b}^\top \mathbf{J})^T = \mathbf{J}^\top \mathbf{b}$ is also referred to as a VJP. Reverse-mode AD can therefore be used to evaluate the expressions in Equations 4.24 and 4.25 and when evaluating the sensitivities with Equation 4.28.

In summary, when computing the full Jacobian of a function $f : \mathbb{R}^n \to \mathbb{R}^m$, reverse-mode AD is more efficient if $m < n$, whereas forward-mode AD is more efficient if $m > n$ (e.g., Margossian, 2019). The effective implementation requires $m << n$ for reverse-mode to be more efficient (e.g., Baydin et al., 2018; Margossian, 2019). In many cases, one is not interested in materializing the entire Jacobian but instead in directly evaluating a JVP or VJP without explicitly storing the full Jacobian. In such cases, forward-mode AD can be used to compute the JVP, while reverse-mode AD is suited for evaluating the VJP. Thus, AD can also be seen as an operator for directly computing JVPs and VJPs, respectively (e.g., Blondel and Roulet, 2024; Hill et al., 2025; Hill and Dalle, 2025).

4.3.4 Use of Automatic Differentiation for Adjoint Solver

The capabilities of AD methods are now used to construct a problem-agnostic adjoint solver. In Equations 4.24 and 4.25, we need to evaluate local VJPs to solve for the adjoint variable $\boldsymbol{\lambda}$. As discussed in the previous chapter, this operation is naturally performed by reverse-mode AD. To achieve this within the Julia-based code of JustRelax.jl, the package Enzyme.jl is used (Moses and Churavy, 2020, Moses et al., 2021). Enzyme.jl supports both forward- and reverse-mode AD on CPUs and GPUs. In the following, it is demonstrated how Enzyme.jl can be used to evaluate a VJP using reverse-mode AD. To illustrate this, the following function $h : \mathbb{R}^2 \to \mathbb{R}^2$ is introduced:

$$h(x_1, x_2) = \begin{bmatrix} y_1 \\ y_2 \end{bmatrix} = \begin{bmatrix} x_1^2 - x_1 x_2 \\ 5x_1 \end{bmatrix} . \tag{4.46}$$

The Jacobian $\mathbf{J}_h$ of function h reads:

$$\mathbf{J}_h(x_1, x_2) = \begin{bmatrix} 2x_1 - x_2 & -x_1 \\ 5 & 0\,. \end{bmatrix} . \tag{4.47}$$

Suppose $x_1 = 4$ and $x_2 = 3$, and we want to compute the VJP with the vector $\mathbf{a} = (2, 3)^{\mathrm{T}}$:

$$\mathbf{a}^{\mathrm{T}} \mathbf{J}_h(4, 3) = \begin{bmatrix} 2 & 3 \end{bmatrix} \begin{bmatrix} 2 \cdot 4 - 3 & -4 \\ 5 & 0 \end{bmatrix} = \begin{bmatrix} 25 & -8 \end{bmatrix} . \tag{4.48}$$

Algorithm 2 provides an example of how to use Enzyme.jl to perform reverse-mode AD. Line 4 introduces the function h, followed by the initialization of the required variables. x holds the input, y is initialized to store the result of h, bx is initialized to store the result of the VJP evaluation and by is initialized with the values of $\mathbf{a}$. The VJP of $\mathbf{a}$ and $\mathbf{J}_h$ is computed using the function "Enzyme.autodiff()". The first

Algorithm 2 : Julia code example: Computation of a VJP using reverse-mode AD with Enzyme.jl.

```
1 using Enzyme # Load package (Enzyme.jl version 0.13.50)
2
3 # Define function h
4 function h(y,x)
5     y[1] = x[1] * x[1] - x[2] * x[1]
6     y[2] = 5*x[1]
7     return nothing
8 end
9
10 # Initialization
11 x  = [4.0, 3.0] # Initial values of x
12 bx = [0.0, 0.0] # Initialize to store the result of the VJP
13 y  = [0.0, 0.0] # Initialize to store result of h
14 by = [2.0, 3.0] # Entries of a-vector
15
16 # Perform reverse mode automatic differentiation
17 Enzyme.autodiff(Reverse, h, Duplicated(y,by), Duplicated(x,bx))
18 # y  = [4.0, 20.0] and bx = [25.0,-8.0]
```

argument "Reverse" specifies that reverse-mode AD is used. The second argument is the function, h. The third argument holds y and dy, and the fourth argument holds x and dx. The last two arguments are forwarded within an object called "Duplicated". If the function y has already been evaluated beforehand, "DuplicatedNoNeed" can be used, because then, the function itself is not evaluated anymore. After executing the Enzyme function, the result of h is stored in y, and the result of the VJP is stored in bx. If by is set to $[1.0, 0.0]$, the partial derivatives of y_1 with respect to x_1 and x_2 are computed. Similarly, setting $by = [0.0, 1.0]$ yields the partial derivatives of y_2. Note that with "Duplicated" and "DuplicatedNoNeed", the results are accumulated. This accumulation can be used if the VJP needs to be propagated through multiple functions (see Equation 4.27). This is used extensively in the adjoint solver, as shown in the next paragraph.

The functionality of Enzyme described above is used to numerically solve the adjoint problem introduced in Section 4.3.2. The following describes how the residuals of Equations 4.24 and 4.25 can be evaluated using AD. Instead of using the function "Enzyme.autodiff()", the function "Enzyme.autodiff_deferred()" is employed, as it also supports GPU execution. A pseudocode implementation of the adjoint solver is provided in Algorithm 3, where the term "Reverse()" denotes a call to "Enzyme.autodiff_deferred()". The pseudocode illustrates the computation of the adjoint variables $\boldsymbol{\lambda}_{\mathbf{v}}$ and λ_P, followed by the evaluation of the adjoint sensitivities $\frac{dF}{d\mathbf{p}}$.

First, the structure of the pseudo-transient iteration loop is presented. Within this loop, the residuals of Equations 4.24 and 4.25 are evaluated and stored in the variables $\bar{\mathbf{v}} = (\bar{v}_x, \bar{v}_z)^{\mathrm{T}}$ and $\bar{P}$, respectively. In line 2, these variables are initialized, after which the contributions of the terms $-\frac{\partial F}{\partial \mathbf{v}}^{\mathrm{T}}$ and $-\frac{\partial F}{\partial P}^{\mathrm{T}}$ are added.

Algorithm 3 : Pseudocode implementation of the adjoint solver using the pseudo-transient method and automatic-differentiation. The code shows the pseudo-transient iteration loop and the evaluation the adjoint sensitivities.

Data : Solution of the Forward Solve + Material Parameters
Result : Adjoints Variables $\boldsymbol{\lambda}_\mathbf{v}$ and λ_P + Adjoint Sensitivities $\frac{d\mathcal{F}}{d\mathbf{p}}$

`# Pseudo-Transient Iteration Loop`

1 **while** *error* $>$ *tolerance* **do**
2 $\quad \bar{v}_x = 0;\ \bar{v}_z = -s;\ \bar{P} = 0$
3 $\quad$ Reverse($\mathbf{R}_\mathbf{v}$): $d\boldsymbol{\tau}_v = \frac{\partial \mathbf{R}_\mathbf{v}}{\partial \boldsymbol{\tau}_v}^\mathrm{T} \boldsymbol{\lambda}_\mathbf{v}$ and $\bar{P}$ += $\frac{\partial \mathbf{R}_\mathbf{v}}{\partial P}^\mathrm{T} \boldsymbol{\lambda}_\mathbf{v}$
4 $\quad$ Reverse($\boldsymbol{\tau}_v$): $d\dot{\boldsymbol{\varepsilon}}_v = \frac{\partial \boldsymbol{\tau}_v}{\partial \dot{\boldsymbol{\varepsilon}}_v}^\mathrm{T} d\boldsymbol{\tau}_v$
5 $\quad$ Reverse(R_P): $\bar{P}$ += $\frac{\partial R_P}{\partial P}^\mathrm{T} \lambda_P$ and $\bar{\mathbf{v}}$ += $\frac{\partial R_P}{\partial \mathbf{v}}^\mathrm{T} \lambda_P$
6 $\quad$ update λ_P with $\bar{P}$
7 $\quad$ Reverse($\dot{\boldsymbol{\varepsilon}}_v$): $\bar{\mathbf{v}}$ += $\frac{\partial \dot{\boldsymbol{\varepsilon}}_v}{\partial \mathbf{v}}^\mathrm{T} d\dot{\boldsymbol{\varepsilon}}_v$
8 $\quad$ update $\boldsymbol{\lambda}_\mathbf{v}$ with $\bar{\mathbf{v}}$

`# Calculate Adjoint Sensitivities`

9 Reverse($\mathbf{R}_\mathbf{v}$): $d\boldsymbol{\tau}_v = -\frac{\partial \mathbf{R}_\mathbf{v}}{\partial \boldsymbol{\tau}_v}^\mathrm{T} \boldsymbol{\lambda}_\mathbf{v}$ and $\frac{dF}{d\rho}^\mathrm{T} = -\frac{\partial \mathbf{R}_\mathbf{v}}{\partial \rho}^\mathrm{T} \boldsymbol{\lambda}_\mathbf{v}$
10 Reverse($\boldsymbol{\tau}_v^n$): $\frac{dF}{d\eta}^\mathrm{T} = -\frac{\partial \boldsymbol{\tau}_v}{\partial \eta}^\mathrm{T} d\boldsymbol{\tau}_v$ and $\frac{dF}{dG}^\mathrm{T} = -\frac{\partial \boldsymbol{\tau}_v}{\partial G}^\mathrm{T} d\boldsymbol{\tau}_v$
11 Reverse(R_P): $\frac{dF}{dK}^\mathrm{T} = -\frac{\partial R_P}{\partial K}^\mathrm{T} \lambda_P$

Since neither v_x nor P are part of the objective function F, these terms vanish, and $\bar{v}_x$ and $\bar{P}$ are therefore initialized to zero. The variable v_z is part of F at selected nodes defined by s and is therefore initialized with -1 at these nodes. The array s specifies the locations where v_z contributes to the objective function. Note that if all v_z velocities in the numerical domain were included in F, the entire vector $\bar{v}_z$ would be initialized with -1.

In line 3, the function $\mathbf{R}_\mathbf{v}$ is differentiated with respect to $\boldsymbol{\tau}_v$ and P, and a VJP with $\boldsymbol{\lambda}_\mathbf{v}$ is calculated and then saved in the intermediate variable $d\boldsymbol{\tau}_v$. $\frac{\partial \mathbf{R}_\mathbf{v}}{\partial P}^\mathrm{T} \boldsymbol{\lambda}_\mathbf{v}$ is calculated and added to $\bar{P}$. Next, the function that calculates $\boldsymbol{\tau}_v$ is differentiated. $\boldsymbol{\tau}_v$ is differentiated with respect to $\dot{\boldsymbol{\varepsilon}}_v$, and the VJP with the previously computed $d\boldsymbol{\tau}_v$ is calculated. This interim result is stored in the variable $d\dot{\boldsymbol{\varepsilon}}_v$. In line 5, the residual function R_P is differentiated, so that both $\bar{P}$ and $\bar{\mathbf{v}}$ can be updated. With that, the complete residual of Equation 4.25 is evaluated and therefore λ_P can be updated. To update $\boldsymbol{\lambda}\mathbf{v}$, the strain-rate function still needs to be differentiated. This finally completes the computation of the term $\frac{\partial \mathbf{R}_\mathbf{v}}{\partial \mathbf{v}}^\mathrm{T} \boldsymbol{\lambda}\mathbf{v}$, so that this last missing term is added to $\bar{\mathbf{v}}$, and $\boldsymbol{\lambda}\mathbf{v}$ is updated in line 8.

After the calculation of the adjoint variables, the sensitivities can be evaluated. In this step, the functions of the forward solver are differentiated with respect to the material parameters for which the sensitivities should be computed. For instance, to compute $\frac{dF}{d\rho}$, the residual function $\mathbf{R}_\mathbf{v}$ is differentiated with respect to ρ and a VJP with $\boldsymbol{\lambda}_\mathbf{v}$ is computed (see line 9). The remaining sensitivities with respect to η, G, and K are evaluated in an analogous manner based on Equation 4.28 (see lines 9 to 12).

4.4 Benchmarking: Gradient Test

To benchmark the adjoint sensitivities, we perform a gradient test (e.g., Navon et al., 1992; Honnorat et al., 2007; Martin and Monnier, 2014). A similar procedure, the

Taylor test, can also be used to verify the adjoint sensitivities (e.g., Charpentier and Ghemires, 2000; Petit et al., 2025), which involves performing a Taylor expansion of F. In the gradient test, the adjoint sensitivities of F with respect to $\mathbf{p}$ are compared to a finite-difference approximation using a first-order scheme:

$$\frac{F(\mathbf{p}+\alpha\delta\mathbf{m})-F(\mathbf{p})}{\alpha}=\frac{\partial F}{\partial \mathbf{p}}\cdot\delta\mathbf{m}+\mathcal{O}(\alpha)\,, \tag{4.49}$$

where α is a small positive value and $\delta\mathbf{m}$ is a perturbation matrix containing random numbers with an euclidean norm of 1. Now we can evaluate the following expression:

$$\mathcal{D}_\alpha=\left|\frac{F(\mathbf{p}+\alpha\delta\mathbf{m})-F(\mathbf{p})}{\alpha\left(\frac{\partial F}{\partial \mathbf{p}}\cdot\delta\mathbf{m}\right)}-1\right| \tag{4.50}$$

According to Equation 4.49, $\lim_{\alpha\to 0}\mathcal{D}_\alpha=0$ holds (Martin and Monnier, 2014). $F(\mathbf{p}+\alpha\delta\mathbf{m})$ requires an evaluation of the forward problem for every α value, $F(\mathbf{p})$ only needs to be evaluated once. The term $\frac{\partial F}{\partial \mathbf{p}}$ corresponds to the adjoint sensitivities. To validate the adjoint sensitivities, the term $\mathcal{D}_\alpha$, should decrease proportionally to α as α decreases. For benchmarking, a pure shear test case is considered, verifying sensitivities with respect to η, G, and K.

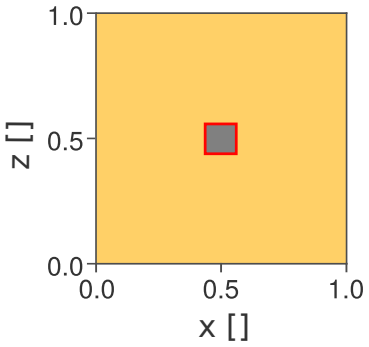

FIGURE 4.2: Initial setup of the pure shear test: yellow represents the matrix, grey the block and red contours indicate the region contributing to the objective function.

TABLE 4.1: Material parameters for pure shear test.

	Matrix	**Block**
η	1.0	1.0
G	1.0	0.5
K	3.0	1.5

4.4.1 Pure Shear Benchmark

Figure 4.2 shows the initial setup of the pure shear benchmark test. The initial setup consists of a homogeneous matrix with a centered block. The domain measures 1 in each direction, and the block has an edge length of 0.2. The objective function F sums the v_z velocities within the block, which is outlined by the red line in Figure 4.2. The numerical resolution is 64 cells in each direction.

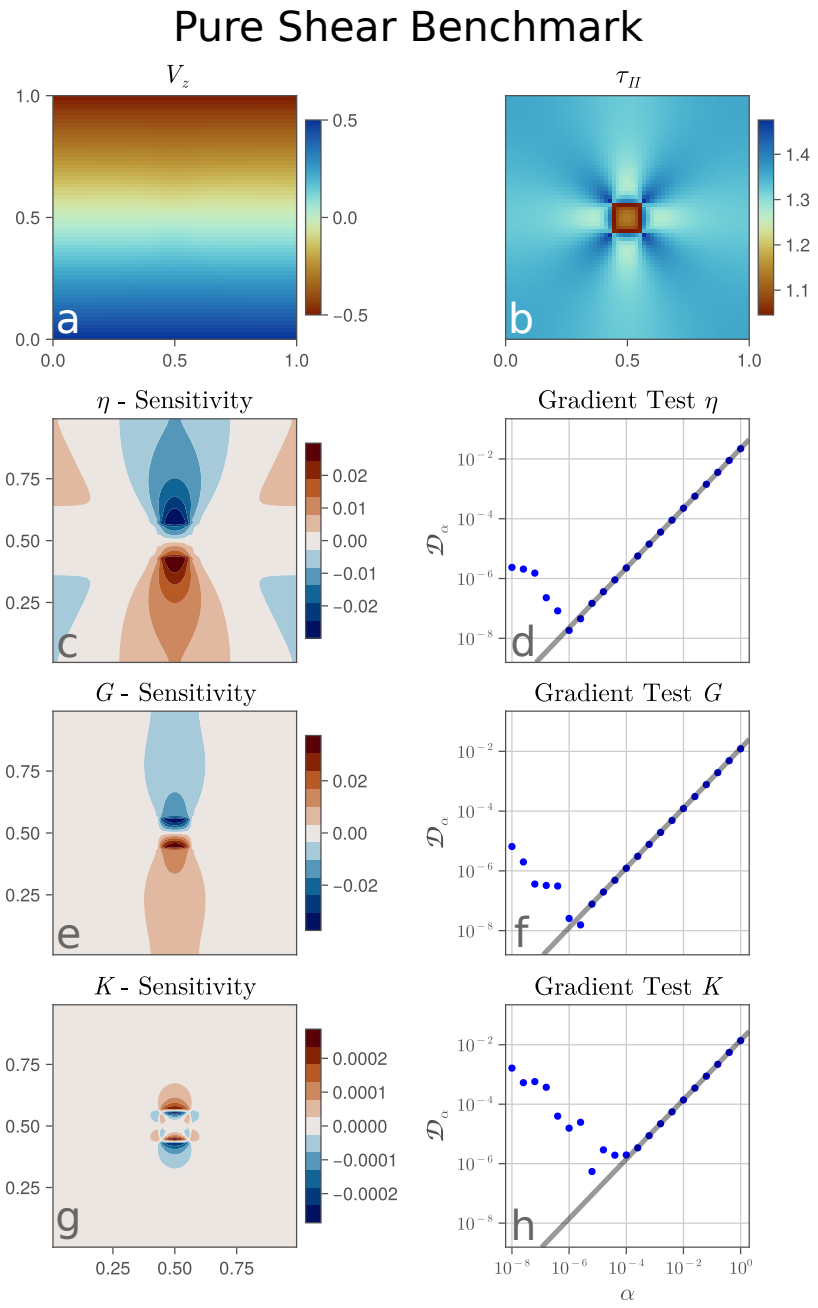

FIGURE 4.3: Gradient test for the pure Shear setup. (a) and (b) show the vertical velocity v_z and the second invariant of the stress, respectively. (c), (e) and (g) show the results of the adjoint sensitivities for η, G, and K, respectively. Adjacent to these, (d), (f) and (h) present the results of the gradient test for η, G, and K, shown as blue dots. The grey line in (d), (f) and (h) represents α plotted against α.

The material parameters used for the pure shear test are listed in Table 4.1. Gravity is set to 0 in every direction. The compressible Stokes equations are solved with a $K = 3.0$ in the matrix and 1.5 in the block. The viscosity η is 1, both in the matrix and block and G is 1 in the matrix and 0.5 in the block. Velocities normal to the boundaries are prescribed as boundary conditions. At the left boundary, $v_x = -0.5$, at the right boundary $v_x = 0.5$, at the bottom boundary $v_z = 0.5$ and at the top boundary $v_z = -0.5$. Both the forward and adjoint solvers use an absolute tolerance of 10^{-15}. Figure 4.3 shows the results of the forward run, the sensitivities with respect

to η, G, and K and the corresponding gradient tests. The adjoint sensitivities are verified by the gradient test, as the truncation error decreases at a rate of α (see Figure 4.3 d,f and h). These tests also verify the sensitivities with respect to the density ρ, since in examples including gravity, the ρ sensitivities are equal to the adjoint variable λ_{v_z} scaled by the gravitational acceleration.

4.5 Sensitivity Analysis

In the following, adjoint sensitivities are analyzed, and it is shown how they can be scaled to allow comparison across different parameters for linear models and small parameter perturbations. To this end, it is necessary to specify the objective function F for which the sensitivities are evaluated. As described in Section 4.3.1, the objective function considered here is the sum of vertical velocities within a defined area. The locations contributing to the objective function are hereafter referred to as observation points. This section discusses how adjoint sensitivities can be used to investigate physical processes. First, a simple setup is considered in which a plume head rises through the asthenosphere. The second example shows a nonlinear 2D subduction zone, where the influence of slab pull and ridge push on the horizontal plate motion is investigated with adjoint sensitivities.

4.5.1 Rising Plume Head

4.5.1.1 Setup

The plume head is characterized by lower density and viscosity relative to the surrounding asthenosphere. In the first part, we focus on the rising velocities of the plume head, while in the second part, we identify the key parameters controlling crustal uplift above the plume in the asthenosphere. The extent and geometry of the initial setup is show in Figure 4.4.

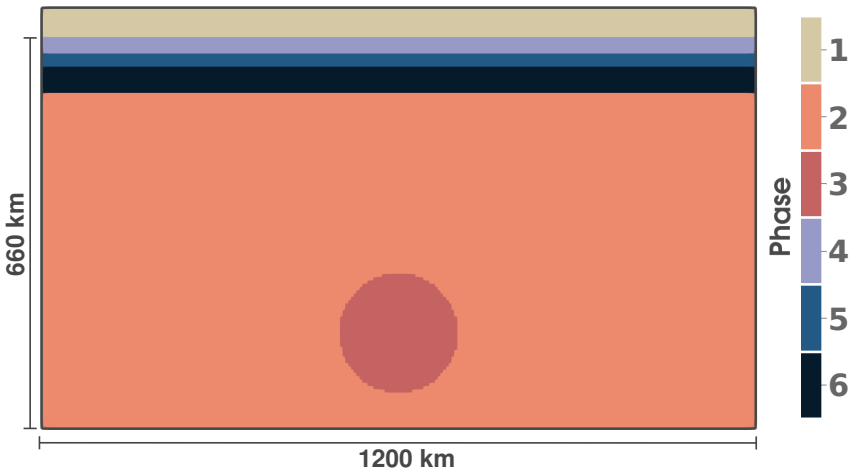

FIGURE 4.4: Initial setup of the rising plume head example. The model comprises six phases, extending 1200 km in the x-direction and 710 km in the z-direction. The upper 50 km consist of a sticky-air layer, defined as phase 1.

The setup comprises six phases: the asthenosphere and plume head, a lithosphere divided into lithospheric mantle, lower crust and upper crust and a sticky-air layer on top of the crust. Values for viscosity η and density ρ are presented in Table 4.4. The shear modulus G is $4 \cdot 10^{10}$ Pa and the bulk modulus is $6.7 \cdot 10^{10}$ Pa. The numerical

resolution is 256 and 128 in the x- and z-directions, respectively and the absolute tolerance is 10^{-8} for both the forward and adjoint solves.

TABLE 4.2: Material parameters of viscosity η and density ρ for the six phases in the plume head example.

Phase	η [Pas]	ρ [kg/m^3]
1	10^{19}	10
2	$5 \cdot 10^{20}$	3300
3	10^{20}	3280
4	$7 \cdot 10^{22}$	2900
5	$1.5 \cdot 10^{23}$	3365
6	$3 \cdot 10^{21}$	3365

4.5.1.2 Simulation Results

Figure 4.5 shows the results of the plume head simulation over a time of 15 Myr. As shown in the first column, the plume head rises vertically through the asthenosphere and flattens when reaching the lithosphere base.

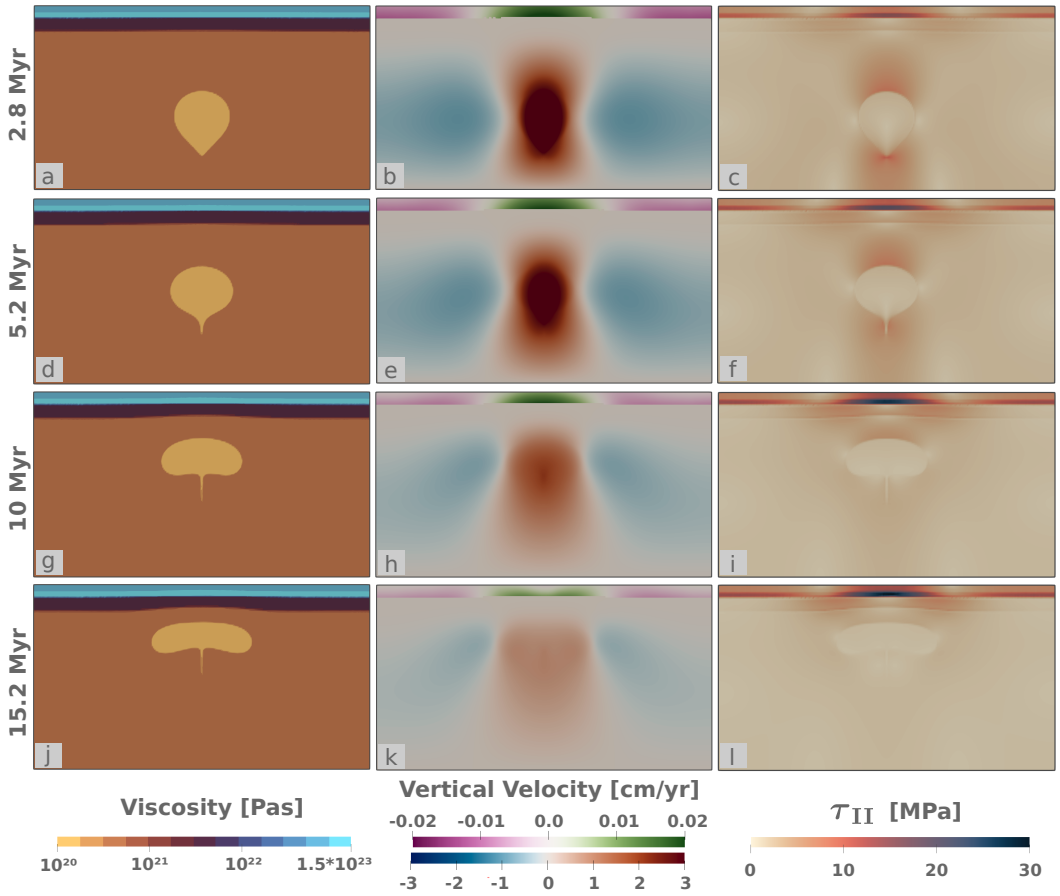

FIGURE 4.5: Results of the plume head simulations at different timesteps. The first row corresponds to 2.8 Myr, the second to 5.2 Myr, the third to 10 Myr, and the last to 15.2 Myr. The first column shows the phase distribution, the second the velocities in the asthenosphere and lithosphere (with separate colorbars for each) and the third the distribution of the second invariant of the stress tensor.

The lower lithosphere appears noticeably deformed, while the displacement is only slightly transmitted to the crust. This is also evident in the vertical velocities. The second column shows the vertical velocity in the asthenosphere and, using a separate colorbar, the vertical velocity in the crust. This distinction is essential, as we later examine both crustal uplift and the plume head's ascent. In the asthenosphere, the plume head initially rises at about 3 cm/yr, slowing as it ascends. Crustal velocities peak when plume velocities are highest, reaching approximately 0.02 cm/yr. The third column shows the stress distribution, expressed by the second invariant of the stress tensor. In the asthenosphere, stresses are highest above and below the plume, while in the crust they increase steadily as the plume ascends, producing a pronounced stress anomaly in the lower crust at 15 Myr.

4.5.1.3 Sensitivity Results

In this section, we compute adjoint sensitivities using observation points corresponding to plume phase 3, such that the objective function sums the vertical velocity v_z within the plume. Thus, these sensitivities reveal the parameters that exert the greatest control on the plume head's vertical velocity. Figure 4.6 shows the sensitivities of viscosity and density, as well as of the shear and bulk modulus. These sensitivities indicate, for each parameter, the regions that most strongly influence the plume head's vertical velocity when the respective parameter is perturbed. We first examine the sensitivities with respect to viscosity. Early in the simulation, the viscosity inside, below and above the plume primarily controls the rising velocity (Figure 4.6a,e).

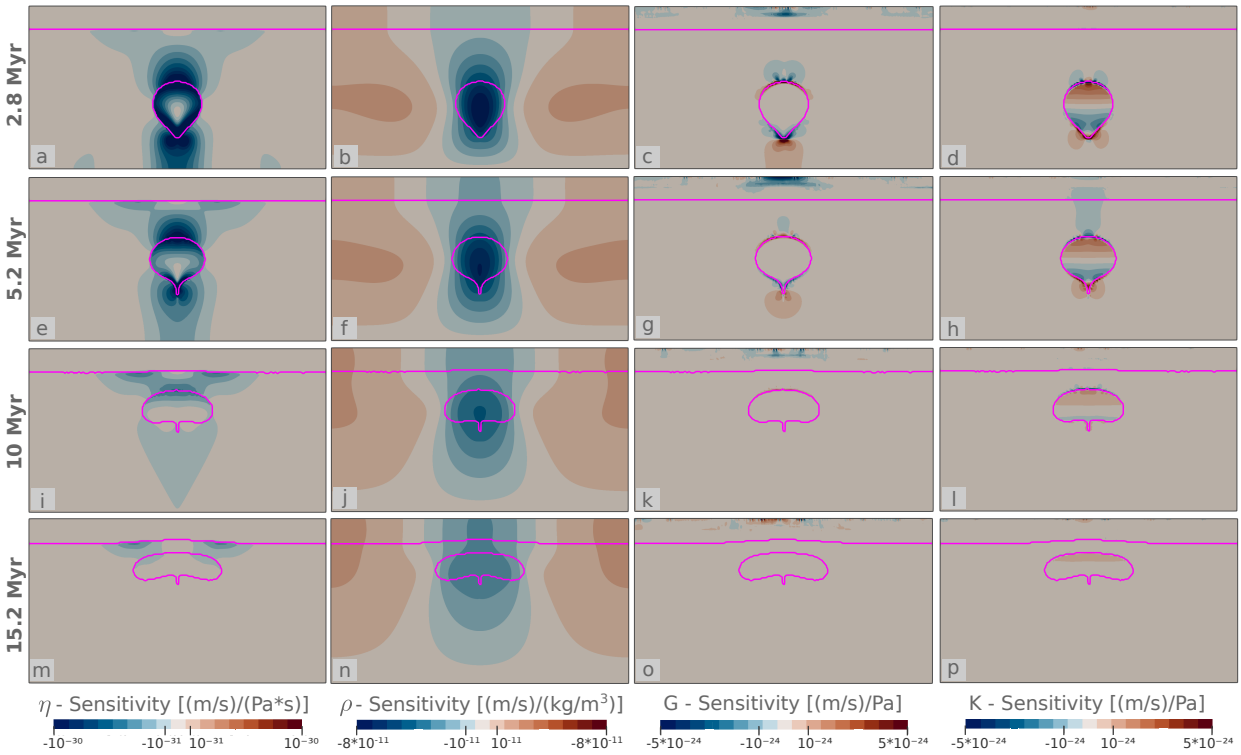

FIGURE 4.6: Sensitivities of the plume head simulation. Rows correspond to different timesteps and columns (from left to right) show sensitivities to viscosity η, density ρ, shear modulus G, and bulk modulus K. The pink contour marks the plume outline in the asthenosphere and the boundary between the asthenosphere and lithosphere phases.

Between 10 and 15 Myr, as the plume flattens, the strongest sensitivities occur in the region between the plume and the lithosphere. These appear as negative anomalies, indicating that increasing viscosity reduces the plume head's ascent velocity. For density, the spatial pattern remains stable throughout the simulation, while the sensitivity magnitude decreases toward the end. Inside the plume, as well as above and below it, the density sensitivity is strongly negative, peaking within the plume. A reduction in plume density therefore strongly increases its ascent velocity. In contrast, to the left and right of the plume, the sensitivities are positive.

The sensitivity patterns of the shear and bulk modulus differ from those described above. Between 2 and 5 Myr, the shear modulus sensitivity shows a positive anomaly below the plume head and a negative one above it. The bulk modulus sensitivity is particularly high in the upper half of the plume and reduced in the lower half. The strongest anomalies generally occur at the plume–asthenosphere interface. In the crust, the pattern is more complex. In particular, the shear modulus shows a negative anomaly of similar magnitude to that in the asthenosphere. In both cases, the sensitivity values decrease as the simulation progresses.

4.5.1.4 Scaling of Adjoint Sensitivities

So far, sensitivity values of different parameters cannot be directly compared, as they have different units and magnitudes. In the following, we want to know how much the objective function changes percentagewise, if a specific parameter is changed by a small percentage. To this end, we scale the sensitivities, following the approach outlined in, for instance, Saltelli et al. (2000), Borgonovo and Peccati (2004), and Reuber et al. (2018):

$$\left(\frac{dF}{dp_i}\right)_{\mathrm{s}} = \frac{dF}{dp_i}\frac{p_i}{F}\,, \tag{4.51}$$

where $\frac{dF}{dp_i}$ is the sensitivity of parameter p_i, $\left(\frac{dF}{dp_i}\right)_{\mathrm{s}}$ is the scaled sensitivity and F the evaluation of the objective function. This method generally belongs to local sensitivity analysis (e.g., Saltelli et al., 2000; Borgonovo and Plischke, 2016).

To compare the scaled sensitivities over time, the maximum scaled sensitivity per parameter is plotted over time in Figure 4.7. The sensitivities of the shear and bulk modulus have a magnitude of 10^{-6} and therefore have little influence on the objective function. In contrast, the viscosity and density sensitivities are three to five orders of magnitude higher. The density sensitivity is consistently larger than the viscosity sensitivity, with values around 10^{-1}. As the absolute density sensitivities across the model domain are consistently high (Figure 4.6), the density can be considered the most influential parameter for the rising velocity.

In addition to that, the spatial sensitivities can be summed per phase, so that the overall influence of a whole phase on the objective function can be investigated. The summed sensitivities at 2.8 Myr are presented in Table 4.3. It can be seen that the smallest values correspond to the sticky air, which exhibits the lowest sensitivities for every parameter. The summed sensitivities for K and G are also negligible compared to those of ρ and η.

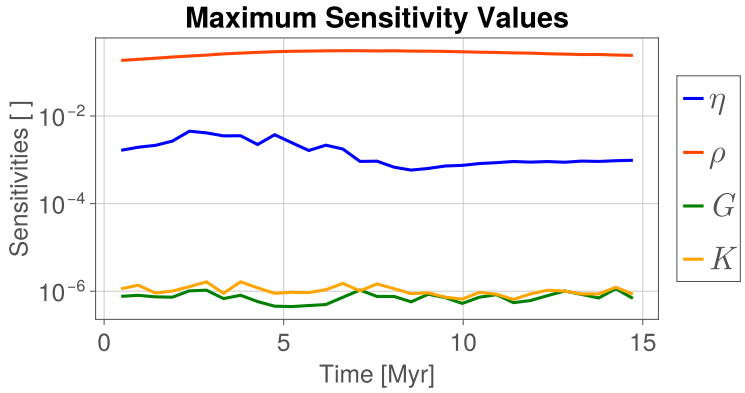

FIGURE 4.7: Scaled sensitivities for the rising plume head. Results are shown for 15 Myr. For each timestep, the maximum absolute sensitivity value of each parameter across the numerical domain is plotted.

TABLE 4.3: Scaled sensitivities summed over each phase for the plume head simulation at 2.8 Myr.

Phase	η	ρ	G	K
1	$3.1 \cdot 10^{-4}$	$-4.8 \cdot 10^{-4}$	$6.3 \cdot 10^{-10}$	$-1.0 \cdot 10^{-7}$
2	-0.89	164.5	$-1.5 \cdot 10^{-6}$	$-3.4 \cdot 10^{-6}$
3	$-9.2 \cdot 10^{-2}$	-179.3	$4.5 \cdot 10^{-6}$	$-6.3 \cdot 10^{-6}$
4	$-2.6 \cdot 10^{-3}$	-0.2	$-1.5 \cdot 10^{-5}$	$-3.0 \cdot 10^{-6}$
5	$2.6 \cdot 10^{-3}$	-0.2	$-1.2 \cdot 10^{-5}$	$-2.8 \cdot 10^{-6}$
6	$-1.5 \cdot 10^{-2}$	-0.6	$-3.8 \cdot 10^{-6}$	$-5.1 \cdot 10^{-6}$

Examining the values for ρ and η reveals that the most influential parameters are the density of the mantle and the plume. Increasing the density of the asthenosphere (phase 2) by 0.1% and therefore 3.3 kg/m^3 increases the ascent velocity of the plume by around 16 %. However, increasing the density of the plume (phase 3) by the same amount reduces the ascent velocity of the plume by around 18 %.

4.5.2 2D Subduction Zone

In this section, a 2D converging subduction zone is investigated. The incompressible Stokes equations are solved, so that the velocity field is divergence-free. A visco-elastic rheology is considered, with mantle viscosity governed by a combination of diffusion and dislocation creep processes:

$$\eta_{\text{eff}} = \left(\frac{1}{\eta_{\text{dis}}} + \frac{1}{\eta_{\text{dif}}} \right)^{-1}, \tag{4.52}$$

$$\eta_{\text{c}} = (F A_c)^{-\frac{1}{n_c}} d^{-\frac{p_c}{n_c}} (\dot{\varepsilon}_{\text{II}})^{\frac{1}{n_c}-1} f^{-\frac{r}{n_c}} \exp\left(\frac{E_c + P\, V_c}{n_c\, R\, T} \right), \tag{4.53}$$

$$F = 2^{n-1} 3^{\frac{n+1}{2}}, \tag{4.54}$$

where η_{eff} is the effective viscosity, η_{dis} and η_{dif} are the dislocation and diffusion creep viscosities, respectively and c represents either c = dis or c = dif. A are experimental constants for dislocation and diffusion creep, respectively. f denotes the water fugacity with exponent r. d is the grain size with exponent p. E and V are the activation

energy and activation volume, respectively. n is the stress exponent for dislocation creep, R the universal gas constant, and T and P the temperature and pressure. F is a prefactor that scales the experimental data from axial compression experiments to invariant form. The density depends on temperature as follows:

$$\rho = \rho_0 \cdot (1 - \alpha \cdot (T - T_0)), \tag{4.55}$$

where ρ_0 is the reference density, T_0 is the reference temperature and α is the thermal expansivity. To account for temperature evolution in the model, the energy equation is also solved with JustRelax.jl:

$$\rho C_\mathrm{p} \frac{DT}{Dt} = \frac{\partial}{\partial x_i}\left(k \frac{\partial T}{\partial x_i}\right), \tag{4.56}$$

where C_p is the heat capacity and κ the thermal conductivity. A benchmark for adjoint sensitivities with dislocation creep viscosity is provided in Appendix 4.C.

4.5.2.1 Setup

The setup of the 2D subduction zone consists of a subducting oceanic lithosphere to the left of the model domain and an overriding continental lithosphere to the right. Figure 4.8 shows the initial temperature and density structure. The model domain extends 3500 km in the horizontal x-direction and 710 km in the vertical z-direction. The upper 50 km consists of a sticky-air layer with a viscosity of 10^{19} Pas and a density of 100 kg/m^3. An oceanic crust with a linear viscosity of 10^{20} Pas forms the top of the left lithosphere, while the top of the right lithosphere consists of a 30 km thick continental crust with a viscosity 10^{23} Pas and a reference density of 2900 kg/m^3. The viscosity of the oceanic crust is artificially low, as the model is visco-elastic and the crust serves as a weak layer for the subducting plate. The reference density of the oceanic crust and the mantle phase is 3300 kg/m^3. The initial temperature profiles are approximated with the halfspace cooling model (Turcotte and Schubert, 2002), where a thermal age of 150 Myr is assumed for the continental part and a maximum thermal age of 80 Myr for the oceanic lithosphere. The oceanic lithosphere thins out to the left of the model (see Figure 4.8).

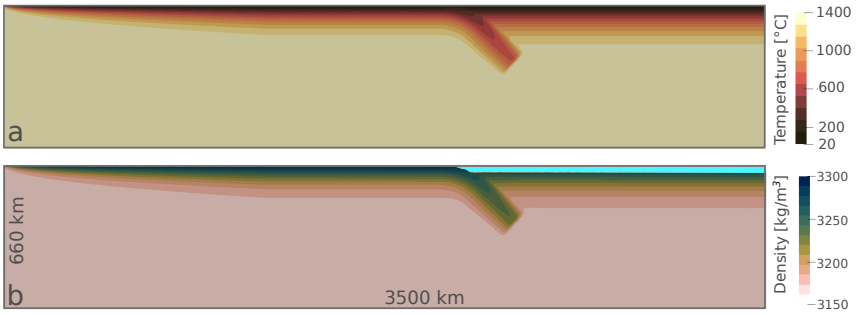

FIGURE 4.8: Initial Setup fo the 2D subduction simulation. (a) shows the initial temperature setup and (b) shows the initial density configuration. Turquoise colors in plot (b) show the density of the continental crust of 2900 kg/m^3.

The parameters for the viscosity can be obtained from Table 4.4. A minimum and maximum viscosity of 10^{19} Pas and 10^{24} Pas, respectively, are assumed. The remaining parameters are shear modulus $G = 6 \cdot 10^{10}$ Pa, heat capacity $C_p = 1000$ J/kg/K, thermal conductivity $k = 3$ W/K/m, thermal expansivity $\alpha = 3 \cdot 10^{-5}$ 1/K

and reference temperature $T_0 = 20°C$. The simulation is performed on a numerical grid of 512 × 128 cells in x- and z-directions, respectively, with an absolute solver tolerance of 10^{-4} for both the forward and the adjoint solver.

TABLE 4.4: Parameters for dislocation and diffusion creep laws.

Dislocation creep	A $[\mathrm{Pa}^{-n}\,\mathrm{m}^{-p}\,\mathrm{s}^{-1}]$	E $[\mathrm{J\,mol}^{-1}]$	V $[\mathrm{m}^3\,\mathrm{mol}^{-1}]$	n	p	r
Dry Olivine[a]	1.1×10^{-16}	530×10^3	14.0×10^{-6}	3.5	0.0	0.0
Diffusion creep	A $[\mathrm{Pa}^{-n}\,\mathrm{m}^{-p}\,\mathrm{s}^{-1}]$	E $[\mathrm{J\,mol}^{-1}]$	V $[\mathrm{m}^3\,\mathrm{mol}^{-1}]$	n	p	r
Dry Olivine [a,c]	1.5×10^{-15}	375×10^3	8.0×10^{-6}	1.0	−3.0	0.0

[a] Hirth and Kohlstedt (2003).
[c] A constant grain size of $d = 5 \cdot 10^{-3}$ m is used.

4.5.2.2 Simulation Results

The subduction simulation was run for 8 Myr. The time evolution of the simulation is shown in Figure 4.9. As can be seen, the horizontal velocity of the subducting plate reaches its peak of approximately 5 cm/yr at around 2 Myr. From this point on, the horizontal plate velocity in the model decreases to a value of around 2 cm/yr at 8 Myr. In the mantle beneath the plate, a return flow is occurs, with velocities on the order of 1 and 2 cm/yr. The continental plate on the right side of the model remains largely unaffected by the subduction process, while a small-scale, anticlockwise circular flow develops in the mantle above the subducting plate.

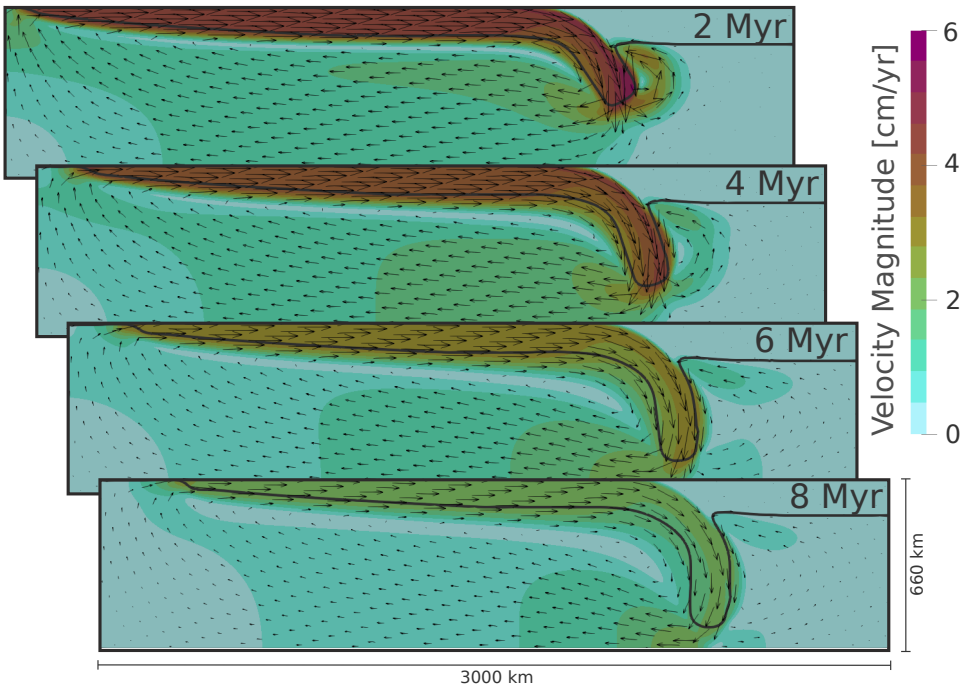

FIGURE 4.9: Results of the 2D subduction simulation at four different timesteps, from 2 Myr at the top to 8 Myr at the bottom. The black line indicates the 1200 °C isotherm. In the x-direction, the model shows the section between 0 km and 3000 km, omitting the last 500 km on the right.

Figure 4.10 shows the resulting effective viscosity of the simulation at 2 Myr and 8 Myr. A low-viscosity layer develops beneath the subducting plate. In the mantle,

the maximum effective viscosity decreases from 10^{24} Pas at 2 Myr to approximately 10^{23} Pas at 8 Myr. Above the subducting plate, a low viscosity zone can be observed. This layer originates from the oceanic crust with linear viscosity of 10^{20} Pas.

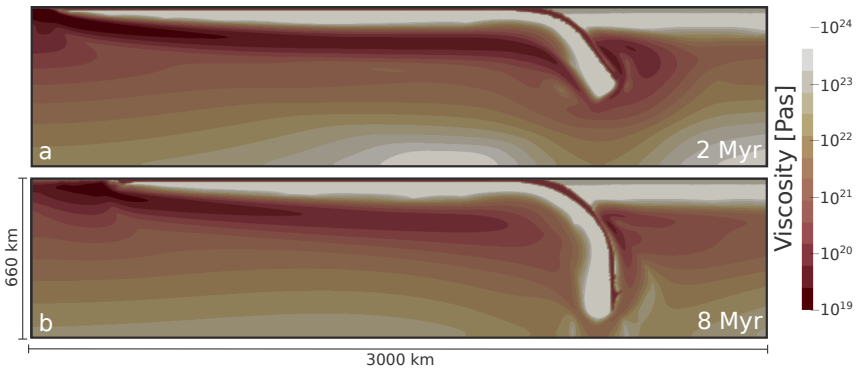

FIGURE 4.10: Effective viscosity of the subduction simulation at (a) 2 Myr and (b) 8 Myr.

4.5.2.3 Sensitivity Results

In this section, we aim to investigate the horizontal motion of the plate in the subducting region. Therefore, the observation points are chosen to be located in the horizontal part of the subducting plate between 1300 km and 1600 km in the x-direction and between a depth of 20 km and 40 km. In Figure 4.11, this location is marked with a pink line in every snapshot of the model results. Here, the horizontal velocity v_x is investigated, which differs from the sensitivities in the previous section and from our definition of the objective function in Equation 4.11, which is based on the vertical velocity component v_z. In Figure 4.11, the sensitivities are shown with respect to the effective viscosity η_{eff} and the density ρ based on Equation 4.55.

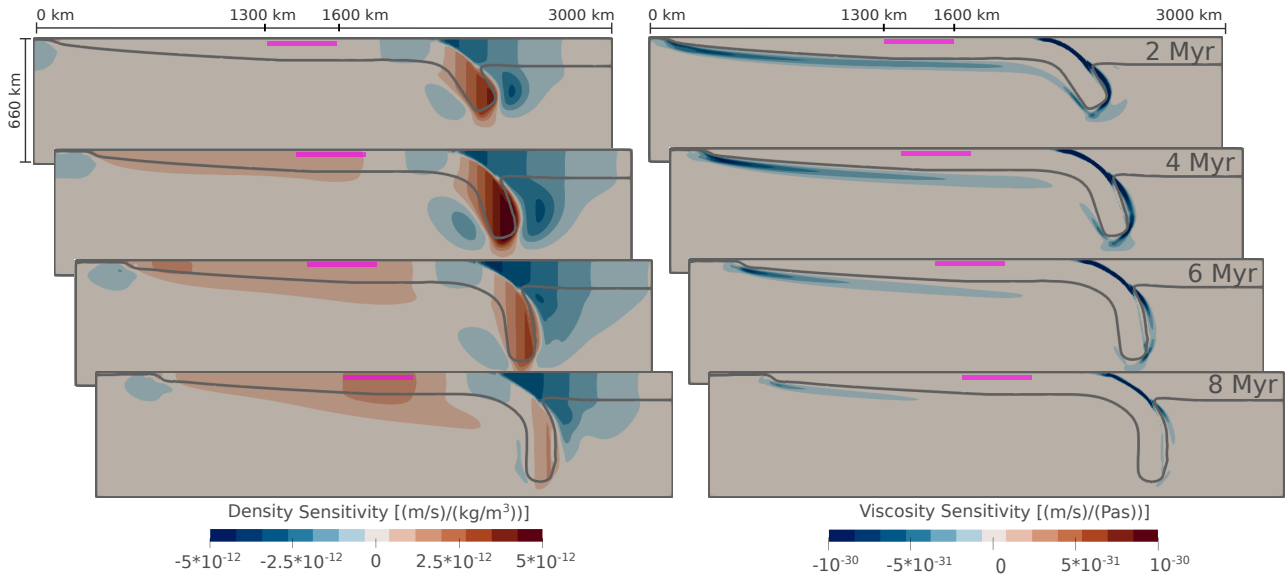

FIGURE 4.11: The sensitivities of density and effective viscosity in the 2D subduction simulation are shown on the left and right, respectively. The pink line indicates the location of the observation points. Four timesteps are presented: the first row at 2 Myr, the second row at 4 Myr, the third row at 6 Myr, and the fourth row at 8 Myr.

The left column of Figure 4.11 shows the sensitivity with respect to density, while the right column shows the sensitivity of the effective viscosity. Note that in both cases, the parameter is an effective parameter evaluated within the solver and is not a variable that can be directly provided as an input. However, this has been actively chosen, as these are the effective input parameters for the Stokes equations and thus provide insight into the driving forces of the simulation.

The density sensitivity exhibits distinct regions of low and high values over the entire time period. Beginning at 2 Myr, a strong positive sensitivity anomaly is observed in the slab portion that extends into the mantle. In contrast, a strong negative sensitivity anomaly appears above the hanging slab in the mantle and lithosphere. Two additional regions are also evident: one to the left of the model in the ridge area, and another horizontal section of the subducting slab just before it bends into the mantle. At 4 Myr, the pattern remains similar, with a new region becoming significant as the horizontal part of the subducting slab exhibits a positive sensitivity anomaly. At 6 Myr, the size of this anomaly increases and the magnitude of the positive anomaly in the hanging slab decreases. This continues until 8 Myr, when the positive anomaly in the hanging slab weakens drastically, while the anomaly in the horizontal slab remains equally strong. The negative anomaly above the hanging slab and in the ridge region remains relatively constant throughout the whole simulation.

The pattern of viscosity sensitivity differs markedly from that of density sensitivity. In general, only negative anomalies are observed in the viscosity sensitivity plot (right column in Figure 4.11). At 2 Myr the slab is almost entirely enclosed by a negative anomaly of the viscosity sensitivity. The anomaly peaks in the region of the interface between the downgoing slab and the continental lithosphere and mantle. A similar pattern is observed at 4 Myr. Starting at 6 Myr, the negative anomaly beneath the horizontal part of the subducting plate retreats toward the left side of the model. This trend continues until 8 Myr, when the negative sensitivities gradually weaken throughout the model.

The results of the sensitivities with respect to direct input parameters are omitted here. However, Appendix 4.D shows the sensitivity results of $V_{\text{dis}}, V_{\text{dif}}, E_{\text{dis}}, E_{\text{dif}}, T$ and the upper cutoff viscosity at 4 Mry.

4.6 Discussion

4.6.1 Usage of Automatic Differentiation

In the implementation presented, AD was used to compute the local VJPs required for calculating the adjoint variables and the sensitivities (see Equations 4.24, 4.25 and 4.28). This allows the functions of the forward solver to be reused in the adjoint solver, so that any changes to the forward solver are automatically reflected in the adjoint solver. A similar approach has been applied by Utkin et al. (2025) for the shallow ice approximation, which is a simplification of the full Stokes problem. In practice, some of the functions in the forward solver needed to be slightly rewritten to make use of them in the adjoint solve. For example, in the forward solve, the residual of the momentum equation and the velocity update are performed in a single function. For the adjoint solver, this needs to be split, as the momentum residual routine is called first, while the function updating the adjoint variable is called last. This example illustrates that, in general, it is advantageous to develop the forward and adjoint codes simultaneously, allowing them to evolve together.

The time per pseudo-transient iteration differs in the forward solve and the adjoint solve. The average time per iteration in the forward solve on an NVIDIA A100 with

80 GB of GPU memory for the subduction example with 512×128 grid cells was 0.0006 s. A pseudo-transient iteration in the adjoint solver took on average 0.025 s, making it roughly 40 times slower than the forward solver. This is partly compensated by the fact that the adjoint solver in these simulations required 2 to 4 times fewer iterations than the forward solver to reach the same numerical precision. In general, for sensitivity analysis, this difference is not critical, as sensitivities do not need to be computed at every timestep but only, for example, when visualizing the output. In the subduction example, sensitivities were calculated every 40 timesteps, so the slower adjoint solver was not a limiting factor. However, for large-scale inversions of geodynamic processes (e.g., Yang and Gurnis, 2016; Ghelichkhan et al., 2021), this may become limiting, potentially requiring the adjoint solver to be implemented manually.

4.6.2 Scaling of Adjoint Sensitivities: Plume Example

The rising plume head example illustrates how adjoint sensitivities can provide insights into physical processes and allow for the comparison of different material parameters on a specific process. Here, the objective function was changed every timestep, in order to "follow" the ascent of the rising plume head.

The density inside the plume, as well as above and below it, negatively affected the rising velocity, meaning that an increase in density reduces the ascent velocity. To gain insight into how each material phase influences the objective function, the spatial sensitivities of each phase can be summed and compared with those of other material phases. Overall, as expected, the mantle and plume density were the most significant parameters for the ascent velocity of the plume head.

To analyze the parameters, the sensitivities were scaled with the parameter value and the value of the objective function itself (Equation 4.51). In the literature, these relative sensitivities are often referred to as "Elasticity" (e.g., Borgonovo and Peccati, 2004; Åberg et al., 2009). This has already been applied in geodynamics in order to derive multiplicative scaling laws of physical processes (e.g., Reuber et al., 2018; Reuber, 2021). The resulting dimensionless scaled sensitivities illustrate the relative change in the objective function for a relative change in the parameter itself. However, if sensitivities are calculated for a specific combination of parameters, it is not clear for which parameter space, these sensitivities are applicable. To investigate this further, the global desired parameter space must be explored. Then, it is possible to figure out how many different sets of sensitivities (scaling laws) are required to describe the desired parameter space (Reuber, 2021).

Another interesting aspect of the sensitivities is to check how pure numerical parameters influence the objective function. That has been done in Table 4.3, which shows that the material parameters of the sticky air do not significantly influence the model results.

4.6.3 Investigation of Horizontal Plate Motion during Subduction

In this section, the sensitivity results for the 2D subduction example are discussed. Adjoint sensitivities were computed for an objective function that sums the horizontal velocity within the horizontal part of the subducting plate. The sensitivity results for density and effective viscosity, presented in Figure 4.11, are investigated. Here, the sensitivities are not scaled, instead, the anomalies are attributed to different driving forces. The extent to which slab pull and ridge push forces influence horizontal plate

motion is quantified and a ratio between these two driving forces is established and analyzed over the course of the simulation.

We first examine the sensitivities of the effective viscosity (right column in Figure 4.11). At 2 Myr, a negative anomaly extends from the ridge to the region beneath the horizontal plate, following the subducting plate and transitioning into the interface between the slab and the overriding plate. The sensitivities reflect regions of low viscosity (Figure 4.10a), where the layer beneath the subducting plate corresponds to the weak asthenospheric channel during subduction, and the anomaly at the subduction interface corresponds to the low-viscosity layer, which was introduced to mimic the subduction channel. The strongest sensitivities are at the interface between the subducting slab and the overriding plate. These anomalies gradually become weaker as the simulation progresses.

The density anomalies present a different pattern. Throughout the simulation, a negative anomaly in the density sensitivities appears above the slab in both the mantle and lithosphere (left column in Figure 4.11), indicating that a reduction in density increases plate velocity in this region. This effect can be attributed to the load exerted by this region on the subduction interface, which increases with higher density. The negative anomaly in the ridge region also persists throughout the simulation. This can be explained by the upwelling of mantle material in this area, where lower-density material rises more rapidly, resulting in an increased spreading velocity of the ridge.

In addition, during the simulation, two positive anomalies in the density anomaly can also be detected. One anomaly is located in the slab region, and the other is situated in the horizontal part of the subducting plate.

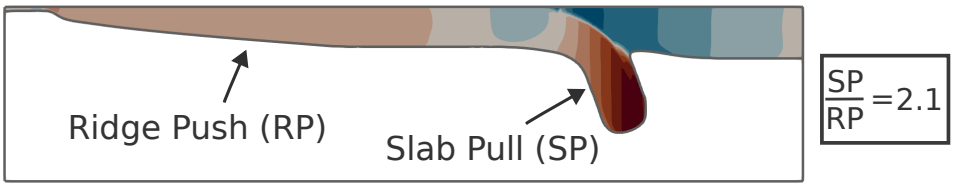

FIGURE 4.12: Density sensitivities for 2D subduction simulation at 4 Myr. For the colorscale, refer to the left column of Figure 4.11. Only sensitivity values at locations with temperatures below 1300 °C are shown. To the right, the ratio between slab pull and ridge push is indicated. For en explanation, how this ratio was computed, please refer to the text.

In Figure 4.12, sensitivities at locations cooler than 1300°C are displayed, so that only the lithospheric contributions are shown. The positive anomaly in the horizontal portion of the plate reflects the influence of ridge push. In contrast, the positive anomaly in the subducted plate corresponds to the influence of slab pull. This assumption can be made because both processes are driven by the density of the material (e.g., Turcotte and Schubert, 2002).

To compare slab pull and ridge push during the subduction, the sensitivities of the two anomalies are summed per driving mechanism. By calculating the ratio between the summed sensitivities of slab pull and ridge push, respectively, it is shown that slab pull has 2.1 times greater influence on horizontal plate motion than ridge push at 4 Mry. To further analyze the ratio between slab pull and ridge push, the ratio was calculated at eight time points between 1 Myr and 8 Myr and the time evolution of this ratio is shown in Figure 4.13b.

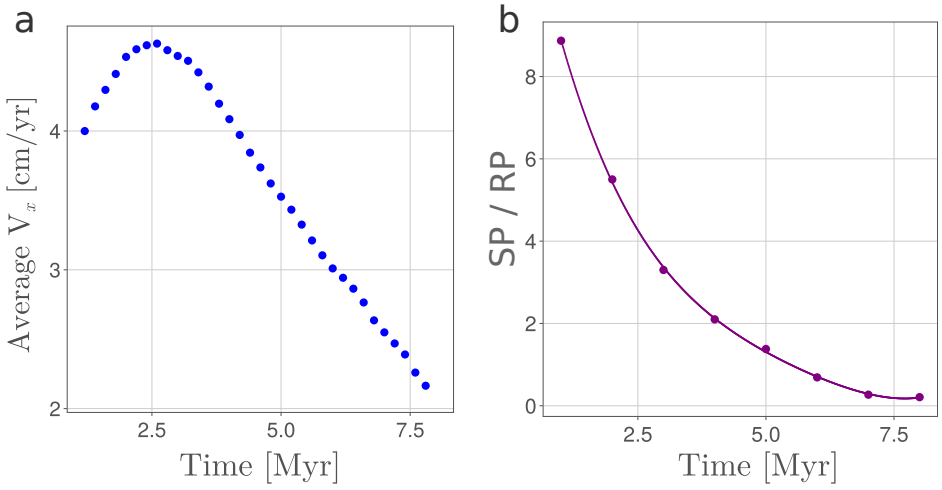

FIGURE 4.13: a) shows the average velocity of the horizontal part of the subducting plate between 1 Myr and 8 Myr, and (b) shows the SP/RP ratio for the same time period. A fourth-order polynomial was fitted through the eight data points, which are highlighted with circles.

Figure 4.13 shows both the evolution of the average horizontal plate velocity and the changes in the ratio between slab pull and ridge push. The plate velocity peaks at around 2.5 Myr and subsequently decreases from approximately 5 cm/yr to 2.2 cm/yr at 8 Myr. However, the slab pull–ridge push ratio decreases continuously from the beginning of the simulation. It starts with a ratio greater than 8 and decreases logarithmically, reaching approximately 0.21 at 8 Myr. Since 6 Myr, the ratio falls below 1, indicating that ridge push becomes more important than slab pull. By examining the simulation results, this can be explained by the fact that the slab reaches the lower part of the asthenosphere (Figure 4.9), which serves as a closed boundary in our simulation.

Overall, it was demonstrated that sensitivities can be used to quantify geodynamic processes. This was illustrated here using the example of competing slab pull and ridge push forces during subduction. Other methods also exist, for example, previous studies have quantified slab pull by integrating the buoyancy of the hanging slab (e.g., Bessat et al., 2020; Candioti et al., 2021). This can be seen as an upper limit for the slab pull force, as other factors, such as shear stresses in the mantle, counteract this process (Candioti et al., 2021).

4.6.4 Limitations

The forward solver uses the accelerated pseudo-transient method (e.g., Räss et al., 2022; Alkhimenkov and Podladchikov, 2024). A different pseudo-transient scheme was used for the adjoint solver (see Appendix 4.B). However, the accelerated pseudo-transient method could also be applied to the adjoint solve, enhancing efficiency and compatibility with the forward solver and thereby simplifying the use of AD.

In the current implementation, some functions of the forward solver were changed in order to make them compatible with the way Enzyme.jl is called in the routines. In the presented implementation, Enzyme functions require arrays of material parameters containing their values at every location as an input argument. Since many functions in the forward solver evaluate material parameters pointwise within each

specific function, several functions had to be rewritten to pass the material parameters as arrays. This should be adapted in the future to utilize the functions of the forward solver.

The implementation could be extended to also account for visco-elasto-plastic rheologies and thus for more realistic subduction setups.

4.7 Conclusions

This chapter presented implementation details of a discrete adjoint method, which is numerically solved using the pseudo-transient method by employing automatic differentiation. The second part of the chapter explains the use of adjoint sensitivities to analyze the results of two numerical simulations: a plume head rising through the asthenosphere and a 2D subduction zone simulation.

In general, the applicability of AD has been demonstrated, showing how it can be used to construct a problem-agnostic adjoint solver. It has been demonstrated how reverse-mode AD can be used to compute local VJPs within the matrix-free pseudo-transient method, and therefore making it well suited for large-scale problems and even 3D simulations (Räss et al., 2022).

Secondly, it has been shown how adjoint sensitivities can be used for quantitative sensitivity analysis of numerical model results. We demonstrated how scaling of sensitivities enables comparisons between the sensitivities of different parameters and across different timesteps. By varying the objective function, different processes can be investigated. For example, the influence of material parameters on possible observables such as the horizontal plate motion can be assessed. Another possibility is to investigate intrinsic processes, like the ascent of a mantle plume, which can be examined by adapting the objective function at each timestep to track the plume's ascent. Sensitivities can also be employed to assess the impact of numerical parameters, such as the upper cutoff viscosity in the Stokes solver (Appendix 4.D).

Lastly, a 2D subduction example was analyzed to demonstrate the applicability of the adjoint solver for problems with nonlinear visco-elastic rheology. Sensitivities for the horizontal plate motion with respect to the effective viscosity and density were investigated. This highlighted key processes that drive subduction, such as ridge push and slab pull. Adjoint sensitivities allow for a quantitative assessment of these processes. In this context, a ratio between the influence of ridge push and slab pull was introduced to quantify the relative importance of both processes and analyze its evolution.

4.8 Appendix

4.A Numerical Pseudo-Transient Parameters Forward Solver

The numerical terms that appear in the Equations 4.6, 4.7 and 4.10 can be calculated as follows:

$$V_p = \frac{c_{\mathrm{CFL}}\Delta x}{\Delta\phi} \iff V_p\Delta\phi = \left[c_{\mathrm{CFL}}\,\Delta x\right], \tag{4.57}$$

$$\tilde{\rho} = Re\frac{\eta}{V_p L} \iff \frac{\tilde{\rho}}{\Delta\phi} = \left[\frac{Re}{(V_p\Delta\phi)L}\right]\eta, \tag{4.58}$$

$$\tilde{G} = \frac{\tilde{\rho}V_p^2}{r+\frac{4}{3}} \iff \frac{1}{\tilde{G}\Delta\phi} = \left[\frac{L(r+\frac{4}{3})}{Re(V_p\Delta\phi)}\right]\frac{1}{\eta}, \tag{4.59}$$

$$\tilde{K} = r\tilde{G} \iff \frac{1}{\tilde{K}\Delta\phi} = \left[\frac{1}{r}\frac{L(r+\frac{4}{3})}{Re(V_p\Delta\phi)}\right]\frac{1}{\eta}. \tag{4.60}$$

The formulation for the numerical parameters V_p, $\tilde{\rho}$, $\tilde{G}$ and $\tilde{K}$ are obtained from Räss et al. (2022). The terms on the right-hand side of the equivalent transformation must be computed to update the solution variables. The parts in square brackets can be calculated before the simulation starts. η denotes the spatially varying viscosity, updated at each timestep, and L is the minimum length scale of the model in the x- or z-direction. Δx is the minimum value of the grid spacing in x- and z-direction. In the plume head simulations $Re = 15\pi$, $r = 1$ and $c_{CFL} = \frac{0.95}{\sqrt{2.1}}$, whereas the other parameters arise from the model setup.

4.B Numerical Pseudo-Transient Parameters Adjoint Solver

In order to solve for the adjoint variables $\boldsymbol{\lambda_v}$ and λ_P another pseudo-transient timestepping approach is chosen compared to the forward solve described in Appendix 4.A. The pseudo timestep for Equation 4.24, denoted with $\Delta\phi_{\lambda_v}$ and the equivalent for Equation 4.25 $\Delta\phi_{\lambda_P}$ can be calculated as follows:

$$\Delta\phi_{\lambda_v} = \alpha \cdot (\Delta x)^2/\eta/4.1\,, \tag{4.61}$$

$$\Delta\phi_{\lambda_P} = \beta \cdot \eta \cdot 4.1/n_{max}\,. \tag{4.62}$$

Here α and β are numerical parameters, which in case of the plume head example are set to 0.8 and 0.125, respectively. Δx is the minimum value of the grid spacing in $x-$ and $z-$direction and n_{max} is the maximum of the grid cell number in $x-$ and $z-$ direction. The solution variables $\boldsymbol{\lambda_v}$ and λ_P are updated with an explicit time integration scheme as follows:

$$\xi_x = 1 - 5/n_x \cdot \xi_x + R_{\lambda_{v_x}}\,, \tag{4.63}$$

$$v_x^{new} = v_x^{old} + \xi_x \cdot \Delta\phi_v\,, \tag{4.64}$$

$$\xi_y = 1 - 5/n_y \cdot \xi_y + R_{\lambda_{v_y}}\,, \tag{4.65}$$

$$v_y^{new} = v_y^{old} + \xi_y \cdot \Delta\phi_v\,, \tag{4.66}$$

$$\lambda_P^{new} = \lambda_P^{old} + R_{\lambda_P} \cdot \Delta\phi_P\,, \tag{4.67}$$

where $R_{\lambda_{v_x}}$ and $R_{\lambda_{v_x}}$ are the residuals of Equation 4.24 and R_{λ_P} is the residual of Equation 4.25. n_x and n_z is the number of grid cells in $x-$ and $z-$ direction. This method has already been successfully applied in previous studies, such as Kiss et al. (2023).

4.C Benchmark Dislocation Creep Viscosity

This benchmark is adapted from the pure shear example in Section 4.4.1. The boundary conditions are similar and the phases are again distributed into a matrix and a block. However, in this case, the viscosity is defined as a dislocation creep law, described in Equation 4.53. The parameters for the dislocation viscosity of the matrix and the block are given in Table 4.5. f and R are set to 1. The remaining material parameters for this benchmark are adapted from the example in section 4.4.1. Figure 4.15 shows the gradient test for this benchmark. The cost function is the same as in Section 4.4.1.

TABLE 4.5: Material parameters for dislocation creep benchmark.

Phase	A	n	r	E	V	T_{ref}
Matrix	0.01	3	1	1	0.01	1
Block	0.1	3	1	1	0.01	1

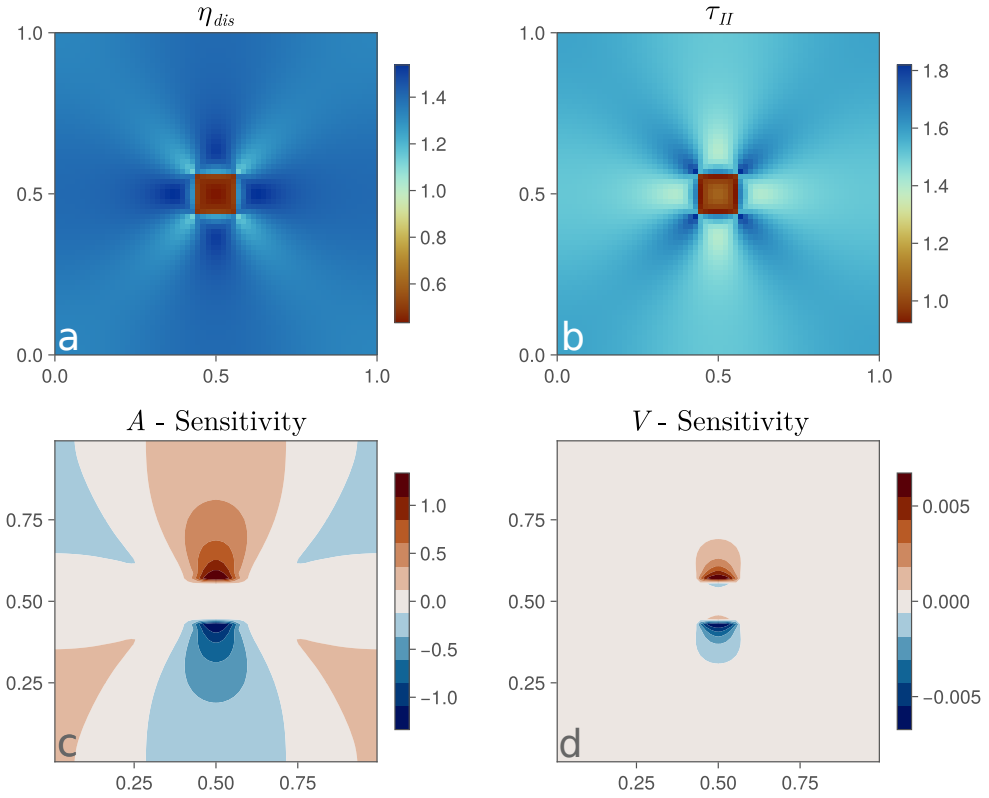

FIGURE 4.14: Dislocation creep benchmark. (a) and (b) show forward solver results for viscosity η_{dis} and the second invariant of the stress tensor τ_{II}, respectively. (c) and (d) show the corresponding sensitivities to A and V.

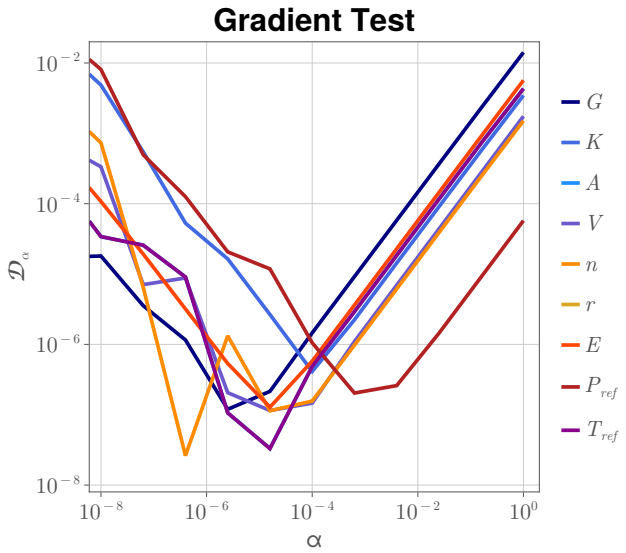

FIGURE 4.15: Gradient test of the dislocation creep benchmark for G, K, A, V, n, r, E, P_{ref} and T_{ref} .

4.D 2D Subduction Sensitivities

In Figure 4.16, the sensitivity results of the 2D subduction simulations for the parameters $V_{\text{dif}}, V_{\text{dis}}, E_{\text{dif}}, E_{\text{dis}}$, the upper cutoff viscosity η_{up} and T are shown.

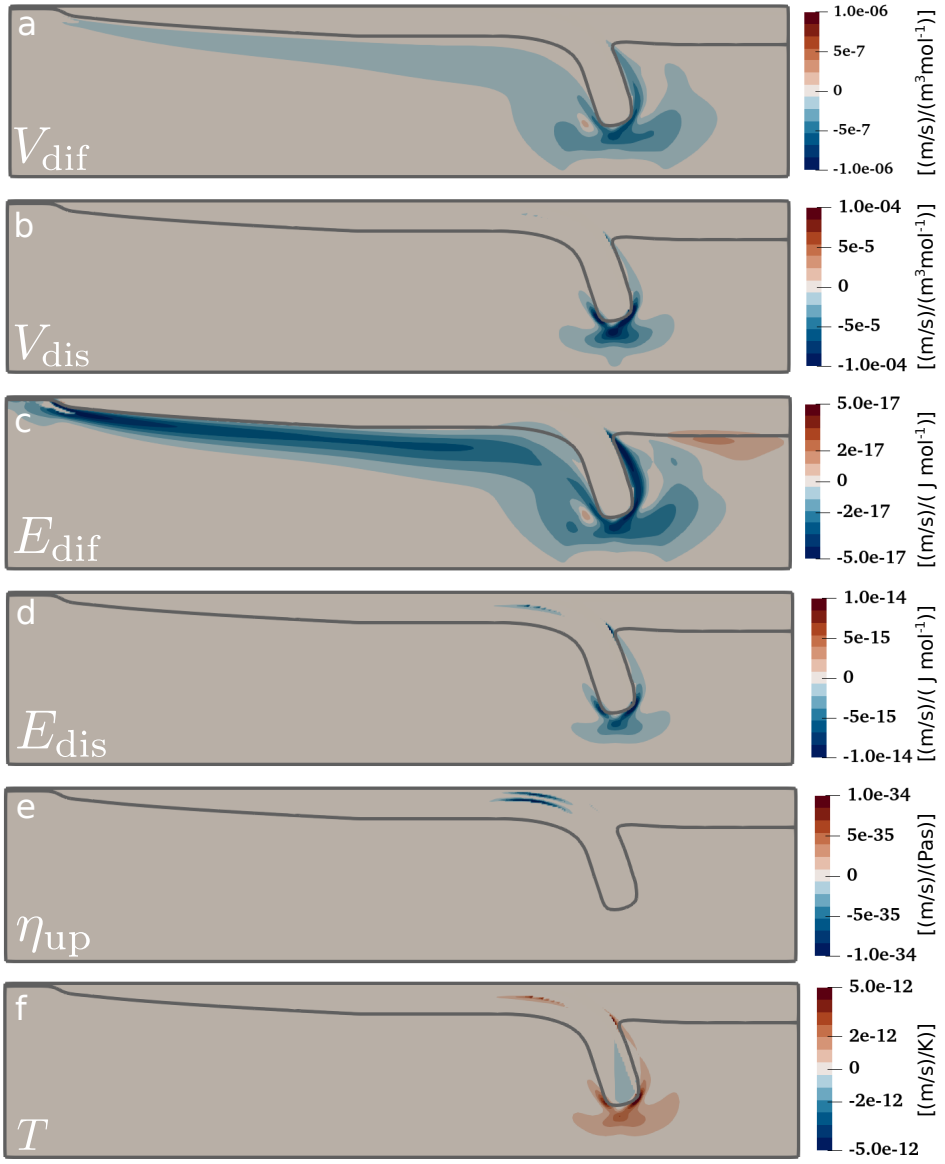

FIGURE 4.16: Sensitivity results for the parameters $V_{\mathrm{dis}}, V_{\mathrm{dif}}, E_{\mathrm{dis}}, E_{\mathrm{dis}}, T, \eta_{\mathrm{up}}$. The same objective function as in section 4.5.2.3 has been used.

Chapter 5

Summary and Outlook

This work presented various methods for investigating upper mantle dynamics and plate motion, with a particular focus on the Mediterranean region. The work spans from a case study of the Mediterranean to a more general approach for analyzing subduction zone plate motion using adjoint sensitivities. The following two sections summarize the main outcomes of the three core chapters, followed by a discussion of potential implications for future studies.

5.1 Summary

Chapter 2 analyzed the mantle dynamics in the Mediterranean region with 3D thermomechanical modeling. The retreat of the rollback subduction systems of the Mediterranean over the last 35 Myr was explored, which helped to understand how distinct subduction systems influence each other. These subduction zones and the convergence of the Eurasian and African plates interact with each other, and the plate motion of this whole area can only be explained by an interplay of all these factors. The Adriatic microplate plays a key role in this area, as it is located in the center of the Mediterranean, between the Eurasian and African plates and surrounded by subduction zones. The models show that the plate motion of the Adriatic microplate is driven by three main factors: the convergence of the African and Eurasian plates, the horizontal distance between the Calabrian and Hellenic trenches, and the retreat of the Alpine slab north of Adria. The mantle dynamics beneath Adria is controlled by the two subduction systems to its west and east: the Apennines-Calabrian subduction and the Dinaric-Hellenic subduction. As they approach the Adriatic microplate, the dynamic pressure beneath Adria increases, driving an escape flow to both the north and south. To the north, the mantle material can only escape eastward, consequently inducing a mantle flow parallel to the Alpine subduction.

In Chapter 3, the model results of the previous chapter were used to calculate synthetic shear wave splitting parameters for the Mediterranean. These were then compared with observations from the Mediterranean, with a particular focus on the Alpine region. The comparison shows that first-order features of the observations in the Mediterranean can be reproduced, such as the orientation of the FPD perpendicular to the trenches of the Calabrian and Hellenic slabs, a circular FPD pattern north of the Alpine slab and trench-parallel FPD south of the Alpine slab. However, the comparison did not result in the model fitting the observations perfectly. For instance, the model shows high delay times between the Alpine and Apenninic slabs due to mantle flow between them. This phenomenon is absent from the observations, suggesting that the Alpine and Apenninic slabs act as a barrier to mantle flow to the northwest. Other discrepancies are observed in the Liguro-Provençal Basin, where Link and Rümpker (2023) report a switch in FPD at greater depth. In the model, with an intact Apennines slab, this feature is not reproduced, suggesting that it may

result from a process absent in the model, such as a slab gap of the Apennines slab or an anisotropy contribution from the lower mantle. Overall, it has been shown that shear wave splitting observations provide valuable additional constraints for the geodynamic model, as they also contain information about the deformation history of the mantle, not just the present-day structure. Conversely, the model results help to explain the observations, as they allow us to observe mantle flow over time.

Chapter 4 outlines the implementation of a discrete adjoint solver, which was built on top of an existing Stokes solver using AD and the pseudo-transient method. It was shown in detail how AD is implemented and how it can be used to construct a problem-agnostic adjoint solver. In the second part, it is shown how adjoint sensitivities can be used for sensitivity analysis and how the sensitivities can be scaled to allow a comparison between different material parameters. A 2D subduction model with nonlinear visco-elastic rheology was examined to quantify the main processes controlling the horizontal velocity of the subducting plate. The effects of slab pull and ridge push on plate motion were quantified and compared to establish a ratio between these two forces.

5.2 Outlook

The results of the 3D thermomechanical simulations can be used to further investigate the geodynamics in the Mediterranean and explore regional processes. Several studies have investigated the ongoing deformation of the Adriatic microplate (e.g., Battaglia et al., 2004; Scisciani and Calamita, 2009). Therefore, the stress within the Adriatic lithosphere could be analyzed to understand how it evolves during the simulation and how it is influenced by the surrounding subduction zones and the convergence between Africa and Eurasia.

Another interesting aspect is how upper mantle dynamics effect crustal processes such as orogeny and vertical surface uplift. Previous studies have shown that slab break-off events can produce a distinct surface response (e.g., Duretz et al., 2011; Hunen and Allen, 2011; Eskens et al., 2025). The models presented here could be used to investigate these processes with a direct application to the Mediterranean.

To address the question of what shear-wave splitting observations reveal about the deformation history of the upper mantle, it is essential to understand how the present-day anisotropic pattern correlates with deformation (e.g., Ribe, 1992). Numerical modeling provides a way of looking into the past and identifying the processes that contributed to the observed pattern. The shear-wave splitting results from the model could be calculated for different geological times, for example, starting at 5 Ma, 10 Ma and 20 Ma. Comparing these results would provide deeper insights into how mantle flow has shaped the seismic anisotropy of the Mediterranean.

Analyzing sensitivities provides a quantitative way to interpret model results and is therefore well-suited for many types of numerical modeling studies. In the future, different processes could be investigated by modifying the objective function, for which we have presented a well-suited framework. This could involve incorporating principal stress directions into the objective function, as demonstrated by Reuber et al. (2020a). Furthermore, to account for more realistic visco-elasto-plastic rheologies, the adjoint solver needs to be extended for combined plastic rheologies.

In the future, the adjoint solver could also be used for inversions in the context of geodynamics (e.g., Worthen et al., 2014; Li et al., 2017; Ghelichkhan et al., 2024). The Julia framework appears well suited for this, as the code presented in this work

can, with minor modifications, run on multiple GPUs, potentially enabling large-scale geodynamic inversions (e.g., Reuber et al., 2020b; Räss et al., 2022).

Appendix

A Use of Artificial Intelligence Tools

The use of artificial intelligence (AI) tools in the thesis is listed in Table A.

TABLE A: Declaration of the use of AI tools in the thesis, including the use case and an explanation of why and where it was used.

AI Tool	**Utilization**	**Why**	**When**
ChatGPT	Correcting grammar, reformulation of text passages, editing LaTeX code, debbuging Julia code for plotting routines, research about the adjoint method	Improving readability, writing quality, improve the appearance of the document based on the LaTeX code, improving the quality of the Julia plots, get an overview over the adjoint method	Throughout the entire thesis
DeepL Write	Correcting grammar, reformulation of text passages	Improving readability, writing quality	Throughout the entire thesis
Grammarly	Correct spelling and grammar mistakes	Readability	Throughout the entire thesis

B Software

For the visualization of the model results, the software ParaView was used. Additionally the Julia package CairoMakie (Danisch and Krumbiegel, 2021) was used for data plotting. The Julia package GMT.jl, which is based on the plotting software GMT (Wessel et al., 2019), was used for the plots in the introduction. The setup for the plume head and 2D subduction zone simulations was created with GeophysicalModelGenerator.jl (Kaus et al., 2024). Inkscape was used to edit the plots.

Acknowledgements

Eidesstattliche Erklärung

Hiermit erkläre ich, dass ich die vorliegende Arbeit selbstständig verfasst und keine anderen als die angegebenen Quellen und Hilfsmittel (dazu zählen auch KI-basierte Anwendungen oder Werkzeuge*) benutzt habe. Sämtliche wörtlichen oder sinngemäßen Übernahmen und Zitate sind kenntlich gemacht und nachgewiesen (dies gilt auch für Texte, die durch generative KI, wie Chat GPT erzeugt wurden). Ich versichere, dass ich keine Hilfsmittel verwendet habe, deren Nutzung die Prüferin oder der Prüfer explizit ausgeschlossen hat. Im Anhang „Nutzung KI-Tools“ habe ich die verwendeten KI-Tools dokumentiert. Mit Abgabe der vorliegenden Leistung übernehme ich die Verantwortung für das eingereichte Gesamtprodukt. Ich verantworte damit auch jegliche KI-generierten Inhalte, die ich in meine Arbeit übernommen habe. Die Richtigkeit übernommener (KI generierter) Aussagen und Inhalte habe ich nach bestem Wissen und Gewissen geprüft. Mir ist bekannt, dass ein Verstoß gegen die genannten Punkte prüfungsrechtliche Konsequenzen hat und insbesondere dazu führen kann, dass die Promotionsleistung als mit „nicht bestanden“ bewertet wird. Die Einschreibung kann für bis zu zwei Jahre widerrufen werden, wenn Studierende zweimal oder häufiger bei Prüfungsleistungen täuschen (§ 69 Abs. 4 und 5 HochSchG).

Christian Schuler
Mainz, 2025

Bibliography

Åberg, Per, Carl Johan Svensson, Hal Caswell, and Henrik Pavia (2009). "Environment-specific elasticity and sensitivity analysis of the stochastic growth rate". In: *Ecological Modelling* 220.5, pp. 605–610.

Aellig, Pascal, Albert de Montserrat, Patrick Sanan, Ludovic Räss, Sidney Beeler, Boris Kaus, Hendrik Ranocha, Christian Schuler, Iván Navarrete Jara, and Lukas Fuchs (2025). *PTsolvers/JustRelax.jl: v0.4.1 (v0.4.1)*. https://doi.org/10.5281/zenodo.15058433.

Alkhimenkov, Yury and Yury Y Podladchikov (2024). "Accelerated pseudo-transient method for elastic, viscoelastic, and coupled hydro-mechanical problems with applications". In: *Geoscientific Model Development Discussions* 2024, pp. 1–35.

Alpert, Lisa A, Meghan S Miller, Thorsten W Becker, and Amir A Allam (2013). "Structure beneath the Alboran from geodynamic flow models and seismic anisotropy". In: *Journal of Geophysical Research: Solid Earth* 118.8, pp. 4265–4277.

Anderson, Helen and James Jackson (1987). "Active tectonics of the Adriatic region". In: *Geophysical Journal International* 91.3, pp. 937–983.

Angrand, Paul and Frédéric Mouthereau (2021). "Evolution of the Alpine orogenic belts in the Western Mediterranean region as resolved by the kinematics of the Europe-Africa diffuse plate boundary". In: *BSGF-Earth Sciences Bulletin* 192.1, p. 42.

Baccheschi, P, L Margheriti, and MS Steckler (2007). "Seismic anisotropy reveals focused mantle flow around the Calabrian slab (Southern Italy)". In: *Geophysical Research Letters* 34.5.

Balay, S, S Abhyankar, Mark F Adams, S Benson, J Brown, P Brune, K Buschelman, EM Constantinescu, L Dalcin, A Dener, et al. (2024). *PETSc/TAO Users Manual Revision 3.21*. Tech. rep. Argonne National Laboratory (ANL), Argonne, IL (United States).

Barruol, Guilhem, Mickael Bonnin, Helle Pedersen, Götz HR Bokelmann, and Christel Tiberi (2011). "Belt-parallel mantle flow beneath a halted continental collision: The Western Alps". In: *Earth and Planetary Science Letters* 302.3-4, pp. 429–438.

Battaglia, Maurizio, Mark H Murray, Enrico Serpelloni, and Roland Bürgmann (2004). "The Adriatic region: An independent microplate within the Africa-Eurasia collision zone". In: *Geophysical Research Letters* 31.9.

Bauville, Arthur and Tobias S Baumann (2019). "geomIO: An open-source MATLAB toolbox to create the initial configuration of 2-D/3-D thermo-mechanical simulations from 2-D vector drawings". In: *Geochemistry, Geophysics, Geosystems* 20.3, pp. 1665–1675.

Baydin, Atilim Gunes, Barak A Pearlmutter, Alexey Andreyevich Radul, and Jeffrey Mark Siskind (2018). "Automatic differentiation in machine learning: a survey". In: *Journal of machine learning research* 18.153, pp. 1–43.

Becker, Thorsten W, Sebastien Chevrot, Vera Schulte-Pelkum, and Donna K Blackman (2006). "Statistical properties of seismic anisotropy predicted by upper mantle geodynamic models". In: *Journal of Geophysical Research: Solid Earth* 111.B8.

Becker, Thorsten W and Sergei Lebedev (2021). "Dynamics of the upper mantle in light of seismic anisotropy". In: *Mantle convection and surface expressions*, pp. 257–282.

Bessat, Annelore, Thibault Duretz, György Hetényi, Sébastien Pilet, and Stefan M Schmalholz (2020). "Stress and deformation mechanisms at a subduction zone: insights from 2-D thermomechanical numerical modelling". In: *Geophysical Journal International* 221.3, pp. 1605–1625.

Bezanson, Jeff, Alan Edelman, Stefan Karpinski, and Viral B Shah (2017). "Julia: A fresh approach to numerical computing". In: *SIAM review* 59.1, pp. 65–98.

Blondel, Mathieu and Vincent Roulet (2024). "The elements of differentiable programming". In: *arXiv preprint arXiv:2403.14606*.

Boneh, Yuval and Philip Skemer (2014). "The effect of deformation history on the evolution of olivine CPO". In: *Earth and Planetary Science Letters* 406, pp. 213–222.

Borgonovo, Emanuele and Lorenzo Peccati (2004). "Sensitivity analysis in investment project evaluation". In: *International Journal of Production Economics* 90.1, pp. 17–25.

Borgonovo, Emanuele and Elmar Plischke (2016). "Sensitivity analysis: A review of recent advances". In: *European Journal of Operational Research* 248.3, pp. 869–887.

Boutelier, D and AR Cruden (2017). "Slab breakoff: Insights from 3D thermo- mechanical analogue modelling experiments". In: *Tectonophysics* 694, pp. 197–213.

Bunge, Hans-Peter, CR Hagelberg, and BJ Travis (2003). "Mantle circulation models with variational data assimilation: inferring past mantle flow and structure from plate motion histories and seismic tomography". In: *Geophysical Journal International* 152.2, pp. 280–301.

Candioti, Lorenzo G, Thibault Duretz, Evangelos Moulas, and Stefan M Schmalholz (2021). "Buoyancy versus shear forces in building orogenic wedges". In: *Solid Earth* 12.8, pp. 1749–1775.

Catalano, Raimondo, Carlo Doglioni, and S Merlini (2001). "On the mesozoic Ionian basin". In: *Geophysical Journal International* 144.1, pp. 49–64.

Channell, JET, B d'Argenio, and F Horvath (1979). "Adria, the African promontory, in Mesozoic Mediterranean palaeogeography". In: *Earth-Science Reviews* 15.3, pp. 213–292.

Charpentier, Isabelle and Mohammed Ghemires (2000). "Efficient adjoint derivatives: application to the meteorological model Meso-NH". In: *Optimization Methods and Software* 13.1, pp. 35–63.

Chertova, MV, W Spakman, T Geenen, AP Van Den Berg, and DJJ Van Hinsbergen (2014). "Underpinning tectonic reconstructions of the western Mediterranean region with dynamic slab evolution from 3-D numerical modeling". In: *Journal of Geophysical Research: Solid Earth* 119.7, pp. 5876–5902.

Chevrot, Sébastien (2000). "Multichannel analysis of shear wave splitting". In: *Journal of Geophysical Research: Solid Earth* 105.B9, pp. 21579–21590.

Cifelli, Francesca, Massimo Mattei, and Federico Rossetti (2007). "Tectonic evolution of arcuate mountain belts on top of a retreating subduction slab: The example of the Calabrian Arc". In: *Journal of Geophysical Research: Solid Earth* 112.B9.

Civello, Sara and Lucia Margheriti (2004). "Toroidal mantle flow around the Calabrian slab (Italy) from SKS splitting". In: *Geophysical Research Letters* 31.10.

Civiero, Chiara, Susana Custódio, João C Duarte, Virgilio B Mendes, and Claudio Faccenna (2020). "Dynamics of the Gibraltar arc system: A complex interaction

between plate convergence, slab pull, and mantle flow". In: *Journal of Geophysical Research: Solid Earth* 125.7, e2019JB018873.

Confal, Judith M, Manuele Faccenda, Tuna Eken, and Tuncay Taymaz (2018). "Numerical simulation of 3-D mantle flow evolution in subduction zone environments in relation to seismic anisotropy beneath the eastern Mediterranean region". In: *Earth and Planetary Science Letters* 497, pp. 50–61.

Crameri, F, H Schmeling, GJ Golabek, T Duretz, R Orendt, SJH Buiter, DA May, BJP Kaus, TV Gerya, and PJ Tackley (2012). "A comparison of numerical surface topography calculations in geodynamic modelling: an evaluation of the 'sticky air'method". In: *Geophysical Journal International* 189.1, pp. 38–54.

D'agostino, N, A Avallone, D Cheloni, E D'anastasio, S Mantenuto, and G Selvaggi (2008). "Active tectonics of the Adriatic region from GPS and earthquake slip vectors". In: *Journal of Geophysical Research: Solid Earth* 113.B12.

Danisch, Simon and Julius Krumbiegel (2021). "Makie.jl: Flexible high-performance data visualization for Julia". In: *Journal of Open Source Software* 6.65, p. 3349. DOI: 10.21105/joss.03349. URL: https://doi.org/10.21105/joss.03349.

de Montserrat, Albert, Pascal Aellig, Ludovic Räss, Thibault Duretz, Ivan Utkin, Boris Kaus, and Hendrik Ranocha (2025). *JuliaGeodynamics/JustPIC.jl: v0.5.10 (v0.5.10). Zenodo.* https://doi.org/10.5281/zenodo.15704602.

Dewey, JF, ML Helman, SD Knott, E Turco, and DHW Hutton (1989). "Kinematics of the western Mediterranean". In: *Geological Society, London, Special Publications* 45.1, pp. 265–283.

Di Leo, JF, AM Walker, Z-H Li, J Wookey, Neil M Ribe, J-M Kendall, and Andrea Tommasi (2014). "Development of texture and seismic anisotropy during the onset of subduction". In: *Geochemistry, Geophysics, Geosystems* 15.1, pp. 192–212.

Duarte, João C, Nicolas Riel, Filipe M Rosas, Anton Popov, Christian Schuler, and Boris JP Kaus (2024). "Gibraltar subduction zone is invading the Atlantic". In: *Geology* 52.5, pp. 331–335.

Duretz, Thibault, Taras V Gerya, and Dave A May (2011). "Numerical modelling of spontaneous slab breakoff and subsequent topographic response". In: *Tectonophysics* 502.1-2, pp. 244–256.

Duretz, Thibault and Stefan M Schmalholz (2015). "From symmetric necking to localized asymmetric shearing: The role of mechanical layering". In: *Geology* 43.8, pp. 711–714.

El-Sharkawy, Amr, Thomas Meier, Sergei Lebedev, Jan H Behrmann, Mona Hamada, Luigia Cristiano, Christian Weidle, and Daniel Köhn (2020). "The slab puzzle of the Alpine-Mediterranean region: Insights from a new, high-resolution, shear wave velocity model of the upper mantle". In: *Geochemistry, Geophysics, Geosystems* 21.8, e2020GC008993.

Elliott, Conal (2018). "The simple essence of automatic differentiation". In: *Proceedings of the ACM on Programming Languages* 2.ICFP, pp. 1–29.

Erman, Ceyhun, Seda Yolsal-Çevikbilen, Tuna Eken, Frederik Tilmann, Derya Keleş, and Tuncay Taymaz (2022). "Constraints on the lithospheric kinematics in the Aegean and western Anatolia unveiled by SKS splitting observations". In: *Journal of Geophysical Research: Solid Earth* 127.12, e2022JB025265.

Eskens, LHJ, A Piccolo, M Thielmann, B Claussmann, M Lejri, TA Ehlers, and N Andrić-Tomašević (2025). "The tectonostratigraphic expression of slab breakoff in foreland basins: Insights from 2D forward stratigraphic modeling". In: *Tectonics* 44.7, e2024TC008664.

Evangelidis, CP (2017). "Seismic anisotropy in the Hellenic subduction zone: Effects of slab segmentation and subslab mantle flow". In: *Earth and Planetary Science Letters* 480, pp. 97–106.

Evangelidis, CP, W-T Liang, NS Melis, and KI Konstantinou (2011). "Shear wave anisotropy beneath the Aegean inferred from SKS splitting observations". In: *Journal of Geophysical Research: Solid Earth* 116.B4.

Faccenda, Manuele and Fabio Antonio Capitanio (2012). "Development of mantle seismic anisotropy during subduction-induced 3-D flow". In: *Geophysical Research Letters* 39.11.

— (2013). "Seismic anisotropy around subduction zones: Insights from three-dimensional modeling of upper mantle deformation and SKS splitting calculations". In: *Geochemistry, Geophysics, Geosystems* 14.1, pp. 243–262.

Faccenna, Claudio and Thorsten W Becker (2010). "Shaping mobile belts by small-scale convection". In: *Nature* 465.7298, pp. 602–605.

Faccenna, Claudio, Thorsten W Becker, Ludwig Auer, Andrea Billi, Lapo Boschi, Jean Pierre Brun, Fabio A Capitanio, Francesca Funiciello, Ferenc Horvàth, Laurent Jolivet, et al. (2014). "Mantle dynamics in the Mediterranean". In: *Reviews of Geophysics* 52.3, pp. 283–332.

Faccenna, Claudio, Thorsten W Becker, Francesco Pio Lucente, Laurent Jolivet, and Federico Rossetti (2001). "History of subduction and back arc extension in the Central Mediterranean". In: *Geophysical Journal International* 145.3, pp. 809–820.

Faccenna, Claudio, Claudia Piromallo, Ana Crespo-Blanc, Laurent Jolivet, and Federico Rossetti (2004). "Lateral slab deformation and the origin of the western Mediterranean arcs". In: *Tectonics* 23.1.

Fellin, Maria Giuditta, Malwina San Jose, Claudio Faccenna, Sean D Willett, Domenico Cosentino, Riccardo Lanari, Loraine Gourbet, and Colin Maden (2022). "Transition from slab roll-back to slab break-off in the central Apennines, Italy: Constraints from the stratigraphic and thermochronologic record". In: *Bulletin* 134.7-8, pp. 1916–1930.

Gerya, Taras (2019). *Introduction to numerical geodynamic modelling*. Cambridge University Press.

Ghelichkhan, Sia, Angus Gibson, D Rhodri Davies, Stephan C Kramer, and David A Ham (2024). "Automatic adjoint-based inversion schemes for geodynamics: reconstructing the evolution of Earth's mantle in space and time". In: *Geoscientific Model Development* 17.13, pp. 5057–5086.

Ghelichkhan, Siavash and Hans-Peter Bunge (2016). "The compressible adjoint equations in geodynamics: derivation and numerical assessment". In: *GEM-International Journal on Geomathematics* 7.1, pp. 1–30.

Ghelichkhan, Siavash, Hans-Peter Bunge, and J Oeser (2021). "Global mantle flow retrodictions for the early Cenozoic using an adjoint method: evolving dynamic topographies, deep mantle structures, flow trajectories and sublithospheric stresses". In: *Geophysical Journal International* 226.2, pp. 1432–1460.

Giles, Michael B and Niles A Pierce (2000). "An introduction to the adjoint approach to design". In: *Flow, turbulence and combustion* 65.3, pp. 393–415.

Givoli, Dan (2021). "A tutorial on the adjoint method for inverse problems". In: *Computer Methods in Applied Mechanics and Engineering* 380, p. 113810.

Glerum, Anne C, Wim Spakman, Douwe JJ van Hinsbergen, Cedric Thieulot, and Casper Pranger (2021). "Sensitivity of horizontal surface deformation to mantle dynamics from 3D instantaneous dynamics modeling of the eastern Mediterranean region". In: *EarthArXiv eprints*, X5FW59.

Griewank, Andreas and Andrea Walther (2008). *Evaluating derivatives: principles and techniques of algorithmic differentiation*. SIAM.

Gueguen, Erwan, Carlo Doglioni, and Manuel Fernandez (1998). "On the post-25 Ma geodynamic evolution of the western Mediterranean". In: *Tectonophysics* 298.1-3, pp. 259–269.

Gunzburger, Max (2000). "Adjoint equation-based methods for control problems in incompressible, viscous flows". In: *Flow, Turbulence and Combustion* 65.3, pp. 249–272.

Gutscher, M-A, J Malod, J-P Rehault, I Contrucci, F Klingelhoefer, L Mendes-Victor, and W Spakman (2002). "Evidence for active subduction beneath Gibraltar". In: *Geology* 30.12, pp. 1071–1074.

Handy, Mark R, Joerg Giese, Stefan M Schmid, Jan Pleuger, Wim Spakman, Kujtim Onuzi, and Kamil Ustaszewski (2019). "Coupled crust-mantle response to slab tearing, bending, and rollback along the Dinaride-Hellenide orogen". In: *Tectonics* 38.8, pp. 2803–2828.

Handy, Mark R, Stefan M Schmid, Romain Bousquet, Eduard Kissling, and Daniel Bernoulli (2010). "Reconciling plate-tectonic reconstructions of Alpine Tethys with the geological–geophysical record of spreading and subduction in the Alps". In: *Earth-Science Reviews* 102.3-4, pp. 121–158.

Handy, Mark R, Stefan M Schmid, Marcel Paffrath, Wolfgang Friederich, et al. (2021). "Orogenic lithosphere and slabs in the greater Alpine area-interpretations based on teleseismic P-wave tomography". In: *Solid Earth* 12.11, pp. 2633–2669.

Handy, Mark R, Kamil Ustaszewski, and Eduard Kissling (2015). "Reconstructing the Alps–Carpathians–Dinarides as a key to understanding switches in subduction polarity, slab gaps and surface motion". In: *International Journal of Earth Sciences* 104, pp. 1–26.

Harlow, Francis H and J Eddie Welch (1965). "Numerical calculation of time-dependent viscous incompressible flow of fluid with free surface". In: *The physics of fluids* 8.12, pp. 2182–2189.

Hasterok, Derrick, Jacqueline A Halpin, Alan S Collins, Martin Hand, Corné Kreemer, Matthew G Gard, and Stijn Glorie (2022). "New maps of global geological provinces and tectonic plates". In: *Earth-Science Reviews* 231, p. 104069.

Hein, Gerrit, Petr Kolínskỳ, Irene Bianchi, and Götz Bokelmann (2021). "Shear wave splitting in the Alpine region". In: *Geophysical Journal International* 227.3, pp. 1996–2015.

Hill, Adrian and Guillaume Dalle (2025). "Sparser, Better, Faster, Stronger: Sparsity Detection for Efficient Automatic Differentiation". In: *Transactions on Machine Learning Research Journal*.

Hill, Adrian, Guillaume Dalle, and Alexis Montoison (2025). "An Illustrated Guide to Automatic Sparse Differentiation". In: *ICLR Blogposts 2025*. https://iclr-blogposts.github.io/2025/blog/sparse-autodiff/.

Hinsbergen, D. J. J. van, M Mensink, CG Langereis, M Maffione, L Spalluto, MARCELLO Tropeano, and Luisa Sabato (2014). "Did Adria rotate relative to Africa?" In: *Solid Earth* 5.2, pp. 611–629.

Hinsbergen, D. J. J. van, Trond H Torsvik, Stefan M Schmid, Liviu C Maţenco, Marco Maffione, Reinoud LM Vissers, Derya Gürer, and Wim Spakman (2020). "Orogenic architecture of the Mediterranean region and kinematic reconstruction of its tectonic evolution since the Triassic". In: *Gondwana Research* 81, pp. 79–229.

Hirth, Greg and David Kohlstedt (2003). "Rheology of the upper mantle and the mantle wedge: A view from the experimentalists". In: *Geophysical monograph series* 138, pp. 83–105.

Holt, AF, LH Royden, and TW Becker (2017). "The dynamics of double slab subduction". In: *Geophysical Journal International* 209.1, pp. 250–265.

Honnorat, Marc, Joel Marin, Jerome Monnier, and Xijun Lai (2007). "Dassflow v1. 0: a variational data assimilation software for 2D river flows". PhD thesis. INRIA.

Horbach, André (2020). "Theory and application of the adjoint method in geodynamics and an extended review of analytical solution methods to the Stokes equation". In.

Horbach, André, Hans-Peter Bunge, and Jens Oeser (2014). "The adjoint method in geodynamics: derivation from a general operator formulation and application to the initial condition problem in a high resolution mantle circulation model". In: *GEM-International Journal on Geomathematics* 5.2, pp. 163–194.

Hua, Yuanyuan, Dapeng Zhao, and Yixian Xu (2017). "P wave anisotropic tomography of the Alps". In: *Journal of Geophysical Research: Solid Earth* 122.6, pp. 4509–4528.

Hunen, Jeroen van and Mark B Allen (2011). "Continental collision and slab break-off: A comparison of 3-D numerical models with observations". In: *Earth and Planetary Science Letters* 302.1-2, pp. 27–37.

Jolivet, Laurent (2023). "Tethys and Apulia (Adria), 100 years of reconstructions". In: *Comptes Rendus. Géoscience* 355.S2, pp. 9–28.

Jolivet, Laurent and Claudio Faccenna (2000). "Mediterranean extension and the Africa-Eurasia collision". In: *Tectonics* 19.6, pp. 1095–1106.

Jolivet, Laurent, Claudio Faccenna, and Claudia Piromallo (2009). "From mantle to crust: Stretching the Mediterranean". In: *Earth and Planetary Science Letters* 285.1-2, pp. 198–209.

Jung, Haemyeong, I Katayama, Z Jiang, T Hiraga, and S-I Karato (2006). "Effect of water and stress on the lattice-preferred orientation of olivine". In: *Tectonophysics* 421.1-2, pp. 1–22.

Kaminski, Edouard, Neil M Ribe, and Jules T Browaeys (2004). "D-Rex, a program for calculation of seismic anisotropy due to crystal lattice preferred orientation in the convective upper mantle". In: *Geophysical Journal International* 158.2, pp. 744–752.

Karato, Shun-ichiro, Haemyeong Jung, Ikuo Katayama, and Philip Skemer (2008). "Geodynamic significance of seismic anisotropy of the upper mantle: New insights from laboratory studies". In: *Annu. Rev. Earth Planet. Sci.* 36.1, pp. 59–95.

Kästle, Emanuel D, Claudio Rosenberg, Lapo Boschi, Nicolas Bellahsen, Thomas Meier, and Amr El-Sharkawy (2020). "Slab break-offs in the Alpine subduction zone". In: *International Journal of Earth Sciences* 109, pp. 587–603.

Kaus, Boris JP (2010). "Factors that control the angle of shear bands in geodynamic numerical models of brittle deformation". In: *Tectonophysics* 484, pp. 36–47.

Kaus, Boris JP, Anton A Popov, T Baumann, A Pusok, Arthur Bauville, Naiara Fernandez, and Marine Collignon (2016). "Forward and inverse modelling of lithospheric deformation on geological timescales". In: *Proceedings of nic symposium.* Vol. 48. John von Neumann Institute for Computing (NIC), NIC Series, pp. 978–983.

Kaus, Boris JP, Marcel Thielmann, Pascal Aellig, Albert de Montserrat, Luca de Siena, Jacob Frasukiewicz, Lukas Fuchs, Andrea Piccolo, Hendrik Ranocha, Nicolas Riel, et al. (2024). "GeophysicalModelGenerator. jl: A Julia package to visualise geoscientific data and create numerical model setups". In: *Journal of Open Source Software* 9.103, p. 6763.

Kaviris, George, Ioannis Fountoulakis, Ioannis Spingos, Christos Millas, Panayotis Papadimitriou, and George Drakatos (2018). "Mantle dynamics beneath Greece from SKS and PKS seismic anisotropy study". In: *Acta Geophysica* 66.6, pp. 1341–1357.

Kincaid, C and RW Griffiths (2003). "Laboratory models of the thermal evolution of the mantle during rollback subduction". In: *Nature* 425.6953, pp. 58–62.

Király, Ágnes, Claudio Faccenna, and Francesca Funiciello (2018a). "Subduction zones interaction around the Adria microplate and the origin of the Apenninic arc". In: *Tectonics* 37.10, pp. 3941–3953.

Király, Ágnes, Francesca Funiciello, Fabio A Capitanio, and Claudio Faccenna (2021). "Dynamic interactions between subduction zones". In: *Global and Planetary Change* 202, p. 103501.

Király, Ágnes, Adam F Holt, Francesca Funiciello, Claudio Faccenna, and Fabio A Capitanio (2018b). "Modeling slab-slab interactions: Dynamics of outward dipping double-sided subduction systems". In: *Geochemistry, Geophysics, Geosystems* 19.3, pp. 693–714.

Király, Ágnes, Daniel E Portner, Kirstie L Haynie, Benjamin H Chilson-Parks, Tithi Ghosh, Margarete Jadamec, Anna Makushkina, Michael Manga, Louis Moresi, and Keely A O'Farrell (2020). "The effect of slab gaps on subduction dynamics and mantle upwelling". In: *Tectonophysics* 785, p. 228458.

Kiss, Daniel, Evangelos Moulas, Boris JP Kaus, and Arne Spang (2023). "Decompression and fracturing caused by magmatically induced thermal stresses". In: *Journal of Geophysical Research: Solid Earth* 128.3, e2022JB025341.

Kissling, Eduard (2024). "Adria microplate: A puzzling key stone in west-central Mediterranean geodynamics". In: *Annals of geophysics* 67.4, S431.

Kneller, Erik A, Peter E Van Keken, Shun-ichiro Karato, and Jeffrey Park (2005). "B-type olivine fabric in the mantle wedge: Insights from high-resolution non-Newtonian subduction zone models". In: *Earth and Planetary Science Letters* 237.3-4, pp. 781–797.

Koulakov, I, A Jakovlev, I Zabelina, F Roure, S Cloetingh, S El Khrepy, and N Al-Arifi (2015). "Subduction or delamination beneath the Apennines? Evidence from regional tomography". In: *Solid Earth* 6.2, pp. 669–679.

Koulakov, Ivan, Bogdan Zaharia, Bogdan Enescu, M Radulian, M Popa, Stefano Parolai, and Jochen Zschau (2010). "Delamination or slab detachment beneath Vrancea? New arguments from local earthquake tomography". In: *Geochemistry, Geophysics, Geosystems* 11.3.

Kovács, I, Gy Falus, G Stuart, K Hidas, Cs Szabó, MFJ Flower, E Hegedűs, K Posgay, and L Zilahi-Sebess (2012). "Seismic anisotropy and deformation patterns in upper mantle xenoliths from the central Carpathian–Pannonian region: Asthenospheric flow as a driving force for Cenozoic extension and extrusion?" In: *Tectonophysics* 514, pp. 168–179.

Kruse, Jan Philipp, Georg Rümpker, Frederik Link, Thibault Duretz, and Harro Schmeling (2024). "Anisotropy and XKS splitting from geodynamic models of double subduction: testing the limits of interpretation". In: *Geophysical Journal International* 239.3, pp. 1400–1424.

Kumar, Ajay, Mauro Cacace, Magdalena Scheck-Wenderoth, Hans-Jürgen Götze, and Boris JP Kaus (2022). "Present-Day Upper-Mantle Architecture of the Alps: Insights From Data-Driven Dynamic Modeling". In: *Geophysical Research Letters* 49.18, e2022GL099476.

Kästle, Emanuel, Grace Shephard, and Anne Paul (2022). *Votemaps of the Alpine upper mantle*.

Le Breton, Eline, Sascha Brune, Kamil Ustaszewski, Sabin Zahirovic, Maria Seton, and R Dietmar Müller (2021). "Kinematics and extent of the Piemont–Liguria Basin–implications for subduction processes in the Alps". In: *Solid Earth* 12.4, pp. 885–913.

Le Breton, Eline, Mark R Handy, Giancarlo Molli, and Kamil Ustaszewski (2017). "Post-20 Ma motion of the Adriatic Plate: New constraints from surrounding orogens and implications for crust-mantle decoupling". In: *Tectonics* 36.12, pp. 3135–3154.

Li, Dunzhu, Michael Gurnis, and Georg Stadler (2017). "Towards adjoint-based inversion of time-dependent mantle convection with nonlinear viscosity". In: *Geophysical Journal International* 209.1, pp. 86–105.

Li, Xiaoye S and James W Demmel (2003). "SuperLU_DIST: A scalable distributed-memory sparse direct solver for unsymmetric linear systems". In: *ACM Transactions on Mathematical Software (TOMS)* 29.2, pp. 110–140.

Li, Zhong-Hai and Neil M Ribe (2012). "Dynamics of free subduction from 3-D boundary element modeling". In: *Journal of Geophysical Research: Solid Earth* 117.B6.

Link, F and G Rümpker (2023). "Shear-Wave Splitting Reveals Layered-Anisotropy Beneath the European Alps in Response to Mediterranean Subduction". In: *Journal of Geophysical Research: Solid Earth* 128.9, e2023JB027192.

Link, Frederik and Georg Rümpker (2021). "Resolving seismic anisotropy of the lithosphere - asthenosphere in the Central/Eastern Alps beneath the SWATH-D network". In: *Frontiers in Earth Science* 9, p. 679887.

Lippitsch, Regina, Edi Kissling, and Jörg Ansorge (2003). "Upper mantle structure beneath the Alpine orogen from high-resolution teleseismic tomography". In: *Journal of Geophysical Research: Solid Earth* 108.B8.

Lis Mancilla, Flor de, Guillermo Booth-Rea, Daniel Stich, José Vicente Pérez-Peña, José Morales, José Miguel Azañón, Rosa Martin, and Flavio Giaconia (2015). "Slab rupture and delamination under the Betics and Rif constrained from receiver functions". In: *Tectonophysics* 663, pp. 225–237.

Liu, Lijun and Michael Gurnis (2008). "Simultaneous inversion of mantle properties and initial conditions using an adjoint of mantle convection". In: *Journal of Geophysical Research: Solid Earth* 113.B8.

Lo Bue, Rosalia, Manuele Faccenda, and Jianfeng Yang (2021). "The role of adria plate lithospheric structures on the recent dynamics of the central mediterranean region". In: *Journal of Geophysical Research: Solid Earth* 126.10, e2021JB022377.

Lo Bue, Rosalia, Francesco Rappisi, Brandon Paul Vanderbeek, and Manuele Faccenda (2022). "Tomographic image interpretation and Central-Western Mediterranean-like upper mantle dynamics from coupled seismological and geodynamic modeling approach". In: *Frontiers in Earth Science* 10, p. 884100.

Löberich, Eric and Götz Bokelmann (2020). "Mantle flow under the Central Alps: Constraints from non-vertical SKS shear-wave splitting". In: *Solid Earth Discussions* 2020, pp. 1–41.

Long, Maureen D and Thorsten W Becker (2010). "Mantle dynamics and seismic anisotropy". In: *Earth and planetary science letters* 297.3-4, pp. 341–354.

Long, Maureen D and Rob D van der Hilst (2005). "Upper mantle anisotropy beneath Japan from shear wave splitting". In: *Physics of the Earth and Planetary Interiors* 151.3-4, pp. 206–222.

Long, Maureen D and Paul G Silver (2008). "The subduction zone flow field from seismic anisotropy: A global view". In: *science* 319.5861, pp. 315–318.

Lourenço, Diogo L, Antoine B Rozel, Maxim D Ballmer, and Paul J Tackley (2020). "Plutonic-squishy lid: A new global tectonic regime generated by intrusive magmatism on Earth-like planets". In: *Geochemistry, Geophysics, Geosystems* 21.4, e2019GC008756.

Macherel, Emilie, Ludovic Räss, and Stefan M Schmalholz (2024). "3D stresses and velocities caused by continental plateaus: Scaling analysis and numerical calculations with application to the Tibetan plateau". In: *Geochemistry, Geophysics, Geosystems* 25.3, e2023GC011356.

Maesano, Francesco E, Mara M Tiberti, and Roberto Basili (2017). "The Calabrian Arc: three-dimensional modelling of the subduction interface". In: *Scientific reports* 7.1, p. 8887.

Mainprice, David and Paul G Silver (1993). "Interpretation of SKS-waves using samples from the subcontinental lithosphere". In: *Physics of the Earth and Planetary Interiors* 78.3-4, pp. 257–280.

Margossian, Charles C (2019). "A review of automatic differentiation and its efficient implementation". In: *Wiley interdisciplinary reviews: data mining and knowledge discovery* 9.4, e1305.

Marta, Andre C, CA Mader, JRRA Martins, E Van der Weide, and JJ Alonso (2007). "A methodology for the development of discrete adjoint solvers using automatic differentiation tools". In: *International Journal of Computational Fluid Dynamics* 21.9-10, pp. 307–327.

Martin, Nathan and Jérôme Monnier (2014). "Adjoint accuracy for the full Stokes ice flow model: limits to the transmission of basal friction variability to the surface". In: *The Cryosphere* 8.2, pp. 721–741.

Martinod, Joseph, Ayend-Christ Daou, Laurent Métral, and Christian Sue (2024). "Did subduction in the western Mediterranean drive Neogene alpine dynamics? Insights from analogue modeling". In: *BSGF-Earth Sciences Bulletin* 195.1, p. 5.

Maupin, V, J Park, B Romanowicz, and A Dziewonski (2007). "Theory and observations—wave propagation in anisotropic media". In: *Seismology and the Structure of the Earth. Treatise on Geophysics* 1, pp. 289–321.

McKenzie, Dan (1972). "Active tectonics of the Mediterranean region". In: *Geophysical Journal International* 30.2, pp. 109–185.

Menant, Armel, Laurent Jolivet, and Bruno Vrielynck (2016). "Kinematic reconstructions and magmatic evolution illuminating crustal and mantle dynamics of the eastern Mediterranean region since the late Cretaceous". In: *Tectonophysics* 675, pp. 103–140.

Mitterbauer, Ulrike, Michael Behm, Ewald Brückl, Regina Lippitsch, Alexander Guterch, G Randy Keller, Elena Koslovskaya, Eva-Maria Rumpfhuber, and Franjo Šumanovac (2011). "Shape and origin of the East-Alpine slab constrained by the ALPASS teleseismic model". In: *Tectonophysics* 510.1-2, pp. 195–206.

Monna, S, C Montuori, C Piromallo, and L Vinnik (2019). "Mantle structure in the Central Mediterranean Region from P and S receiver functions". In: *Geochemistry, Geophysics, Geosystems* 20.10, pp. 4545–4566.

Monteiller, Vadim and Sébastien Chevrot (2010). "How to make robust splitting measurements for single-station analysis and three-dimensional imaging of seismic anisotropy". In: *Geophysical Journal International* 182.1, pp. 311–328.

Moses, William and Valentin Churavy (2020). "Instead of Rewriting Foreign Code for Machine Learning, Automatically Synthesize Fast Gradients". In: *Advances in Neural Information Processing Systems*. Ed. by H. Larochelle, M. Ranzato, R. Hadsell, M. F. Balcan, and H. Lin. Vol. 33. Curran Associates, Inc., pp. 12472–12485. URL: https://proceedings.neurips.cc/paper/2020/file/9332c513ef44b682e9347822c2e457ac-Paper.pdf.

Moses, William S., Valentin Churavy, Ludger Paehler, Jan Hückelheim, Sri Hari Krishna Narayanan, Michel Schanen, and Johannes Doerfert (2021). "Reverse-Mode Automatic Differentiation and Optimization of GPU Kernels via Enzyme". In:

Proceedings of the International Conference for High Performance Computing, Networking, Storage and Analysis. SC '21. St. Louis, Missouri: Association for Computing Machinery. ISBN: 9781450384421. DOI: 10.1145/3458817.3476165. URL: https://doi.org/10.1145/3458817.3476165.

Müller, J-D and P Cusdin (2005). "On the performance of discrete adjoint CFD codes using automatic differentiation". In: *International journal for numerical methods in fluids* 47.8-9, pp. 939–945.

Muttoni, Giovanni, Eduardo Garzanti, Laura Alfonsi, Simonetta Cirilli, Daniela Germani, and William Lowrie (2001). "Motion of Africa and Adria since the Permian: paleomagnetic and paleoclimatic constraints from northern Libya". In: *Earth and Planetary Science Letters* 192.2, pp. 159–174.

Navon, I Michael, Xiaolei Zou, J Derber, and J Sela (1992). "Variational data assimilation with an adiabatic version of the NMC spectral model". In: *Monthly weather review* 120.7, pp. 1433–1446.

Omlin, Samuel, Ludovic Räss, and Ivan Utkin (2022). "Distributed Parallelization of xPU Stencil Computations in Julia". In: *arXiv preprint arXiv:2211.15716*.

Omlin, Samuel and Ludovic Räss (2024). "High-performance xPU Stencil Computations in Julia". In: *Proceedings of the JuliaCon Conferences* 6.64, p. 138. DOI: 10.21105/jcon.00138. URL: https://doi.org/10.21105/jcon.00138.

Paffrath, Marcel, Wolfgang Friederich, Stefan M Schmid, Mark R Handy, AlpArray, AlpArray-Swath D Working Group, et al. (2021). "Imaging structure and geometry of slabs in the greater Alpine area–A P-wave travel-time tomography using AlpArray Seismic Network data". In: *Solid Earth* 12.11, pp. 2671–2702.

Pearce, Frederick Douglas, S Rondenay, M Sachpazi, M Charalampakis, and Leigh H Royden (2012). "Seismic investigation of the transition from continental to oceanic subduction along the western Hellenic Subduction Zone". In: *Journal of Geophysical Research: Solid Earth* 117.B7.

Peral, Mireia, Manel Fernandez, Jaume Vergés, Sergio Zlotnik, and Ivone Jiménez-Munt (2022). "Numerical modelling of opposing subduction in the Western Mediterranean". In: *Tectonophysics* 830, p. 229309.

Petit, Carole, Anthony Jourdon, and Nicolas Coltice (2025). "Reconstructing landscapes: an adjoint model of the Stream Power and diffusion erosion equation". In: *EGUsphere* 2025, pp. 1–23.

Petrescu, Laura, Silvia Pondrelli, Simone Salimbeni, and Manuele Faccenda (2020a). "Mantle flow below the central and greater Alpine region: Insights from SKS anisotropy analysis at AlpArray and permanent stations". In: *Solid Earth Discussions* 2020, pp. 1–26.

Petrescu, Laura, Graham Stuart, Gregory Houseman, and Ian Bastow (2020b). "Upper mantle deformation signatures of craton–orogen interaction in the Carpathian–Pannonian region from SKS anisotropy analysis". In: *Geophysical Journal International* 220.3, pp. 2105–2118.

Piccardi, L, Federico Sani, G Moratti, D Cunningham, and E Vittori (2011). "Present-day geodynamics of the circum-Adriatic region: An overview". In: *Journal of geodynamics* 51.2-3, pp. 81–89.

Piromallo, Claudia and Andrea Morelli (2003). "P wave tomography of the mantle under the Alpine-Mediterranean area". In: *Journal of Geophysical Research: Solid Earth* 108.B2.

Plomerová, Jaroslava and Vladislav Babuška (2010). "Long memory of mantle lithosphere fabric—European LAB constrained from seismic anisotropy". In: *Lithos* 120.1-2, pp. 131–143.

Pons, Michaël, Constanza Rodriguez Piceda, Stephan V Sobolev, Magdalena Scheck-Wenderoth, and Manfred R Strecker (2023). "Localization of deformation in a non-collisional subduction orogen: The roles of dip geometry and plate strength on the evolution of the broken Andean foreland, Sierras Pampeanas, Argentina". In: *Tectonics* 42.8, e2023TC007765.

Popov, AA and Stephan V Sobolev (2008). "SLIM3D: A tool for three-dimensional thermomechanical modeling of lithospheric deformation with elasto-visco-plastic rheology". In: *Physics of the earth and planetary interiors* 171.1-4, pp. 55–75.

Pusok, Adina E and Dave R Stegman (2019). "Formation and stability of same-dip double subduction systems". In: *Journal of Geophysical Research: Solid Earth* 124.7, pp. 7387–7412.

Qorbani, Ehsan, Götz Bokelmann, István Kovács, Frank Horváth, and György Falus (2016). "Deformation in the asthenospheric mantle beneath the Carpathian- Pannonian Region". In: *Journal of Geophysical Research: Solid Earth* 121.9, pp. 6644–6657.

Ranalli, Giorgio (1995). *Rheology of the Earth*. Springer Science & Business Media.

Rappisi, F, R Lo Bue, BP Vanderbeek, JM Confal, C Erman, P Baccheschi, S Pondrelli, T Eken, S Yolsal-Çevikbilen, and M Faccenda (2025). "3-D mantle flow and structure of the Mediterranean from combined P-wave and splitting intensity anisotropic tomography". In: *Journal of Geophysical Research: Solid Earth* 130.6, e2024JB030883.

Rappisi, Francesco, BP VanderBeek, Manuele Faccenda, Andrea Morelli, and Irene Molinari (2022). "Slab Geometry and Upper Mantle Flow Patterns in the Central Mediterranean From 3D Anisotropic P-Wave Tomography". In: *Journal of Geophysical Research: Solid Earth* 127.5, e2021JB023488.

Räss, Ludovic, Ivan Utkin, Thibault Duretz, Samuel Omlin, and Yuri Y Podladchikov (2022). "Assessing the robustness and scalability of the accelerated pseudo-transient method". In: *Geoscientific Model Development* 15.14, pp. 5757–5786.

Ratnaswamy, Vishagan, Georg Stadler, and Michael Gurnis (2015). "Adjoint-based estimation of plate coupling in a non-linear mantle flow model: theory and examples". In: *Geophysical Journal International* 202.2, pp. 768–786.

Reilinger, Robert and Simon McClusky (2011). "Nubia–Arabia–Eurasia plate motions and the dynamics of Mediterranean and Middle East tectonics". In: *Geophysical Journal International* 186.3, pp. 971–979.

Reiss, MC, MD Long, and N Creasy (2019). "Lowermost mantle anisotropy beneath Africa from differential SKS-SKKS shear-wave splitting". In: *Journal of Geophysical Research: Solid Earth* 124.8, pp. 8540–8564.

Reuber, Georg S (2021). "Statistical and deterministic inverse methods in the geosciences: introduction, review, and application to the nonlinear diffusion equation". In: *GEM-International Journal on Geomathematics* 12.1, p. 19.

Reuber, Georg S, Lukas Holbach, Anton A Popov, Martin Hanke, and Boris JP Kaus (2020a). "Inferring rheology and geometry of subsurface structures by adjoint-based inversion of principal stress directions". In: *Geophysical Journal International* 223.2, pp. 851–861.

Reuber, Georg S, Lukas Holbach, and Ludovic Räss (2020b). "Adjoint-based inversion for porosity in shallow reservoirs using pseudo-transient solvers for non-linear hydro-mechanical processes". In: *Journal of Computational Physics* 423, p. 109797.

Reuber, Georg S, Anton A Popov, and Boris JP Kaus (2018). "Deriving scaling laws in geodynamics using adjoint gradients". In: *Tectonophysics* 746, pp. 352–363.

Ribe, Neil M (1989). "Seismic anisotropy and mantle flow". In: *Journal of Geophysical Research: Solid Earth* 94.B4, pp. 4213–4223.

Ribe, Neil M (1992). "On the relation between seismic anisotropy and finite strain". In: *Journal of Geophysical Research: Solid Earth* 97.B6, pp. 8737–8747.

Ring, Uwe, Johannes Glodny, Thomas Will, and Stuart Thomson (2010). "The Hellenic subduction system: high-pressure metamorphism, exhumation, normal faulting, and large-scale extension". In: *Annual Review of Earth and Planetary Sciences* 38, pp. 45–76.

Romagny, Adrien, Laurent Jolivet, Armel Menant, Eloïse Bessière, Agnès Maillard, Albane Canva, Christian Gorini, and Romain Augier (2020). "Detailed tectonic reconstructions of the Western Mediterranean region for the last 35 Ma, insights on driving mechanisms". In: *Bulletin de la Société géologique de France* 191.1.

Rosenbaum, Gideon, Gordon S Lister, and Cecile Duboz (2002a). "Reconstruction of the tectonic evolution of the western Mediterranean since the Oligocene". In: *Journal of the Virtual Explorer* 8.January, pp. 107–130.

Rosenbaum, Gideon, Gordon S Lister, and Cécile Duboz (2002b). "Relative motions of Africa, Iberia and Europe during Alpine orogeny". In: *Tectonophysics* 359.1-2, pp. 117–129.

Rosenbaum, Gideon, Gordon S Lister, and Cecile Duboz (2004). "The Mesozoic and Cenozoic motion of Adria (central Mediterranean): a review of constraints and limitations". In: *Geodinamica Acta* 17.2, pp. 125–139.

Rosenberg, Claudio L, Nicolas Bellahsen, Alain Rabaute, and J-B Girault (2021). "Distribution, style, amount of collisional shortening, and their link to Barrovian metamorphism in the European Alps". In: *Earth-Science Reviews* 222, p. 103774.

Roth, Rolf and Stefan Ulbrich (2013). "A discrete adjoint approach for the optimization of unsteady turbulent flows". In: *Flow, turbulence and combustion* 90.4, pp. 763–783.

Royden, Leigh and Claudio Faccenna (2018). "Subduction orogeny and the Late Cenozoic evolution of the Mediterranean Arcs". In: *Annual Review of Earth and Planetary Sciences* 46, pp. 261–289.

Rubinstein, R and SN Atluri (1983). "Objectivity of incremental constitutive relations over finite time steps in computational finite deformation analyses". In: *Computer Methods in Applied Mechanics and Engineering* 36.3, pp. 277–290.

Salimbeni, Simone, Silvia Pondrelli, Irene Molinari, Josip Stipčević, Snježan Prevolnik, Iva Dasović, and AlpArray-CASE working group (2022). "Seismic anisotropy across Adria plate, from the Apennines to the Dinarides". In: *Frontiers in Earth Science* 10, p. 881138.

Saltelli, Andrea, Stefano Tarantola, and Francesca Campolongo (2000). "Sensitivity analysis as an ingredient of modeling". In: *Statistical science*, pp. 377–395.

Scarfì, Luciano, Marco Firetto Carlino, and Carla Musumeci (2023). "Seismic anisotropy to investigate lithospheric-scale tectonic structures and mantle dynamics in southern Italy". In: *Scientific Reports* 13.1, p. 20932.

Schefer, Senecio, Vladica Cvetković, Bernhard Fügenschuh, Alexandre Kounov, Maria Ovtcharova, Urs Schaltegger, and Stefan M Schmid (2011). "Cenozoic granitoids in the Dinarides of southern Serbia: age of intrusion, isotope geochemistry, exhumation history and significance for the geodynamic evolution of the Balkan Peninsula". In: *International Journal of Earth Sciences* 100, pp. 1181–1206.

Schellart, Wouter P (2024). "Subduction dynamics and overriding plate deformation". In: *Earth-Science Reviews*, p. 104755.

Schettino, Antonio and Eugenio Turco (2011). "Tectonic history of the western Tethys since the Late Triassic". In: *Bulletin* 123.1-2, pp. 89–105.

Schuler, Christian, Boris Kaus, Eline Le Breton, Nicolas Riel, and Anton Popov (Oct. 2024). *Software used in "Mantle Dynamics in the Mediterranean and Plate Motion*

of the Adriatic Microplate: Insights from 3D Thermomechanical Modeling". DOI: 10.5281/zenodo.13987488. URL: https://doi.org/10.5281/zenodo.13987488.

Schuler, Christian, Boris JP Kaus, Eline Le Breton, Nicolas Riel, and Anton A Popov (2025). "Mantle dynamics in the mediterranean and plate motion of the Adriatic microplate: Insights from 3D thermomechanical modeling". In: *Geochemistry, Geophysics, Geosystems* 26.3, e2024GC011996.

Scisciani, Vittorio and Fernando Calamita (2009). "Active intraplate deformation within Adria: Examples from the Adriatic region". In: *Tectonophysics* 476.1-2, pp. 57–72.

Serpelloni, Enrico, Adriano Cavaliere, Leonardo Martelli, Francesco Pintori, Letizia Anderlini, Alessandra Borghi, Daniele Randazzo, Sergio Bruni, Roberto Devoti, Paolo Perfetti, et al. (2022). "Surface velocities and strain-rates in the Euro-Mediterranean region from massive GPS data processing". In: *Frontiers in Earth Science* 10, p. 907897.

Silver, Paul G (1996). "Seismic anisotropy beneath the continents: Probing the depths of geology". In: *Annual review of earth and planetary sciences* 24.1, pp. 385–432.

Silver, Paul G and W Winston Chan (1988). "Implications for continental structure and evolution from seismic anisotropy". In: *Nature* 335.6185, pp. 34–39.

— (1991). "Shear wave splitting and subcontinental mantle deformation". In: *Journal of Geophysical Research: Solid Earth* 96.B10, pp. 16429–16454.

Skemer, Philip and Lars N Hansen (2016). "Inferring upper-mantle flow from seismic anisotropy: an experimental perspective". In: *Tectonophysics* 668, pp. 1–14.

Song, Wenkai, Youqiang Yu, Cong Shen, Fan Lu, and Fansheng Kong (2019). "Asthenospheric flow beneath the Carpathian-Pannonian region: Constraints from shear wave splitting analysis". In: *Earth and Planetary Science Letters* 520, pp. 231–240.

Spakman, Wim and Rinus Wortel (2004). "A tomographic view on western Mediterranean geodynamics". In: *The TRANSMED Atlas. The Mediterranean region from crust to mantle: Geological and geophysical framework of the Mediterranean and the surrounding areas*. Springer, pp. 31–52.

Stampfli, Gérard M and Heinz W Kozur (2006). "Europe from the Variscan to the Alpine cycles". In: *Geological Society, London, Memoirs* 32.1, pp. 57–82.

Stegman, David Robert, Justin Freeman, Wouter Pieter Schellart, L Moresi, and David May (2006). "Influence of trench width on subduction hinge retreat rates in 3-D models of slab rollback". In: *Geochemistry, Geophysics, Geosystems* 7.3.

Stein, Seth and Michael Wysession (2009). *An introduction to seismology, earthquakes, and earth structure*. John Wiley & Sons.

Subašić, Senad, Snježan Prevolnik, Davorka Herak, and Marijan Herak (2017). "Observations of SKS splitting beneath the Central and Southern External Dinarides in the Adria-Eurasia convergence zone". In: *Tectonophysics* 705, pp. 93–100.

Šumanovac, Franjo, Snježana Markušić, Tihomir Engelsfeld, Klaudia Jurković, and Jasna Orešković (2017). "Shallow and deep lithosphere slabs beneath the Dinarides from teleseismic tomography as the result of the Adriatic lithosphere downwelling". In: *Tectonophysics* 712, pp. 523–541.

Thielmann, Marcel, Boris JP Kaus, and Anton A Popov (2015). "Lithospheric stresses in Rayleigh–Bénard convection: effects of a free surface and a viscoelastic Maxwell rheology". In: *Geophysical Supplements to the Monthly Notices of the Royal Astronomical Society* 203.3, pp. 2200–2219.

Tommasi, Andréa, David Mainprice, Gilles Canova, and Yvan Chastel (2000). "Viscoplastic self-consistent and equilibrium-based modeling of olivine lattice preferred

orientations: Implications for the upper mantle seismic anisotropy". In: *Journal of Geophysical Research: Solid Earth* 105.B4, pp. 7893–7908.

Turcotte, Donald L and Gerald Schubert (2002). *Geodynamics*. Cambridge university press.

Ustaszewski, Kamil, Stefan M Schmid, Bernhard Fügenschuh, Matthias Tischler, Eduard Kissling, and Wim Spakman (2008). "A map-view restoration of the Alpine-Carpathian-Dinaridic system for the Early Miocene". In: *Swiss journal of Geosciences* 101, pp. 273–294.

Utkin, Ivan, Yilu Chen, Ludovic Räss, and Mauro A Werder (2025). "Snapshot and time-dependent inversions of basal sliding using automatic generation of adjoint code on graphics processing units". In: *Journal of Glaciology* 71, e72.

Wei, Wei, Dapeng Zhao, Feixiang Wei, Xiang Bai, and Jiandong Xu (2019). "Mantle dynamics of the eastern Mediterranean and Middle East: Constraints from P-wave anisotropic tomography". In: *Geochemistry, Geophysics, Geosystems* 20.10, pp. 4505–4530.

Wessel, Paul, Joaquim Freire Luis, L al Uieda, Remko Scharroo, Florian Wobbe, Walter HF Smith, and Dongdong Tian (2019). "The generic mapping tools version 6". In: *Geochemistry, Geophysics, Geosystems* 20.11, pp. 5556–5564.

Wortel, MJR and W Spakman (1992). "Structure and dynamics of subducted lithosphere in the Mediterranean region". In: *Proceedings of the Koninklijke Nederlandse Akademie van Wetenschappen* 95.3, pp. 325–347.

Wortel, MJR and Wim Spakman (2000). "Subduction and slab detachment in the Mediterranean-Carpathian region". In: *Science* 290.5498, pp. 1910–1917.

Worthen, Jennifer, Georg Stadler, Noemi Petra, Michael Gurnis, and Omar Ghattas (2014). "Towards adjoint-based inversion for rheological parameters in nonlinear viscous mantle flow". In: *Physics of the Earth and Planetary Interiors* 234, pp. 23–34.

Yang, Ting and Michael Gurnis (2016). "Dynamic topography, gravity and the role of lateral viscosity variations from inversion of global mantle flow". In: *Geophysical Supplements to the Monthly Notices of the Royal Astronomical Society* 207.2, pp. 1186–1202.

Yolsal-Çevikbilen, Seda (2014). "Seismic anisotropy along the Cyprean arc and northeast Mediterranean Sea inferred from shear wave splitting analysis". In: *Physics of the Earth and Planetary Interiors* 233, pp. 112–134.

Zhang, Jianshe, Lin Li, Xu Dong, Ziqing Zhang, Yanfeng Zhang, and Xingen Lu (2023). "A discrete adjoint framework coupled with adaptive PCE for robust aerodynamic optimization of turbomachinery under flow uncertainty". In: *Aerospace Science and Technology* 142, p. 108592.

Zhu, Hejun, Ebru Bozdağ, and Jeroen Tromp (2015). "Seismic structure of the European upper mantle based on adjoint tomography". In: *Geophysical Journal International* 201.1, pp. 18–52.